Silicon micro-ring resonator modulator for inter/intra-data centre applications

Silicon micro-ring resonator modulator for inter/intra-data centre applications

By

Zhao Wang

B. Eng. (TJU, Tianjin, China) 2009

M.Sc. (KIT, Karlsruhe, Germany) 2011

A Thesis

Submitted to the School of Graduate Studies in Partial Fulfillment of Requirements for the Degree

Doctor of Philosophy

McMaster University (Engineering Physics)

DOCTOR OF PHILOSOPHY (2017)

Hamilton, Ontario

TITLE: Silicon micro-ring resonator modulator for inter/intra-data centre applications

AUTHOR: Zhao Wang, B.Eng. (Tianjin University, China)

M.Sc. (Karlsruhe Institute of Technology, Germany)

SUPERVISORS: Dr. Andrew P. Knights & Dr. Daniel T. Cassidy

NUMBER OF PAGERS: xiv, 125

Abstract

The recent and rapid growth of silicon photonics is driven by the ever-increasing demand for bandwidth inside and between data centres. Silicon photonics can offer an unparalleled performance in terms of scalability and power consumption with low-cost fabrication through the leveraging of CMOS fabrication techniques. This thesis describes research on the silicon micro-ring resonator modulator, a device which combines energy-efficiency with a compact footprint that is ideal for data centre applications. Both theoretical and experimental work is described in the context of improving the reachability, capacity and stability of the silicon micro-ring resonator modulator for inter/intra-data centre communication. Chapter 2 presents modeling work using MATLAB® that provides predictive results for both device-level and system-level performance. Chapter 3 studies the chirp characteristic of an over-coupled silicon micro-ring resonator modulator and its capability of generating a negative-chirp modulation. The resulting chirp-induced power penalty is measured to be as low as 2.5 dB after 100 km transmission. Chapter 4 focuses on the advanced modulation techniques that can be efficiently exploited for increasing the spectral efficiency in the typically band-limited system. A record single-polarization 104 Gb/s data rate per wavelength (direct-detect) was achieved by using digital signal processing to alleviate the modulation deficiencies that are specific to the silicon micro-ring resonator modulator. In Chapter 5, a generic resonance control method using intrinsic defect-mediated photocurrent is described and experimentally demonstrated to provide stability for the silicon micro-ring resonator modulator during high-speed operation. This control method can also lead to an "all-silicon" system without the need for power detection using germanium.

Acknowledgements

Foremost, I would like to express my deepest gratitude to my two remarkable supervisors, Prof. Andy Knights and Prof. Daniel Cassidy for their continuous support and guidance throughout my entire PhD study. I also want to thank Prof. Knights for those industrial opportunities he has provided to me during the past years so that I can leave school with invaluable real-word experiences.

I also would like to thank Prof. Shiva Kumar who served as my supervisory committee member and made a tremendous contribution to my work. Prof. Kumar had many fruitful discussions with me and helped me with his coding on fiber-optics communication system. His work has given me a better understanding of his field and inspired my own coding work that was indispensable for my PhD research.

I also want to say thank you to all my colleagues in Knights group: Dr. Edgar Huante-Cerón, Dixon Paez, David Hagan, Jason Ackert, Jimmy Zheng, Kyle Murray Liam Dow and many other people for their assistances and friendships over these years. A special thanks to Dr. Edgar Huante-Cerón who helped me with his incredible expertise, knowledge and skill during my first year at McMaster.

My thesis work also relied on collaborations with Prof. John Cartledge from Queen's University. I would like to thank Prof. Cartledge for his advice, insight and guidance on high-speed communication systems and DSP techniques. Many experimental results in this thesis could not be achieved without those state-of-art instruments provided by Prof. Cartledge. Thanks to Prof. Cartledge's students, who offered their helps to me during my several extended visits to Queen's University. Thanks to Dr. Dan Deptuck

from CMC Microsystems for his coordination on the IME fabrication. Thanks to Prof. Lukas Chrostowski from University of British Columbia. He is the organizer and instructor (among others) for the Si-EPIC program from which I have received scholarship, training and other resources that have provided useful lessons in the field of silicon photonics.

I want to thank my family, especially my wife Joyce for her unconditional support along the road to my PhD. Her love, tolerance and understanding have kept me fighting without fear. Thanks to my parents, who made me what I am today, who supported me financially and emotionally since the day I decided to go abroad to pursue my dream. Thanks to Jasmine and Marshall, who treated me like their own son. Finally, thanks to all my relatives from China, who always cared about me and warmed my heart.

Table of Contents

List of Figures

Chapter 1 Introduction

1.1 Optical interconnect and silicon photonics

1.1.1 The need for optical interconnect in the cloud age

The advent of optical interconnect can be dated to the early-2000s with the aim for seeking replacement of electrical I/O for data centres [1, 2]. An optical solution became imperative after a wave of bandwidth-demanding internet services such as high-performance computing, cloud, high-definition video-on-demand, etc., began to emerge in the late-2000s. According to the Cisco Global Cloud Index white paper [3], the global data centre IP traffic (including both intra-data centre traffic and extended-reach traffic linked to the data centre) that accounts for the majority of the total data centre traffic first entered the Zettabyte (10^{21} bytes) era in the year 2010 and is projected to reach 15.3 Zettabytes by the end of 2020, with a compound annual growth rate of about 30 percent over 10 years. Enabling such enormous data throughput must be met with a scalable I/O technology in terms of bandwidth and power consumption.

Intra/inter-chip electrical interconnect is known to be the major performance bottleneck in high-speed systems in terms of power consumption [4], radio-frequency (RF) interference [5], transmission loss and bandwidth [6]. One notable example is the tradeoff between the bandwidth and reachable distance for RF signals transported in a conductive wire [7]: a higher bandwidth requires a shorter distance, which simply is not compatible with the data centre server design that consists of clustered line cards in a rack with a

backplane pooling resourced together through very long electrical wires. Other problems such as parasitic capacitance, skin-effect-induced RF resistance, impedance mismatch, etc., can also begin to limit the system performance as the speed increases. The conventional solution to overcome the capacity shortage in data centres by simply multiplying the number of servers becomes less and less economically viable due to the unsustainable power consumption associated with the insatiable demand for bandwidth.

Optical interconnect, a miniaturized optical communication system integrated on a small chip, consists of a number of integrated photonics components such as a laser, modulator, passive waveguide and photodetector to form a short-reach optical I/O link [8]. Switching the communication into the optical domain can provide a superior performance that mitigates the technological obstacles residing in the electronic interconnect [9, 10]. One of the major advantages for utilizing optical carriers to transport information is the inherent parallelism that allows the system bandwidth to be aggregated on a single bus by *wavelength division multiplexing* (WDM). Therefore, it provides the bandwidth scalability much desired for high-throughput interconnect. Optical signal propagation over a short distance typically experiences very low loss and low chirp, resulting in low signal distortion thus preserving the signal integrity. The optical signal propagating in the non-conductive dielectric waveguide is also immune to RF noise and interference, which can allow a tight arrangement for parallel arrays in terms the of optical I/O bus in a small area without introducing crosstalk issues. The time delay caused by propagation in a fixed optical link is also predictable owing to the known optical impedance for a given wavelength regardless of the bandwidth of the signal. Moreover, optical signal propagation in dielectric does not produce resistive heating, leading to negligible power dissipation that has become a major issue for hyper-scaled data centres.

1.1.2 Silicon photonics as a preferred material platform

Optical interconnect can be realized by several competing technologies using different material platforms such as III-V compounds, silicon, polymer or hybrid [11–13]. Though a comparable performance can be achieved among these technologies, the cost associated with large-volume production must be taken into consideration owing to the extremely cost-sensitive environment in data centre deployment. Since its inception in the late 1980s, silicon photonics has quickly received a wide popularity from IT industries because the fabrication of silicon photonics using silicon-on-insulator (SOI) is compatible with the *complementary-metal-oxide-semiconductor* (CMOS) fabrication techniques [14–16]. Therefore, by leveraging maturely developed CMOS foundries, silicon photonic devices can be fabricated on the wafer level at relatively low cost.

However, producing small-quantities of silicon photonic chip for research exploration using state-of-art equipment is still expensive for less-funded academic groups. Fortunately, silicon photonic designers can have public access to the *multiple-purpose-wafer* (MPW) service offered by some international CMOS foundries such IMEC, IME, MOSIS, etc. [17]. The MPW service allows multiple designs to be combined onto a single mask so that the cost for each fabrication is shared by different groups. The advantage of the MPW service is that the fabrication process is well-controlled and the resulting device can be expected to have a relatively predictable and stable performance, whereas the disadvantage is that it gives less flexibility for varying the fabrication process (e.g. changing the doping centration) so that the device performance may not be optimized [18].

One drawback in silicon photonics is a lack of optical gain since silicon is an indirect bandgap semiconductor. Although direct growth of III-V gain material on silicon

has been demonstrated [19], the resulting efficiency is not sufficient for commercial applications. The practical approach is through hybrid integration for which the optical source is coupled into the silicon chip by either chip bonding or free-space coupling such as end-to-end butt coupling. Laser source packaging has become the main limitation for the mass production of silicon photonics system in terms of yield and cost.

1.1.3 Building blocks of silicon photonics system

Silicon photonic building blocks contain a number of passive and active components such as waveguide, grating coupler, modulator and photodetector shown in Figure 1.1. Early research predominantly focused on the theoretical study and the realization of these individual components [20]. Nowadays, these building blocks are commonly available in the *process-design- kit* (PDK) provided by the foundries so that chip designers now concentrate on building advanced systems [21].

One major success in silicon photonics is associated with the low-loss SOI channel waveguide, which exploits a high refractive index contrast between silicon and silicon dioxide. This leads to strong optical confinement, a prerequisite for a low-loss optical routing especially when tight bends (>10 μm) are involved in a limited chip space. As shown in Figure 1.1, the starting materiel in the SOI platform is thin-layer of silicon (220 nm). The underneath BOX layer (silicon dioxide) normally has a thickness of a few microns in order to avoid an excessive mode leakage into the substrate. A silicon channel waveguide is thus obtained by a full etch process that results in a strong optical confinement. The mode property completely depends on the waveguide geometry, the theory of which will be discussed in detail in Chapter 2. Another important passive component is the grating coupler [22] responsible for coupling in/out light between the

external fiber and the silicon waveguide. A low-loss, low-reflection and broadband grating coupler is generally desirable in the silicon photonics system.

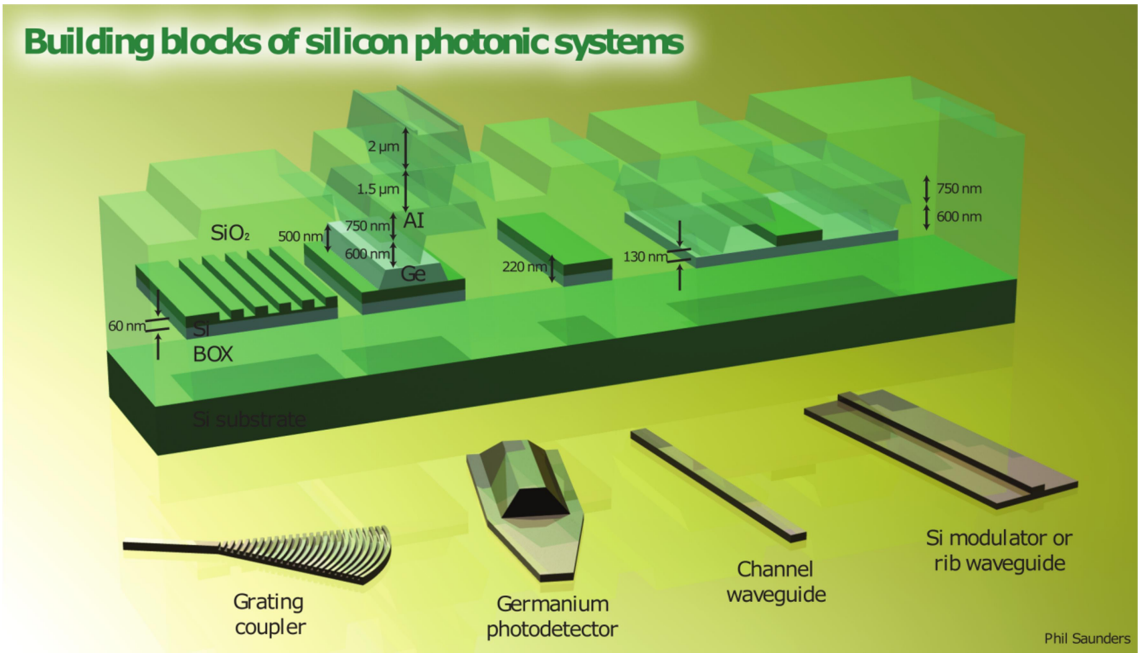

Figure 1.1 Building blocks for silicon photonics system. Figure reproduced with permission from OPN/Phil Saunders.

Silicon is known to be transparent to communication wavelengths. The dominant photo-detection mechanism in SOI is achieved by heterogeneous integration of germanium on silicon via epitaxial growth [24], thereby resulting in a structure for the germanium photodetector shown in Figure 1.1. For optical absorption, carriers are generated by absorption of the evanescent field that escapes into the germanium layer and are subsequently swept out by an electric field through a p-i-n junction configuration where the intrinsic region (that below the germanium layer) can be lightly doped in order to increase the conductivity [25]. Photo-detection in SOI can be also achieved via a monolithic approach. This mechanism is known as defect-mediated photo-detection [26].

By intentionally introducing defects in the silicon, an intermediate energy level can be formed so that electrons in the valence band can be excited by photo-absorption.

Modulation in SOI is enabled by a phase shifter that explores the plasma dispersion effect [27] where a change of carrier density leads to a change of refractive index. The SOI phase shifter is usually constructed using a rib waveguide in which a junction can be embedded in the core by ion implantation and the carrier density is manipulated by the electrical signal. A slab layer is implemented to provide an electrical access to the core. To translate phase modulations into intensity modulations, interferometric structures have to be deployed, which then can be generally divided into two categories: non-resonant type and resonant type.

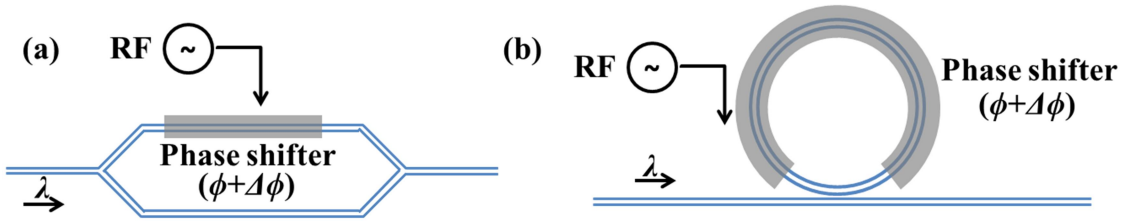

Figure 1.2 (a) Symmetric Si-MZM with two equal arms. (b) All-pass Si-MRR. ϕ is the constant phase shift for both unmodulated optical path while $\Delta\phi$ is the RF-signal induced phase modulation.

As shown in Figure 1.2 (a), the most recognized non-resonator type of modulator is the silicon Mach-Zehnder modulator (Si-MZM) that is known for its large optical bandwidth, insensitivity to temperature fluctuation (for symmetric configuration) and tolerance to fabrication uncertainty [28–31]. If both arms embed phase shifters with equal length, Si-MZM can potentially achieve chirp-free modulation under push-pull drive, favorable for medium/long-reach transmission. However, there are also some drawbacks making the Si-MZM less appealing for short-reach communications. For instance, since the plasma dispersion effect is quite weak, the typical length of the Si-MZM is several

millimeters in order to achieve a low-V_π (e.g. < 2.5 V, a value that is normally the maximum voltage provided by a CMOS chip) modulation. MZMs consume relatively large energy (>1 pJ/bit) due to the capacitance inherited from the long junction. In addition, transmission line electrodes are also needed to avoid a group velocity mismatch between the RF signal and optical signal.

The silicon micro-ring resonator (Si-MRR) modulator [32–34] is an example of a resonant-type modulator as shown in Figure 1.2 (b). Si-MRR modulator is known for its small footprint (typical radius is below 30 μm) and small power consumption (<100 fJ/bit) due to the resonant enhancement provided by the ring cavity [35]. One of the major drawbacks for the Si-MRR modulator, however, is large susceptibility to the thermal fluctuation and a total optical bandwidth limited by the periodicity of the resonance. As a result, there will be additional power required to align the resonance to the laser wavelength via a micro-heater and maintain the resonance during the high-speed operation by a feedback control loop. The characteristics of the Si-MRR will be discussed throughout the thesis.

Compared to the Si-MZM, the Si-MRR modulator can build a much more elegant WDM system with a small footprint that uses less optical sources and accordingly requires less power consumption. In a Si-MZM WDM system as sketched in Figure 1.3 (a), a parallel-channel configuration must be adopted, pairing with multiple laser sources. If a single output is desired, a multiplexer is also needed, which increases the design complexity. In contrast, the same WDM system based on Si-MRR modulators, shown in Figure 1.3 (b), has a much simpler design where multiple Si-MRR modulators can be serially cascaded on a single bus waveguide with each Si-MRR modulator being operated in the allocated channel without crosstalk, resulting from the wavelength-selection

capability provided by the ring resonator [36, 37]. Therefore, a single laser source such as a Fabry-Pérot laser diode can be deployed to provide multiple desired wavelengths in the same bus waveguide, thereby leading to a much more energy-efficient system ideal for short-reach communication [38].

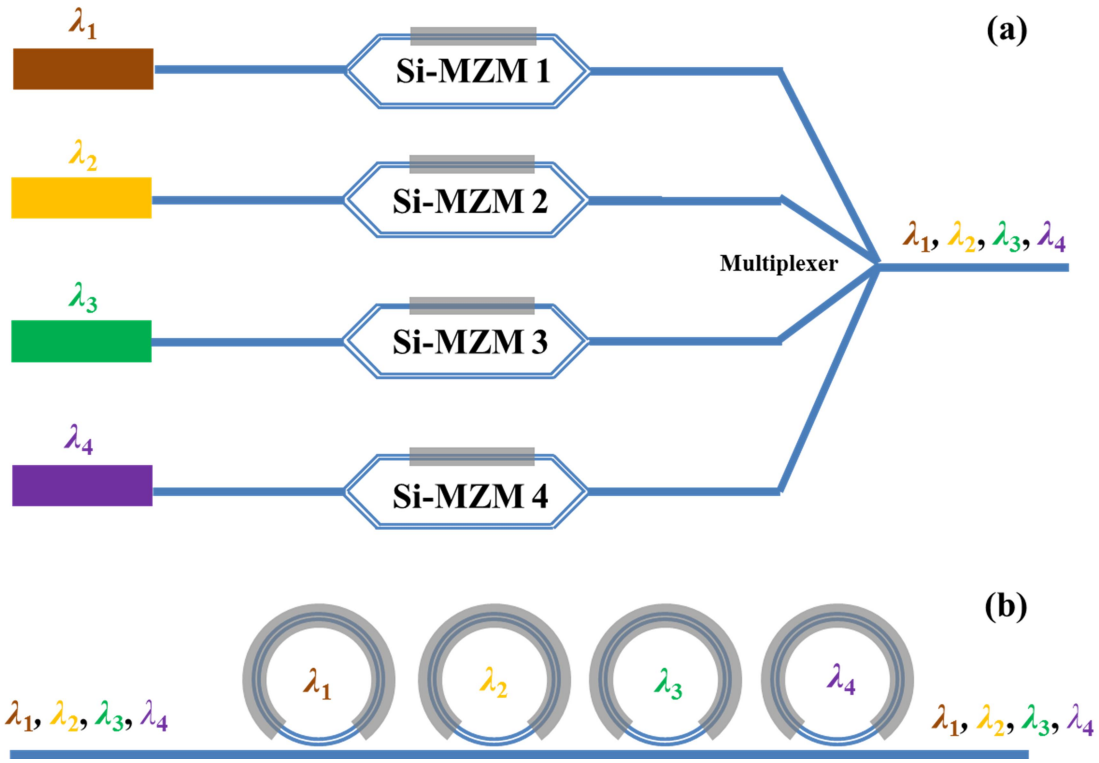

Figure 1.3 Four-channel WDM systems (a) based on parallel Si-MZMs with four independent laser sources and a multiplexer; (b) based on cascaded Si-MRRs in a single-input and single-output configuration with a multi-mode laser source. Drawing is not to scale.

1.2 Statements of thesis work

The contents presented in this thesis work resulted from my original work, guided by Prof. Andy Knights and Prof. Daniel Cassidy. Much of the work also relied on support from other personnel. In Chapter 2, simulations that involve analytical mode calculation (in section 2.1) and plasma dispersion effect (in section 2.2) were originally provided by

Prof. Lukas Chrostowski and Dr. Wei Shi during the Si-EPIC training workshop that I attended in 2013. The corresponding scripts compiled in MATLAB® can be accessed from [39]. Simulation codes developed in section 2.2 and 2.3 have undergone significant modifications by me to arrive at their current form. System-level simulations were completed with assistance from Prof. Shiva Kuma who provided me with his fiber-optic system coding to which I have made significant modifications. The theoretical guidance related to section 2.4 can be found in [40]. My other contribution to the modeling is the end-to-end system-level simulation providing a performance evaluation of the Si-MRR modulator in an extended transmission link. In particular, I contributed the simulation that obtains the dynamic response of the Si-MRR modulator, which serves as the link between the device-level simulation and system-level simulation.

In Chapter 3, the Si-MRR device was originally designed by Dr. Edgar Huante-Cerón for applications in high-speed short- reach links, but without the aim to study dispersion. I conceived the idea for studying the chirp characteristic, developed the measurement methodology and performed the theoretical chirp analysis. The high-speed measurement was conducted at Queen's University by me during several extended visits, where I was helped by Prof. John Cartledge and his students.

In Chapter 4, the work relied on collaboration again with Prof. John Cartledge's group at Queen's University. The experimental work presented in section 4.2 was performed by me together with Dr. Yuliang Gao who also contributed the DSP control.

In Chapter 5, I originally proposed the idea and developed the resonance control algorithm. Prof. John Cartledge and his students provided me with help on high-speed measurements during an extended visit to Queen's University.

1.3 Publications

Journal papers that contribute the thesis work are listed as follows:

Z. Wang, Y. Gao, J. C. Cartledge, E. Huante-Cerón, D. Logan, and A.P. Knights, "DSP-enabled 104 Gb / s 16-QAM Nyquist subcarrier modulation using a silicon micro-ring resonator," *IEEE photonics Technol. Lett*., 2017. (Intend to submit)

Z. Wang, D. Paez, A. El-Rahman, P. Wang, L. Dow, J. C. Cartledge, and A. P. Knights, "Resonance control of a silicon micro-ring resonator modulator under high-speed operation using the intrinsic defect-mediated photocurrent," *Opt. Express*, 2017. (Submitted)

Z. Wang, Y. Gao, A. S. Kashi, J. Cartledge, and A.P Knights, "Silicon micro-ring modulator for dispersion uncompensated transmission applications," *J. Light. Technol.,* vol. 34, no. 16, pp. 3675–3681, 2016.

Conference proceedings that also part of the thesis work are listed as follows:

Z. Wang, D. J. Paez, L. Dow, and A. P. Knights, "Intrinsic resonance stabilization in depletion-type silicon micro-ring modulators." in *IEEE 14th International Conference on Group IV Photonics (GFP)*, Berlin, 2017. (Accepted)

Y. Gao, **Z. Wang**, J. C. Cartledge, S. Yam, and A.P. Knights, "56 Gb/s Single-Carrier 16-QAM and 32-QAM Subcarrier Modulation Using a Silicon Micro-Ring Resonator," in *Optical Fiber Communication Conference*, 2017, p. Th1B.2.

Z. Wang and A. P. Knights, "Using the intrinsic properties of silicon micro-ring modulators for characterization of RF termination," in *Proc. SPIE 10107, Smart Photonic and Optoelectronic Integrated Circuits XIX*, 2017, p. 101070G.

Z. Wang and A. P. Knights, "Dual-ring-Assisted MZI silicon modulator for enhanced intensity modulation," in *IEEE 13th International Conference on Group IV Photonics (GFP)*, Shanghai, 2016, pp. 88–89.

Z. Wang, E. Huante-Ceron, A. P. Knights, A. S. Karar, and J. C. Cartledge, "High-speed low-voltage BPSK modulation using a silicon micro-ring resonator," in *11th International Conference on Group IV Photonics (GFP)*, Paris, 2014, pp. 51–52.

Reference

[1] N. Savage, "Linking with light [high-speed optical interconnects]," *IEEE Spectr.*, vol. 39, no. 8, pp. 32–36, Aug. 2002.

[2] M. J. Kobrinsky, A. B. Block, J. Zheng, B. C. Barnett, E. Mohammed, M. Reshotko, F. Robertson, S. List, I. Young, and K. Cadien, "On-chip optical interconnects," *Intel Technol. J.*, vol. 8, no. 2, pp. 129–141, 2004.

[3] Cisco White Paper, "Cisco Global Cloud Index: Forecast and Methodology, 2015-2020," 2015.

[4] H. Cho, P. Kapur, and K. C. Saraswat, "Power comparison between high-speed electrical and optical interconnects for interchip communication," *J. Light. Technol.*, vol. 22, no. 9, pp. 2021–2033, Sep. 2004.

[5] R. Khazaka and M. Nakhla, "Analysis of high-speed interconnects in the presence of electromagnetic interference," *IEEE Trans. Microw. Theory Tech.*, vol. 46, no. 7, pp. 940–947, Jul. 1998.

[6] R. H. Havemann and J. A. Hutchby, "High-performance interconnects: an integration overview," *Proc. IEEE*, vol. 89, no. 5, pp. 586–601, May 2001.

[7] R. L. Freeman, *Fundamentals of Telecommunications*. New York, USA: John Wiley & Sons, Inc., 1999.

[8] A. F. Benner, M. Ignatowski, J. A. Kash, D. M. Kuchta, and M. B. Ritter, "Exploitation of optical interconnects in future server architectures," *IBM J. Res. Dev.*, vol. 49, no. 4.5, pp. 755–775, Jul. 2005.

[9] J. Baliga, K. Hinton, R. Parthiban, R. W. A. Ayre, R. S. Tucker, W. Sorin, and V., "Evolution of WDM optical IP networks: A cost and energy perspective," *J. Light. Technol.*, vol. 27, no. 3, pp. 243–252, Feb. 2009.

[10] M. Asghari and A. V Krishnamoorthy, “Silicon photonics: Energy-efficient communication,” *Nat. Photonics*., vol. 5, no. 5, pp. 268–270, May. 2011.

[11] Y. Arakawa, T. Nakamura, Y. Urino, and T. Fujita, “Silicon photonics for next generation system integration platform,” *IEEE Commun. Mag.*, vol. 51, no. 3, pp. 72–77, 2013.

[12] G. Roelkens, L. Liu, D. Liang, R. Jones, A. Fang, B. Koch, and J. Bowers, “III-V/silicon photonics for on-chip and intra-chip optical interconnects,” *Laser Photon. Rev.*, vol. 4, no. 6, pp. 751–779, Nov. 2010.

[13] R. Dangel, C. Berger, R. Beyeler, L. Dellmann, M. Gmur, Ré. Hamelin, F. Horst, T. Lamprecht, T. Morf, S. Oggioni, M. Spreafico, and B. J. Offrein, “Polymer-waveguide-based board-level optical interconnect technology for Datacom applications,” *IEEE Trans. Adv. Packag.*, vol. 31, no. 4, pp. 759–767, Nov. 2008.

[14] B. Jalali and S. Fathpour, “Silicon photonics,” *J. Light. Technol. Vol. 24, Issue 12, pp. 4600-4615*, vol. 24, no. 12, pp. 4600–4615, Dec. 2006.

[15] A. Rickman, “The commercialization of silicon photonics,” *Nat. Photonics*, vol. 8, no. 8, pp. 579–582, 2014.

[16] D. A. B. Miller, “Optical interconnects to silicon,” *IEEE J. Sel. Top. Quantum Electron.*, vol. 6, no. 6, pp. 1312–1317, Nov. 2000.

[17] M. Hochberg, N. Harris, R. Ding, Y. Zhang, A. Novack, Z. Xuan, and T. Baehr-Jones, “Silicon photonics: The next fabless semiconductor industry,” *IEEE Solid-State Circuits Mag.*, vol. 5, no. 1, pp. 48–58, 2013.

[18] A. E. J. Lim, J. Song, Q. Fang, C. Li, X. Tu, N. Duan, K. K. Chen, R. P. C. Tern, and T. Y. Liow, “Review of silicon photonics foundry efforts,” *IEEE J. Sel. Top. Quantum Electron.*, vol. 20, no. 4, pp. 405–416, 2014.

[19] S. Chen, W. Li, J. Wu, Q. Jiang, M. Tang, S. Shutts, S. N. Elliott, A. Sobiesierski, A. J. Seeds, I. Ross, P. M. Smowton, and H. Liu, “Electrically pumped continuous-wave III–V quantum dot lasers on silicon,” *Nat. Photonics*, vol. 10, no. 5, pp. 307–311, 2016.

[20] R. Soref, “The past, present, and future of silicon photonics,” *IEEE J. Sel. Top. Quantum Electron.*, vol. 12, no. 6, pp. 1678–1687, 2006.

[21] M. Hochberg and T. Baehr-Jones, “Towards fabless silicon photonics,” *Nat. Photonics*, vol. 4, no. 8, pp. 492–494, Aug. 2010.

[22] A. Mekis, S. Gloeckner, G. Masini, A. Narasimha, T. Pinguet, S. Sahni, and P. De Dobbelaere, "A grating-coupler-enabled CMOS photonics platform," *IEEE J. Sel. Top. Quantum Electron.*, vol. 17, no. 3, pp. 597–608, May 2011.

[23] M. Streshinsky, R. Ding, Y. Liu, A. Novack, C. Galland, A. E.-J. Lim, P. Guo-Qiang Lo, T. Baehr-Jones and M. Hochberg, "The road to affordable, large-scale silicon photonics," *Opt. Photonics News*, vol. 24, no. 9, pp. 32–39, 2013.

[24] J. Michel, J. Liu, and L. C. Kimerling, "High-performance Ge-on-Si photodetectors," *Nat. Photonics*, vol. 4, no. 8, pp. 527–534, Aug. 2010.

[25] S. J. Koester, J. D. Schaub, G. Dehlinger, and J. O. Chu, "Germanium-on-SOI infrared detectors for integrated photonic applications," *IEEE J. Sel. Top. Quantum Electron.*, vol. 12, no. 6, pp. 1489–1502, Nov. 2006.

[26] B. Desiatov, I. Goykhman, J. Shappir, and U. Levy, "Defect-assisted sub-bandgap avalanche photodetection in interleaved carrier-depletion silicon waveguide for telecom band," *Appl. Phys. Lett.*, vol. 104, no. 9, 2014.

[27] R. Soref and B. Bennett, "Electrooptical effects in silicon," *IEEE J. Quantum Electron.*, vol. 23, no. 1, pp. 123–129, Jan. 1987.

[28] S. Akiyama, T. Baba, M. Imai, T. Akagawa, M. Takahashi, N. Hirayama, H. Takahashi, Y. Noguchi, H. Okayama, T. Horikawa, and T. Usuki, "125-Gb/s operation with 029-V·cm V_πL using silicon Mach-Zehnder modulator based-on forward-biased pin diode," *Opt. Express*, vol. 20, no. 3, p. 2911, Jan. 2012.

[29] D. J. Thomson, F. Y. Gardes, G. T. Reed, F. Milesi, and J.-M. Fedeli, "High speed silicon optical modulator with self aligned fabrication process.," *Opt. Express*, vol. 18, no. 18, pp. 19064–9, Aug. 2010.

[30] L. Liao, D. Samara-Rubio, M. Morse, A. Liu, D. Hodge, D. Rubin, U. Keil, and T. Franck, "High speed silicon Mach-Zehnder modulator.," *Opt. Express*, vol. 13, no. 8, pp. 3129–35, Apr. 2005.

[31] P. Dong, L. Chen, and Y. Chen, "High-speed low-voltage single-drive push-pull silicon Mach-Zehnder modulators," *Opt. Express*, vol. 20, no. 6, pp. 6163–6169, 2012.

[32] P. Dong, R. Shafiiha, S. Liao, H. Liang, N.-N. Feng, D. Feng, G. Li, X. Zheng, A. V Krishnamoorthy, and M. Asghari, "Wavelength-tunable silicon microring modulator.," *Opt. Express*, vol. 18, no. 11, pp. 10941–6, May 2010.

[33] F. Y. Gardes, a Brimont, P. Sanchis, G. Rasigade, D. Marris-Morini, L. O'Faolain, F. Dong, J. M. Fedeli, P. Dumon, L. Vivien, T. F. Krauss, G. T. Reed, and J. Martí,

"High-speed modulation of a compact silicon ring resonator based on a reverse-biased pn diode.," *Opt. Express*, vol. 17, no. 24, pp. 21986–91, Nov. 2009.

[34] Q. Xu, S. Manipatruni, and B. Schmidt, "12.5 Gbit/s carrier-injection-based silicon micro- ring silicon modulators," *Opt. Express*, vol. 15, no. 2, pp. 430–436, 2007.

[35] G. T. Reed, G. Mashanovich, F. Y. Gardes, and D. J. Thomson, "Silicon optical modulators," *Nat. Photonics*, vol. 4, no. 8, pp. 518–526, Jul. 2010.

[36] S. Manipatruni, L. Chen, and M. Lipson, "Ultra high bandwidth WDM using silicon microring modulators.," *Opt. Express*, vol. 18, no. 16, pp. 16858–67, Aug. 2010.

[37] Q. Xu, B. Schmidt, J. Shakya, and M. Lipson, "Cascaded silicon micro-ring modulators for WDM optical interconnection.," *Opt. Express*, vol. 14, no. 20, pp. 9431–9435, 2006.

[38] G. Li, A. V Krishnamoorthy, I. Shubin, J. Yao, Y. Luo, H. Thacker, X. Zheng, K. Raj, and J. E. Cunningham, "Ring resonator modulators in silicon for interchip photonic links," *IEEE J. Sel. Top. Quantum Electron.*, vol. 19, no. 6, pp. 95–113, 2013.

[39] L. Chrostowski and M. Hochberg, *Silicon photonics design*. Cambridge, UK: Cambridge University Press, 2015.

[40] S. Kumar and M. J. Deen, *Fiber optic communications: fundamentals and applications*. Chichester, West Sussex, UK: John Wiley & Sons Inc., 2014.

Chapter 2 Theoretical considerations enabling predictive modeling of silicon photonics modulation

Simulation and modeling in silicon photonics is increasing in importance as more emphasis is placed on device deployment via large-scale manufacturing [1]. In a similar manner to the microelectronics industry, the need for accurate, predictive modeling of device variations or modifications is required to avoid unreasonable costs associated with experimental, exploratory investigation. The result of good modeling can increase yield of fabrication or lead to new devices or operational methods.

Section 2.1 provides an introduction to guided wave theory based on the electromagnetic treatment in [2]. The effective index method (EIM) is used to demonstrate a means to compute the optical mode profile as well as the effective index. In addition, the reader is referred to [3] for a ray-optics approach for the understanding of optical propagation in a waveguide. Section 2.2 describes p-n junction physics and the analytical model for a depletion-type p-n junction that serves as a phase shifter in silicon photonics. Section 2.3 focuses on the silicon micro-ring resonator (Si-MRR) modulator related to the majority of the content in this thesis. Both the static response and the time-resolved dynamic response are studied in order to understand the performance of the device. Together, these theoretical considerations are combined by the author to produce a model for the Si-MRR modulator based on an analytical form. As a result, an efficient model is presented which dramatically reduces the computation time, while maintaining

satisfactory results for the device performance prediction without the need of time-consuming numerical simulations.

2.1 Analytical solution for mode profile

2.1.1 Guided wave in a 2-D slab waveguide

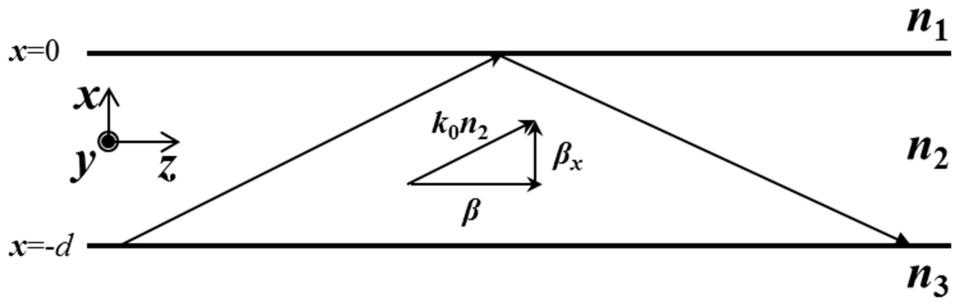

Figure 2.1 Slab waveguide.

Optical waveguides are an indispensable passive component in photonic systems and are used to confine and guide an optical wave. In general, an optical waveguide has a spatially inhomogeneous profile of refractive index where the core has a higher refractive index than the cladding. The optical confinement can be understood, from a ray-optics perspective, as the result of total internal refraction, a phenomenon in which light is totally reflected at the boundary of two materials when traveling from a dense medium to a less dense medium with the incident angle larger than the critical angle [4]. A simple 2-D slab waveguide, as shown by Figure 2.1, consists of three homogeneous and isotropic dielectric layers extending to infinity ($z \rightarrow +\infty$). The refractive index of the core (n_2) is larger than the refractive indices of the claddings (n_1, n_3), leading to a confinement along

the *x*-direction. Considering the waveguide is homogenous along the *z*-direction, the scalar wave equation can be given by:

$$\left(\frac{\partial^2}{\partial x^2}+\frac{\partial^2}{\partial y^2}\right)E(x,y)+\left[\left(k_0\right)^2 n-\beta^2\right]E(x,y)=0 \tag{2.1}$$

where k_0 is the wavenumber in vacuum and equal to ω/c and β is the propagation constant in the *z*-direction (or the *z* component of $k_0 n_2$ as shown in Figure 2.1). An important quantity, effective index n_{eff}, can be deduced:

$$n_{eff}=\frac{\beta}{k_0} \tag{2.2}$$

An optical mode is commonly referred to as an electromagnetic field profile in the transverse plane (perpendicular to the *z*-direction) that results from the boundary conditions of the waveguide. The optical mode must be a static solution of the wave equation or in other words, it must form a standing wave in the transverse plane. The boundary condition imposes that the field (tangential components of E- and H- fields) must be continuous across the boundary, leading to a small portion of energy propagating in the cladding layer. However, the field in the cladding must be exponentially decaying in order to satisfy the law of energy conservation and thus it is named as the evanescent field. Since the sign of $\left(\left(k_0\right)^2 n-\beta^2\right)$ will determine if the field is oscillating (confined) or exponentially decaying, n_{eff} must be constrained such that:

$$\max\left(n_1,n_3\right)<n_{eff}<n_2 \tag{2.3}$$

so that the optical field is confined in the core ($\left(\left(k_0\right)^2 n_2-\beta^2\right)>0$) but exponentially decaying in the cladding ($\left(\left(k_0\right)^2 n_{1,3}-\beta^2\right)<0$). For the 2-D waveguide as shown in Figure 2.1, the transverse electrical (TE) mode is the mode profile along the *x*-direction

when the polarization of the E-field is along the y-direction; and a transverse magnetic (TM) mode is the mode profile along the *x*-direction when the polarization of the H-field is along the y-direction. For the TE mode, the E-field amplitude $E_y^m(x)$ has the following expressions:

$$E_y^m(x) = \begin{cases} C\exp(-qx), & x \geq 0 \\ C\left(\cos(hx) - \frac{q}{h}\sin(hx)\right), & -d \leq x \leq 0 \\ C\left(\cos(hd) + \frac{q}{h}\sin(hd)\right)\exp\left(p(x+d)\right), & x \leq -d \end{cases} \quad (2.4)$$

where the superscript *m* stands for the *m*-th mode, *d* is the thickness of the core layer, *C* is a normalization constant and *h*, *q*, *p* are defined as:

$$h = [(n_2 k_0)^2 - (n_{eff} k_0)^2]^{1/2},\ q = [(n_{eff} k_0)^2 - (n_1 k_0)^2]^{1/2},\ p = [(n_{eff} k_0)^2 - (n_3 k_0)^2]^{1/2} \quad (2.5)$$

The H-field amplitude $H_z^m(x) = i\omega\mu\,\partial E_y^m(x)/\partial x$ is then derived as:

$$H_z^m(x) = i\omega\mu \cdot \begin{cases} -qC\exp(-qx), & x \geq 0 \\ C\left(-h\sin(hx) - q\cos(hx)\right), & -d \leq x \leq 0 \\ pC\left(\cos(hd) + \frac{q}{h}\sin(hd)\right)\exp\left(p(x+d)\right), & x \leq -d \end{cases} \quad (2.6)$$

The boundary condition requires that both $E_y^m(x)$ and $H_z^m(x)$ (tangential components) be continuous at the interfaces $x = 0$ and $x = -d$. By using equations (2.4), (2.6) and applying the boundary condition, one can obtain the so-called mode-condition eigenfunction:

$$\tan(hd) = \frac{p+q}{h\left(1-pq/h^2\right)} \tag{2.7}$$

Eq. (2.7) has a finite number of solutions for n_{eff} as a result of the constraint imposed by Eq. (2.3). An example given in Figure 2.2 shows the computed E-field amplitudes of the TE-mode at a wavelength of 1.55 μm for a 2-D slab layer where n_1=1 (air), n_2=3.47 (Si), n_3=1.44 (SiO_2) and d=1 μm. Four solutions can be obtained from the mode-condition eigenfunction and the normalized E-field amplitudes for different modes are plotted along the propagation direction. It can be seen that each mode forms a standing wave in the transverse plane. The fundamental mode TE_0 is referred to as the mode with largest n_{eff}.

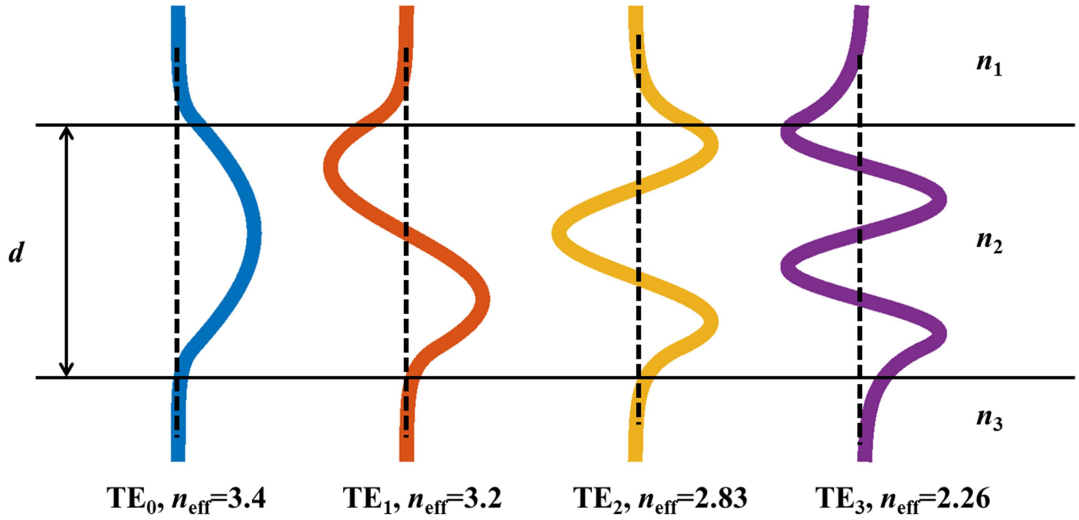

Figure 2.2 Confined TE-modes (plotted as E-field) in a slab waveguide.

A similar approach can be used to solve for the TM mode, using the boundary conditions on the two tangential components $H_y^m(x)$ and $E_z^m(x)$. Here only the final solutions for the model-condition eigenfunction and the E-field amplitude $E_x^m(x)$ are given. The mode-condition eigenfunction is defined as:

$$\tan(hd) = \frac{h\left(\frac{n_2^2}{n_3^2}p + \frac{n_2^2}{n_1^2}q\right)}{\left(h^2 - pq/h^2\right)} \tag{2.8}$$

and the E-field amplitude is expressed as

$$E_x^m(x) = \frac{1}{n_{eff}\varepsilon} \cdot \begin{cases} -\frac{n_1^2 h}{n_2^2 q} C\exp(-qx), & x \geq 0 \\ C\left(-\frac{n_1^2 h}{n_2^2 q}\cos(hx) + \sin(hx)\right), & -d \leq x \leq 0 \\ -C\left(\frac{n_1^2 h}{n_2^2 q}\cos(hd) + \sin(hd)\right)\exp\left(p(x+d)\right), & x \leq -d \end{cases} \tag{2.9}$$

2.1.2 Effective index method

Accurate analytical solutions cannot be found for the majority of 3-D waveguides (e.g. ridge waveguides) in which the confinement of light is two-dimensional. Numerical simulation such as *finite- difference-time-domain* (FDTD) method is needed to calculate the exact mode profile but is difficult to integrate into a fully analytical model. Alternatively, an analytical approximation, the *effective index method* (EIM) [5], can be used to compute the mode profile as well as the effective index. The principle of EIM is to convert a 2-D confinement into two separate 1-D problems with the approximation that the 2-D mode profile is separable in the orthogonal directions, such that $E(x,y) = E(x)E(y)$ by ignoring the vectored nature of the electromagnetic field [6]. The EIM treatment has been commonly used for solving for mode profiles in the rectangular waveguide that has a large aspect ratio (width to height); normally the case for the typical SOI waveguide in the integrated system.

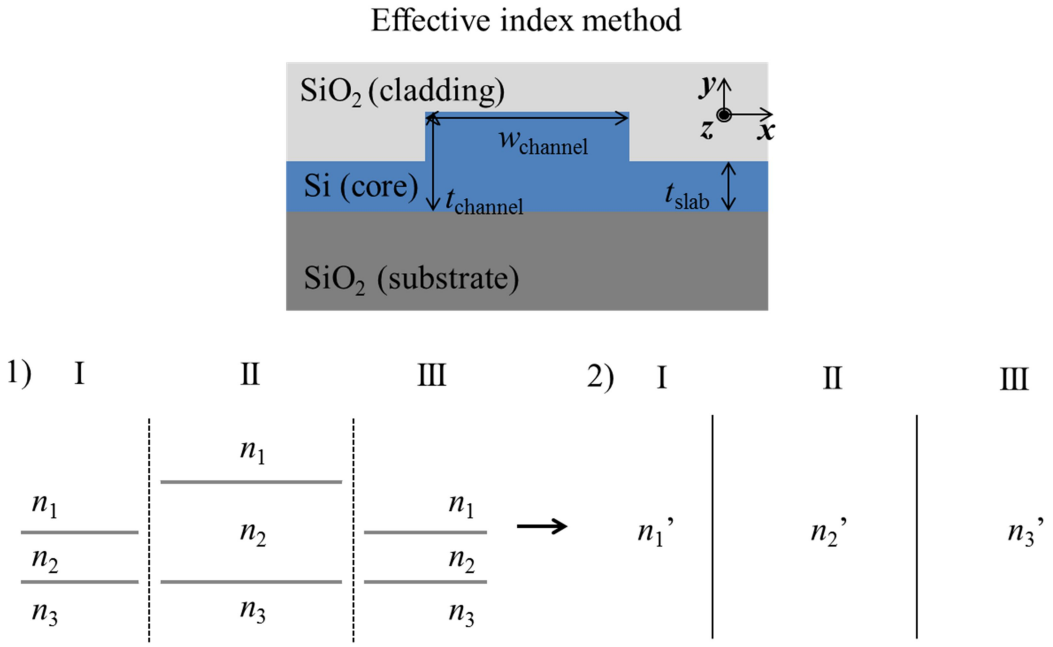

Figure 2.3 Illustration of using EIM on a SOI ridge waveguide.

A typical ridge waveguide is shown in Figure 2.3 (top) where the TE mode is defined when the polarization of the E-field is along the *x*-axis and the TM mode is defined when the polarization of the E-field is along the *y*-axis. Note that the definitions for TE and TM modes in the 3-D waveguide are different from those in the 2-D waveguide, which sometimes causes confusion. The use of the EIM treatment on decomposing the 2-D confinement into two orthogonal 1-D confinements is shown for the TE mode as an example. Firstly, the ridge waveguide is horizontally divided into three regions I, II and III, each of which is a 2-D slab waveguide with a vertical confinement along *y*-direction. Using the TE mode-condition eigenfunction Eq. (2.7), effective indices $n_1^{'}$, $n_2^{'}$, $n_3^{'}$ can be calculated for each region, which then constructs a new '2-D slab waveguide' with a horizontal confinement along the *x*-direction. The n_{eff} and the 1-D mode profile $E_x(x)$ can be calculated by the TM-mode equations (2.8) and (2.9), respectively. Similarly, the 1-D mode profile $E_x(y)$ in the orthogonal direction can be

directly obtained from the TE-mode equation Eq. (2.6) for the slab waveguide shown in region II so that the 2-D model profile can be constructed by $E_y(y) \times E_x(y)$. A similar treatment can be applied to obtain the 2-D TM mode that will not be shown in detail. The single-mode condition in the 3-D waveguide results from waveguide dimensions that support only one solution for each polarization (TE or TM) with the fundamental mode is normally refereed to the first TE mode. The majority of the SOI devices operate with the fundamental mode only. We restrict ourselves to consideration of the fundamental mode for this thesis while acknowledging that the results could be extended for higher modes.

As a comparison, the TE-mode profiles (intensity) acquired by the EIM and FDTD are shown in Figure 2.4 for the ridge waveguide in Figure 2.3 with a geometry of w_{channel}=500 nm, t_{channel}=220 nm and t_{slab}=90 nm. The main disagreement can be found at the waveguide edge between the channel and slab owing to the EIM approximation that does not properly deal with an abrupt interface change. This disparity is not particularly important for studying optical modulation that mostly takes place in the centre of the channel. The effective index n_{eff} and group index $n_g = n_{eff} - \lambda\, dn_{eff} / d\lambda$ are calculated to quantify the error introduced by the EIM. The material dispersion for Si from the wavelength of 1.5 μm to 1.6 μm is taken into account by using the Sellmeier equation [7]:

$$n^2(\lambda) = 1 + \frac{A_1\lambda^2}{\lambda^2 - B_1^2} + \frac{A_2\lambda^2}{\lambda^2 - B_2^2} + \frac{A_3\lambda^2}{\lambda^2 - B_3^2} \tag{2.10}$$

where coefficients (A_1, A_2 A_3) are (10.6684, 0.003043, 1.5413) and (B_1, B_2 B_3) are (0.3015, 1.1347, 1104). The inserted λ is in units of micrometer. The refractive index of SiO_2 is fixed at 1.44 due to the negligible dispersion for the same wavelength range.

The results for the simulation of n_{eff} and n_g obtained by EIM and FDTD simulation are provided in Figure 2.5 for comparison. Good agreement is reached with

only about 1.5 % difference between the two methods for n_{eff} and 0.1% for n_g for a wavelength of 1.55 μm.

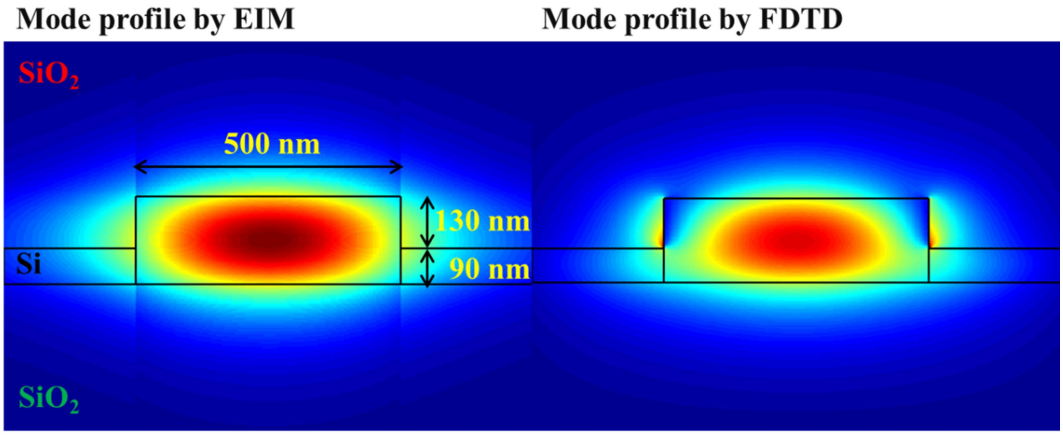

Figure 2.4 Mode profiles obtained by EIM and FDTD.

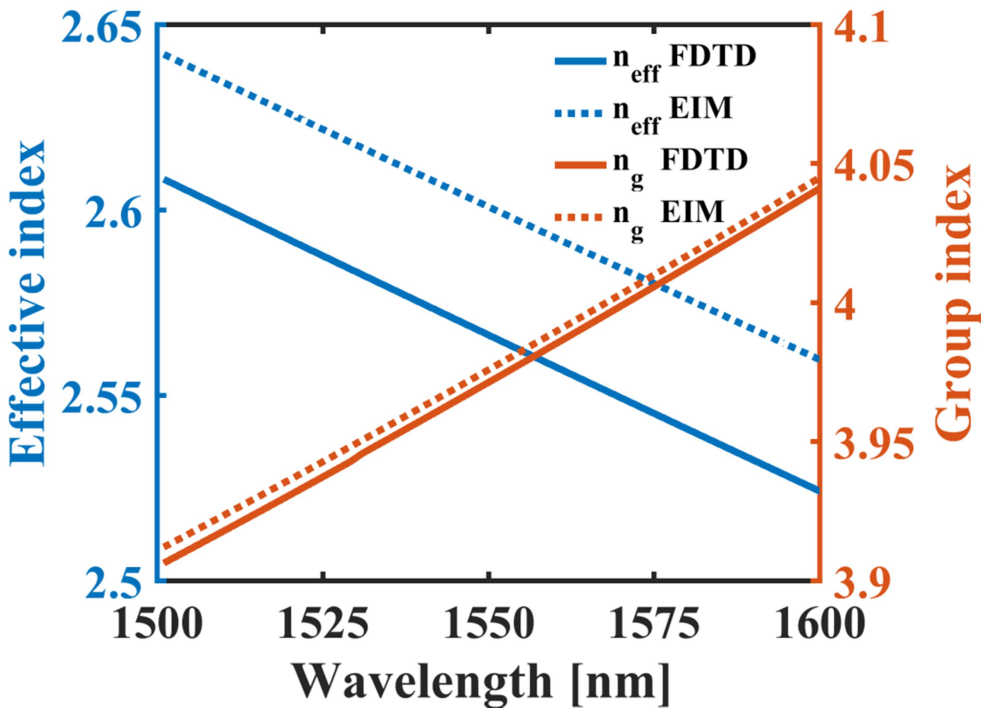

Figure 2.5 Effective index and group index estimation by EIM and FDTD.

2.2 Modulation in SOI waveguides

2.2.1 Plasma dispersion effect

In an optical transmission link employing external modulation, the optical modulator is the most important component, providing a means to encode electrical information onto an optical carrier. Through the electrical-to-optical (E/O) conversion, the intensity or phase of light may be modulated by an electrical signal. An electro-absorption modulator can directly modulate the intensity of light through varying the absorption spectrum of the material in response to an applied voltage, an effect known as the Franz-Keldysh effect. Another type of modulation can be achieved by an electro-optical phase shifter that modulates the real component of the refractive index of a material, and subsequently the phase of light guided within. State-of-art high-speed modulators used for optical fiber communications typically exhibit strong second-order nonlinearity, namely the Pockels effect, which is found to be very efficient in certain materials, for example Lithium Niobate ($LiNbO_3$) or III-V compounds (Indium Phosphide, Gallium Arsenide etc.) [8]. For the Pockels effect, the change of the real part of the refractive index is linearly proportional to the voltage via the second-order nonlinear coefficient, leading to a pure phase modulation.

Unfortunately, due to the centro-symmetry of silicon in the crystalline form, the second-order nonlinearity does not naturally exist in SOI waveguides although it can be introduced by strain engineering (which may be used to break the centro-symmetry) [9]. The third-order nonlinearity, namely the Kerr effect, is too weak to be practically used for modulation in SOI. It is noted that modulators made from a SiGe compound can achieve electro-absorption based modulation via the quantum-confined stark effect [10, 11].

However, the process of making a SiGe quantum-well waveguide is more sophisticated and not compatible with the CMOS fabrication technology currently used in the semiconductor industry.

Modulation in SOI is predominantly obtained by the plasma dispersion effect in which the presence of free carriers (electrons and holes) results in the optical modulation. This effect was first studied in detail for silicon in the landmark work of Soref and Bennet [12] about 30 years ago. Free carriers are introduced into the silicon waveguide via the process of ion implantation. The carrier-induced modulation on the complex refractive index $(n+i\kappa)$ are given by equations (2.11) and (2.12):

$$\Delta n = -3.64\times10^{-10}\lambda^2\Delta N - 3.51\times10^{-6}\lambda^2\Delta P^{0.8}[\mathrm{cm}^{-1}] \tag{2.11}$$

$$\Delta\alpha = 3.52\times10^{-6}\lambda^2\Delta N + 2.4\times10^{-}\lambda^2\Delta P\,[\mathrm{cm}^{-1}] \tag{2.12}$$

where Δn represents the change of the real part of the refractive index n and $\Delta\alpha$ is the change of material absorption coefficient associated with the imaginary part of the refractive index κ. The carrier concentration changes are given by ΔN for electrons and ΔP for holes. Note that the material dispersion has been considered in the above equations by following the Drude-model for a range of important communication wavelengths [13]. It should also be noted that the phase modulation and intensity modulation always accompany each other, which is generally undesirable.

Carrier concentration in SOI waveguides can be electrically manipulated by depletion, injection and accumulation, leading to three popular junction designs [14]: carrier-depletion based p-n junction, carrier-injection based p-i-n junction and carrier-accumulation based on p-oxide-n junction or metal-oxide-semiconductor (MOS) structure as schematically shown in Figure 2.6.

Each design has its own advantages and disadvantages. For instance, the carrier-injection junction operating under forward bias gives the most energy efficient modulation but has the smallest modulation bandwidth (<1 GHz) mainly limited by the minority recombination lifetime. The pre-emphasis technique [15] through which the frequency response of the low-speed p-i-n diode is equalized can be used to increase the speed of the recombination but this complicates the electrical driver design. On the contrary, carrier-depletion junctions under reverse bias has the smallest efficiency due to the small change of the carrier concentration near the depletion region, but this technique is generally most popular due to the large achievable bandwidths of tens of GHz [16]. The performance of the carrier-accumulation junction lies somewhat between the other two but this technique is limited in bandwidth due to the large capacitance caused by the thin oxide layer. The first-generation high-speed silicon modulators with bandwidths ranging from 1 GHz to 10 GHz were demonstrated by the Intel group between 2004 and 2005 and were based on an accumulation phase shifter [17, 18]. The depletion p-n junction has been widely accepted now as the dominant modulation mechanism for phase shifting in SOI as a result of the large achievable bandwidth and ease of fabrication. The focus of this thesis is modulation using the depletion p-n junction.

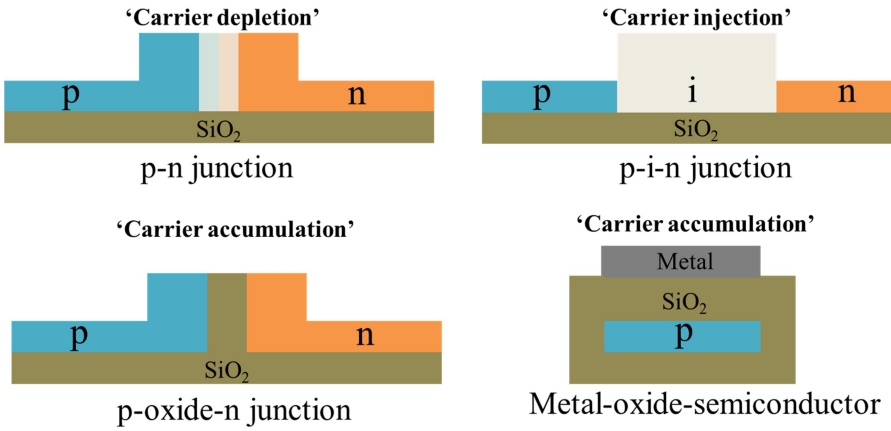

Figure 2.6 Carrier depletion, injection and accumulation and junction designs.

2.2.2 Depletion p-n junction modulation modeling

Since in the reverse bias p-n junction optical modulation is result for the interaction between free carriers and the optical field, one needs to obtain the carrier concentration across the whole junction under the reverse bias to adequately model device operation. More importantly, the geometry of the depletion region, where the predominant modulation occurs, needs to be well-defined. For a classical 1-D approach, the full depletion approximation assumes that there is an abrupt transition in terms of the carrier concentration at the boundary between the depleted region and the quasi-neutral region, which also means that no free carriers can exist in the depletion region. In addition, the width of the p-n junction is assumed to be much shorter than the carrier diffusion length, so that a linear profile can be applied for the minority carrier concentration from the depletion region to the doped region beyond [19].

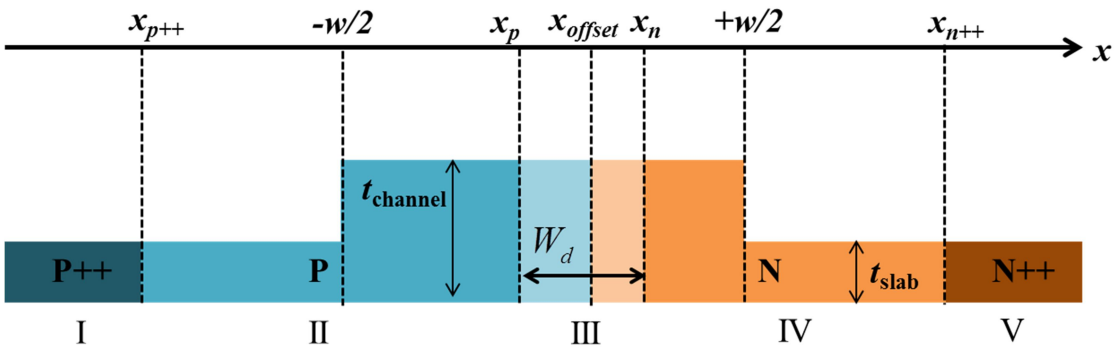

Figure 2.7 Depletion p-n junction in the 1-D analysis.

Figure 2.7 describes a depletion p-n junction where the carrier concentrations $n(x)$ (donor) and $p(x)$ (accepter) along the x-direction are solved. In the equilibrium state, the width of the depletion region W_d under the reverse bias voltage V is given as

$$W_d = \sqrt{\frac{2\varepsilon_0\varepsilon_s(N_D+N_A)(V_b-V)}{qN_DN_A}} \tag{2.13}$$

where ε_0 is the permittivity of vacuum (8.85×10^{-12} F/m^{-1}), ε_r is the relative permittivity for silicon (equal to 11.68), q is the electron charge (1.6×10^{-19} C), N_D and N_A are the concentrations for the donor and acceptor, respectively. The V_b is known as the built-in potential, defined as

$$V_b = \frac{k_B T}{q} \ln \frac{N_A N_D}{n_i^2} \tag{2.14}$$

where k_B is the Boltzmann constant (1.38×10^{-23} m^{2}kgs^{-2}K^{-1}), T is the temperature in Kelvin, and n_i is the intrinsic carrier concentration as a function of temperature:

$$n_i(T) = 5.29 \times 10^{19} \left(\frac{T}{300} \right)^{2.54} \exp(-\frac{6726}{T}) \tag{2.15}$$

As shown in Figure 2.7, a junction offset biased towards the n-doped region is defined so that the majority of the p-n junction is p-doped. This is because the concentration change for the hole, compared to the electron, will produce a larger refractive index change but causes a lower absorption, as indicated by equations (2.11) and (2.12). As a result, the boundary coordinates x_p *and* x_n for the p-doped and n-doped regions are given as:

$$x_p = x_{offset} - \frac{W_d}{1 + N_A / N_D} \tag{2.16}$$

$$x_n = x_{offset} + \frac{W_d}{1 + N_D / N_A} \tag{2.17}$$

Finally, voltage-dependent carrier concentrations $p(x,V)$ and $n(x,V)$ can be given in region I:

$$\begin{cases} p(x,V) = N_{A++} \\ n(x,V) \approx 0 \end{cases} \tag{2.18}$$

in region II:

$$\begin{cases} p(x,V) = N_A \\ n(x,V) = \dfrac{n_i^2}{N_P}\left[1+\left(1-\dfrac{x_p - x}{x_p - x_{p++}}\right)\right] e^{\left(\frac{qV}{k_B T}-1\right)} \end{cases} \tag{2.19}$$

in region III

$$\begin{cases} p(x,V) = 0 \\ n(x,V) = 0 \end{cases} \tag{2.20}$$

in region IV

$$\begin{cases} p(x,V) = \dfrac{n_i^2}{N_D}\left[1+\left(1-\dfrac{x - x_n}{x_{n++} - x_n}\right)\right] e^{\left(\frac{qV}{k_B T}-1\right)} \\ n(x,V) = N_D \end{cases} \tag{2.21}$$

and in region V

$$\begin{cases} p(x,V) \approx 0 \\ n(x,V) = N_{D++} \end{cases} \tag{2.22}$$

The 2-D carrier profiles $p(x,y)$ and $p(x,y)$ can be constructed by stacking of the 1-D carrier profile in the vertical direction under the full-depletion approximation. Using equations (2.11) and (2.12), the 2-D spatial profiles $n(x,y)$ and $\alpha(x,y)$ can be

calculated. As a result, the effective index change Δn_{eff} and the absorption change $\Delta \alpha_{pn}$ for the fundamental mode can be obtained by an overlap calculation between the spatial profiles $\langle n(x,y), \alpha(x,y) \rangle$ and the mode profile, given by:

$$\left\langle \Delta n_{eff}(x,y,V), \Delta \alpha_{pn}(x,y,V) \right\rangle = \frac{\iint \left\langle \Delta n(x,y,V), \Delta \alpha(x,y,V) \right\rangle \left| E(x,y) \right|^2 dxdy}{\iint \left| E(x,y) \right|^2 dxdy} \quad (2.23)$$

An example of this approach is given for a depletion p-n junction that has the same ridge waveguide structure as shown in Figure 2.4. The doping concentrations for the P++, P , N and N++ regions are assumed to be 1×10^{20} cm^{-3}, 0.5×10^{18} cm^{-3}, 3×10^{18} cm^{-3} and 1×10^{20} cm^{-3}, respectively. Heavy doping regions are 0.8 μm away from the waveguide edge to avoid unnecessary parasitic optical absorption. Three junction offsets 0 nm, 75 nm and 150 nm are considered in the simulation as a comparison. The simulated results for Δn_{eff} and $\Delta \alpha_{pn}$ with respect to the reverse bias up to -6 V for a wavelength of 1.55 μm are shown by Figure 2.8. It can be concluded that the largest modulation efficiency (Δn_{eff}) occurs at the junction offset of 75 nm, indicating that the corresponding depleted region has a better overlap with the center of the optical mode.

The modeling explained in this section is used for balancing the modulation efficiency and insertion loss of a particular modulator design, by examining different configurations for the doping concentration, the junction geometry and the junction offset [20]. It should be noted that the modeling could be also applied for solving geometries in the vertical p-n junction or the interdigitated p-n junction.

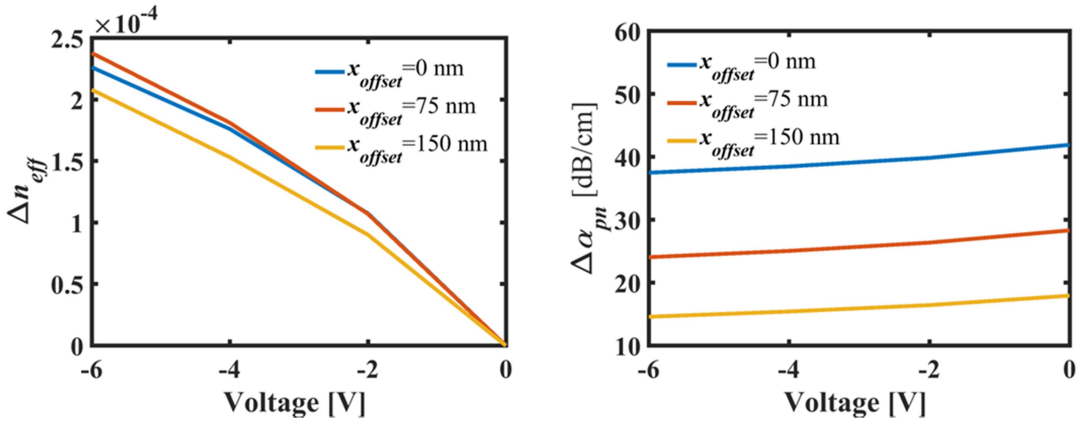

Figure 2.8 Simulated Δn_{eff} and $\Delta \alpha_{pn}$ under reverse bias voltage from 0 V to -6 V.

2.2.3 High-speed characteristics of a revered biased p-n junction

The bandwidth limitation of the p-n junction can be studied using the small-signal circuit, or a lumped model [21] as shown in Figure 2.9, provided that the total length of the junction is relatively short (shorter than one tenth of the effective microwave wavelength). This is usually the case for the Si-MRR modulator since the majority of designs for high-speed operations have a radius smaller than 30 μm limiting the total length of the junction shorter than 200 μm whereas the effective microwave wavelength in vacuum for a 10 Gb/s signal as an example is 30 mm. Since the p-n junction operates in the depletion mode, depleted and quasi-neutral regions can be treated as serially connected capacitors (C_d) and resistors (R_n and R_p) respectively which results in a low-pass filtering with an upper bandwidth limit. In addition, the parasitic resistance (R_b) and capacitances (C_m and C_b) that result from the co-planar metal contacts and the buried oxide layer (BOX) can further reduce the device bandwidth. R_s is the impedance that is seen at the source and typically is equal to 50 Ohms for the purpose of impedance matching. Accurate impedance values in small-signal circuits can be extracted through fitting the S_{11} response measured by a vector network analyzer [22]. In the model

presented here, I assume that the influences from the parasitic elements (R_b, C_m and C_b) are negligible so that the small-signal model shown in Figure 2.9 is simplified into a first-order *RC* circuit with four elements in series: R_s, R_n, R_p and C_d. The voltage across the capacitive element can be taken as [23]:

$$\frac{1}{1+j2\pi fC_d\left(R_n+R_p+R_s\right)} \tag{2.24}$$

The 3-dB bandwidth is defined as the frequency at which this voltage drops by half and is given by:

$$f_{pn}=\frac{1}{2\pi C_d\left(R_n+R_p+R_s\right)} \tag{2.25}$$

The term *RC* is also referred to as the time constant and has units of seconds. Under the full-depletion approximation, the depletion capacitance C_d can be deduced from the infinite parallel-plate capacitor formula:

$$C_d=\varepsilon_0\varepsilon_s\frac{t_{channel}L_{pn}}{W_d} \tag{2.26}$$

where W_d is defined by Eq. (2.13), L_{pn} is the total junction length and $t_{channel}$ is the channel thickness. More advanced analytical modeling of the p-n junction capacitance can be found in [24], which incorporates fringing-field effects that increases the total capacitance by 25% for the typical SOI rib waveguide designs.

The analytical expression for the resistance of a doped waveguide is given by:

$$R=\frac{W}{\mu qtL} \tag{2.27}$$

where μ is the carrier mobility, t is the thickness of the waveguide, L is the total length in the propagation direction and W is the width of the doped regions in the lateral direction. The series resistance for the junction with the geometry given by Figure 2.7 can be expressed as:

$$R = \frac{-w/2 - x_{p++}}{q\mu_p t_{slab} L} + \frac{x_p + w/2}{q\mu_p t_{channel} L} + \frac{w/2 - x_n}{q\mu_n t_{channel} L} + \frac{x_{n++} - w/2}{q\mu_n t_{slab} L} \tag{2.28}$$

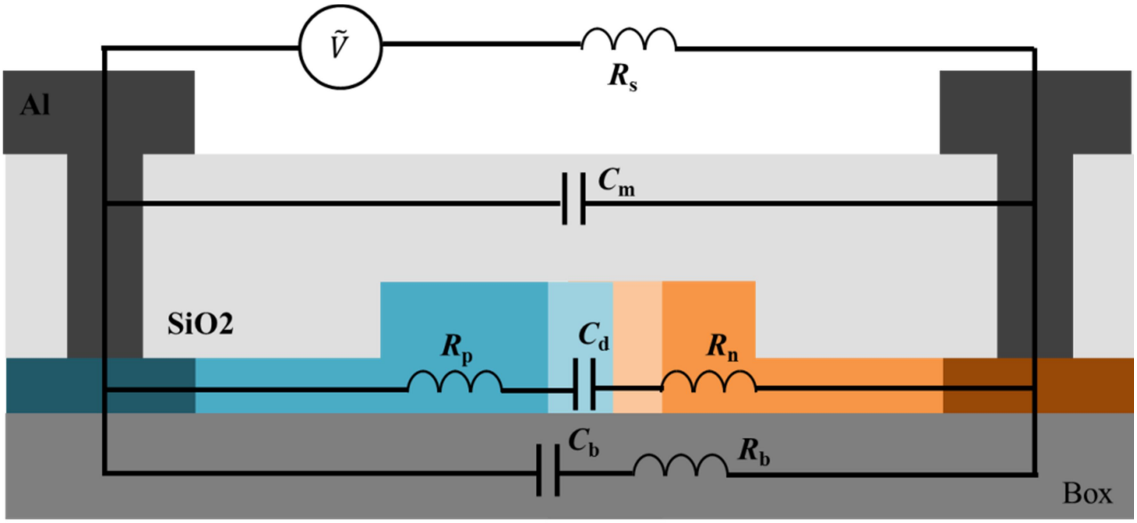

Figure 2.9 Small-signal circuits for the depletion p-n junction.

2.3 Silicon micro-ring resonator modulator

2.3.1 Static transfer for a silicon micro-ring resonator (Si-MRR)

Silicon micro-ring resonators (Si-MRR) are known as a special kind of Fabry-Pérot (F-P) etalon with the cavity formed by a closed-loop ring [25]. A bus waveguide closely placed beside the ring forms a 2 × 2 coupler that allows light to couple into or out of the ring cavity. The resonant condition is achieved when a roundtrip phase change of

the light propagating in the ring is equal to an integer number of 2π. Thus, a standing wave is formed (trapping the optical energy in the ring) and a large field can be built up owing to constructive interference. Meanwhile, destructive interference is obtained at the output so that at resonance the transmitted power is minimized. Due to its notch-filtering characteristic, the Si-MRR is widely used for filtering and routing in an integrated system.

Figure 2.10 shows two basic configurations for the Si-MRR, namely the all-pass configuration and the add-drop configuration. In the add-drop configuration, a second bus waveguide is placed at the drop port of the Si-MRR so that a portion of light, instead of being trapped in the ring, can be extracted and routed into the drop-port waveguide.

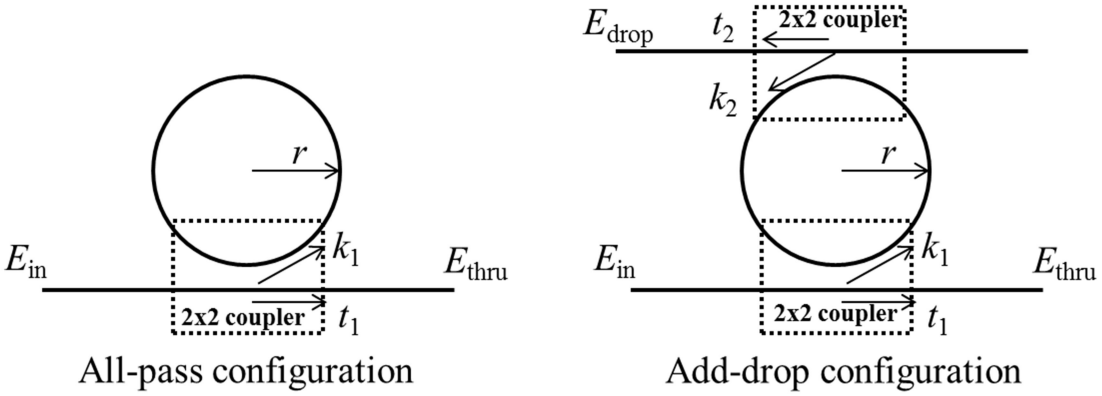

Figure 2.10 All-pass and add-drop configuration.

The 2 × 2 coupler is described by the thru-coupling coefficient t and cross-coupling coefficient k and a lossless coupler is assumed so that $t^2 + k^2 = 1$ (t and k are real numbers). For the all-pass Si-MRR, the field static transfer for the though port is [26]:

$$E_{thru} = \frac{-a + te^{-i\theta}}{-at + e^{-i\theta}} \tag{2.29}$$

where a is the roundtrip propagation coefficient (a=1 means a lossless ring) and θ is the roundtrip phase change defined as:

$$\theta = n_{eff} \frac{4\pi^2}{\lambda} r \tag{2.30}$$

The input field E_{in} is normalized to 1. For the add-drop Si-MRR, the field static transfer for the through port is:

$$E_{thru} = \frac{t_1 - t_2 a e^{i\theta}}{1 - t_1 t_2 a e^{i\theta}} \tag{2.31}$$

and the field static transfer for the drop port is:

$$E_{drop} = \frac{-k_1 k_2 \sqrt{a} e^{i\theta/2}}{1 - t_1 t_2 a e^{i\theta}} \tag{2.32}$$

Note that the all-pass Si-MRR can be considered as a special kind of add-drop Si-MRR in which t_2 is equal to 1.

Simulation of an add-drop Si-MRR with a 12 μm radius and coefficients of $t_1 = 0.93$, $t_2 = 0.96$ and $a = 0.97$ is shown in Figure 2.11 and plotted as the normalized spectrum (intensity transfer) for the thru-port and drop-port signal for a wavelength range from 1540 nm to 1550 nm. A Si-MRR constructed in the silicon ridge waveguide geometry given in Figure 2.5 allows dispersion to be included by inserting the wavelength-depended n_{eff} according to the EIM calculation.

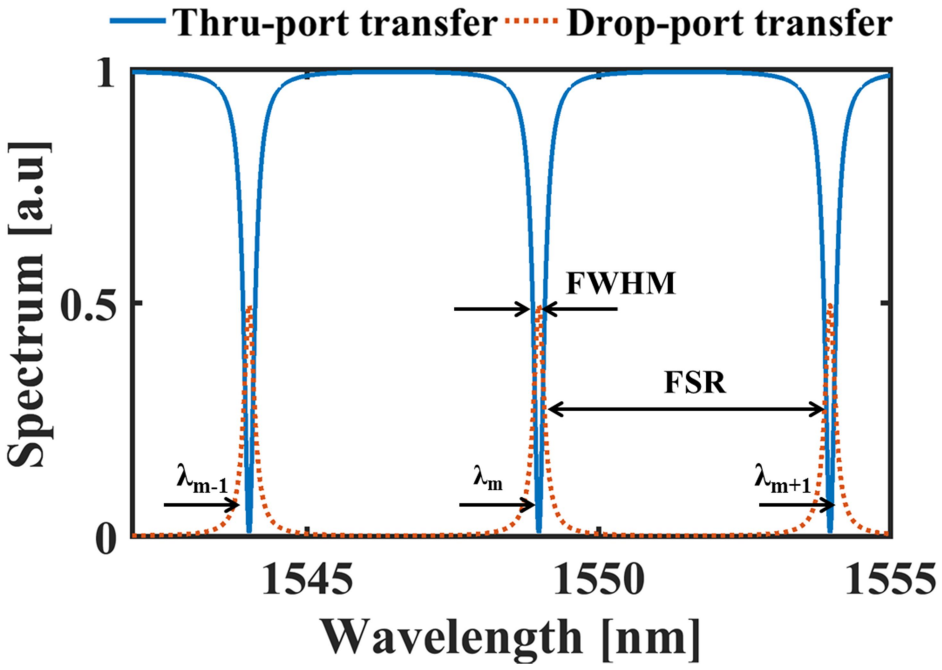

Figure 2.11 Thru-port and drop-port intensity responses for an add-drop Si-MRR.

The periodic modes shown in the spectrum are the result of forming F-P modes in the ring where the periodicity is quantified by the *free spectral range* (FSR), defined as the spacing between two consecutive modes (e.g. between λ_m and λ_{m+1}) and given by:

$$\mathrm{FSR} = \frac{\lambda_m^{\,2}}{n_g L} \tag{2.33}$$

where L is the cavity circumference and λ_m is the resonant wavelength for the m^{th} mode. The group index n_g is used in Eq. (2.33) to account for dispersion. One parameter of particular interest is the *extinction ratio* (ER) defined as the ratio of the maximum power to the minimum power for the through-port transfer. A large ER is normally desirable in the majority of applications of the Si-MRR because of the associated selectivity and accordingly a larger resonant enhancement. Figure 2.12 shows the ER (in log scale) with respect to at_2 for the λ_m mode when a in Eq. (2.31) is swept between 0.9 and 0.99, t_1

and t_2 remain same as those used for generating Figure 2.11. Three operating conditions are shown: (1) the critically-coupled condition is achieved when:

$$t_1 = at_2 \tag{2.34}$$

where the external loss due to the through-port waveguide (t_1)is equal to the total internal loss in the cavity (at_2). When the Si-MRR is critically coupled, the transmitted power at the through port is zero and the extinction ratio is infinite (Figure 2.12 shows a finite ER due to digitization in the simulation). (2) The Si-MRR is said to be over-coupled when $t_1 < at_2$ and (3) under-coupled when $t_1 > at_2$. The larger the difference between t_1 and at_2, the smaller the extinction ratio. Thus, the design optimization of the Si-MRR normally leads to matching these two terms. In addition, the coupling condition has a great impact on the phase response of the Si-MRR that will be elaborated upon in the next section.

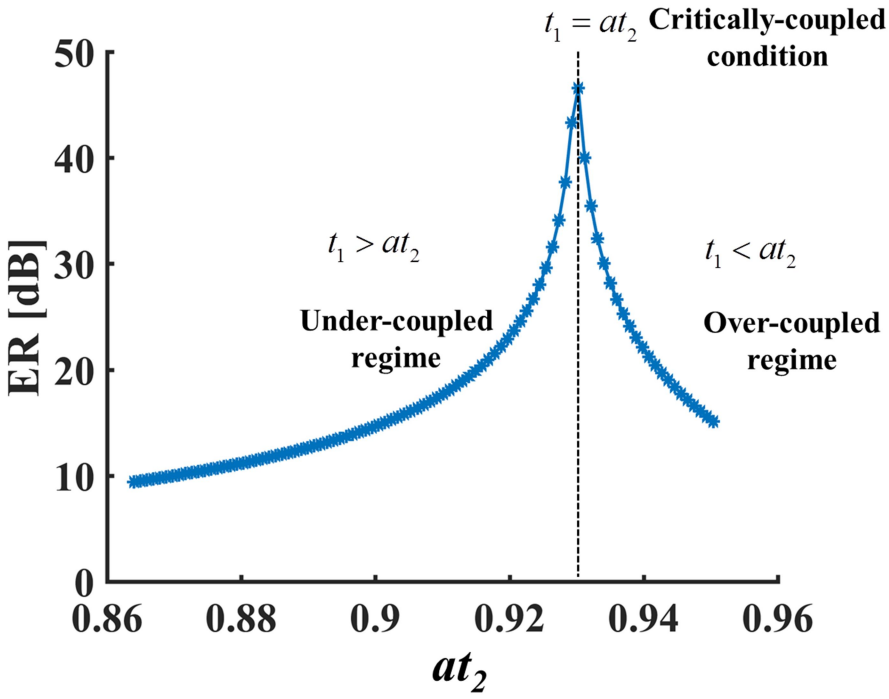

Figure 2.12 Calculated ER for an add-drop Si-MRR when a varies from 0.9 to 0.99.

The *full width at half maximum* (FWHM) or 3-dB bandwidth given by [27]:

$$\text{FWHM} = \frac{\left(1 - t_1 t_2 a\right)\lambda_m^2}{\pi n_g L \sqrt{t_1 t_2 a}} \tag{2.35}$$

The finesse of the resonator is defined as the ratio of FSR to FWHM, a measure of the sharpness of the resonance with respect to the free spectral range. By using equations (2.33) and (2.35), the finesse F for the add-drop Si-MRR is given as:

$$F = \frac{\pi\sqrt{t_1 t_2 a}}{1 - t_1 t_2 a} \tag{2.36}$$

which is fully determined by the parameters t_1, t_2, a and independent of the cavity length. The quality factor (Q-factor) of the Si-MRR is defined as the ratio of λ_m to FWHM, a measure of the sharpness of the resonance with respect to the resonant wavelength. Using equations (2.33) - (2.36), the Q factor can be determined as:

$$\text{Q-factor} = \frac{n_g L}{\lambda_m} F \tag{2.37}$$

The Q factor is commonly used to describe the transient behavior of an electrical oscillator or optical resonator. The physical manifestation of the Q factor can be associated with the ratio of energy stored in the resonator to the energy dissipated per cycle. The energy dissipation is constructed from the loss in the ring or the loss incurred during coupling to the bus waveguide. This lead to the concept of photon cavity lifetime as a measure of how long the optical energy can be stored in the cavity and is defined by:

$$\tau_{cav} = \frac{Q\lambda_{res}}{2\pi c} \tag{2.38}$$

The optical bandwidth of the Si-MRR is thus determined by τ_{cav} through $f_{cav} = 1/2\pi\tau_{cav}$. The Q factor reflects an inherent trade-off between the resonance enhancements and the operable bandwidth. A Si-MRR with large Q factor is normally used for sensing due to the large resonance enhancement whereas the Si-MRR with low Q factor is required for high-speed modulation due to the need for relatively higher bandwidth.

2.3.2 Static model of the Si-MRR modulator

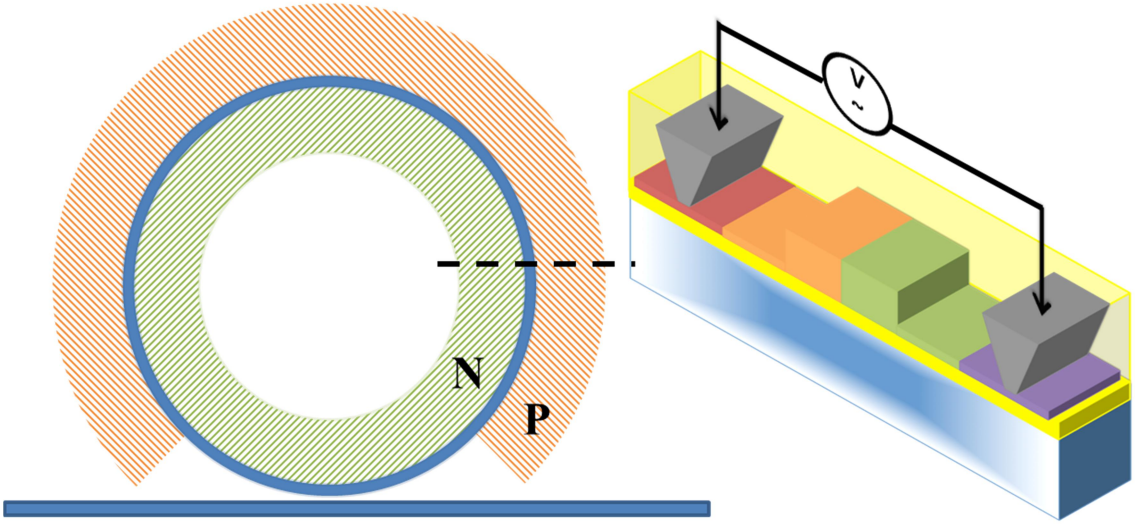

Figure 2.13 Depletion-type Si-MRR modulator

It is well known that interferometric structures such as the Si-MRR are able to translate a phase modulation in the cavity to an intensity modulation at the output. The Si-MRR modulator is realized by embedding a p-n junction as the phase shifter in the ring waveguide, as schematically drawn in Figure 2.13. The all-pass Si-MRR is preferable to the add-drop Si-MRR since the p-n junction can cover a larger portion of the ring.

When the refractive index of the waveguide is modulated via the plasma dispersion effect, the effective index n_{eff} as well as the absorption α of the optical mode

will be modulated as indicated by Eq. (2.23). As a result, some modifications have to be made for the static field transfer Eq. (2.29) , using the modulated terms θ and a defined as:

$$\theta = \frac{2\pi}{\lambda}\left(n_{eff}L + \Delta n_{eff}L_{pn}\right) \tag{2.39}$$

$$a = \sqrt{e^{\left(-\alpha_i L - \alpha_{pn}L_{pn}\right)}} \tag{2.40}$$

where L_{pn} is the physical length of the p-n junction, a_i is the intrinsic loss of the waveguide, Δn_{eff} and a_{pn} are the carrier-induced effective index change and extrinsic loss calculated by equations (2.11) and (2.12), respectively.

A simulation for DC intensity responses of a 12-μm Si-MRR modulator under different reverse biases is performed using the junction design shown in Figure 2.8. In the simulation, 88% of the ring is assumed to be covered by the p-n junction so that $L_{pn} = 0.88L$ and the remaining 12% of the ring forms the coupler. The intrinsic loss including the propagation loss as well as the bending loss is set to be 3 dB/cm. The propagation coefficient a at zero bias is determined to be 0.976 according to Eq. (2.40). Two simulation conditions t =0.972 and t =0.981 are chosen to study the difference between Si-MRRs operating under the over-coupled and the under-coupled regimes, respectively, while remaining close to 0.976 to guarantee a large notch depth. The simulated results for the intensity responses are shown in Figure 2.14, which leads to an important observation. If the Si-MRR is over-coupled at zero bias, it will move further from the critically coupled condition as reverse bias increases and the notch depth will keep reducing. On the contrary, if the ring is under-coupled at zero bias, it will approach the critically coupled condition as reverse bias increases and may or may not switch to the

over-coupled condition. Another major difference between the two regimes (over- or under-coupled), as mentioned previously, is related to the phase response of the Si-MRR, obtained from the argument of Eq. (2.29). The simulated phase responses for the two regimes are shown in Figure 2.15. For the over-coupled condition, the phase response has a continuous 2π change across the resonance whereas for the under-coupled condition, the phase response has an abrupt change at the resonance point, while the total phase change will be less than π. The phase response of the over-coupled MMR modulator allows it to be exploited in more advanced applications such as negative-chirp modulation, coherent modulation. This will be further investigated in later chapters of this thesis.

The DC modulation efficiency of the Si-MRR modulator is defined as the resonance shift relative to the driving voltage change. Based on the intensity responses of the over-coupled Si-MRR modulator shown in Figure 2.15 , the modulation efficiency is plotted in Figure 2.16.

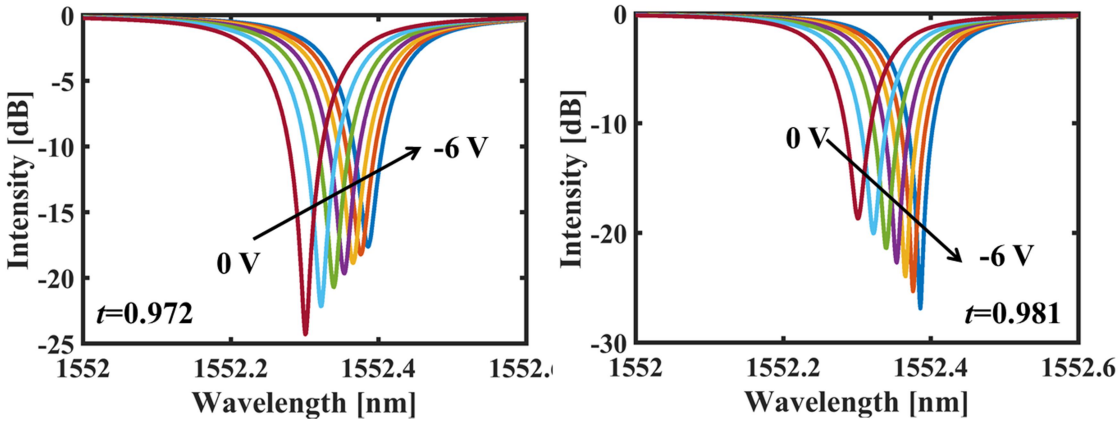

Figure 2.14 Simulated intensity responses under reverse bias voltage from 0 V to -6 V for the Si-MRR modulators operating under the over-coupled condition (t=0.972) and under-coupled condition (t=0.981)

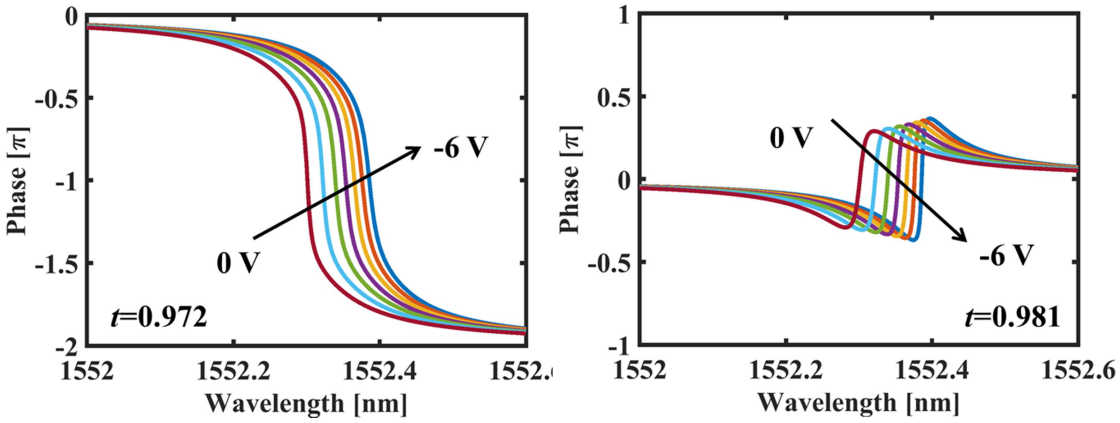

Figure 2.15 Simulated phase responses under reverse bias voltage from 0 V to -6 V for the Si-MRR modulators operating under the over-coupled condition (t =0.972) and under-coupled condition (t =0.981)

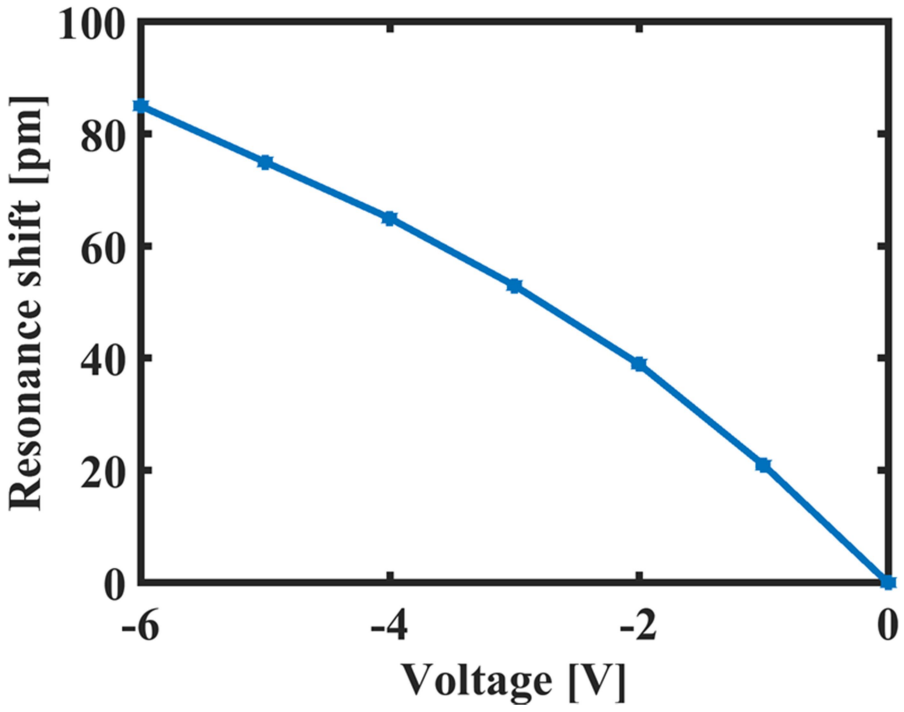

Figure 2.16 Resonance shift relative to the resonance wavelength at zero bias.

The coupling gap between the Si-MRR and the bus waveguide determines the coupling of light from the bus to the ring. The determination of the coupling coefficient is

critical to the design of the Si-MRR modulator. Although there are several analytical treatments to calculate the coupling coefficient [28], each one has a certain approximation for a specific problem. Thus, to provide a satisfactory result, FDTD simulation is included in our model with the aim to establish a look-up table where the gap distance can be directly determined or extracted by interpolation. An example is given in Figure 2.17 to show the obtained t through 3-D FDTD simulation with respect to discrete gap distances for three different slab thicknesses (80 nm, 90 nm and 100 nm). This is to illustrate how the fabrication uncertainty (e.g. slab thickness changes or gap changes) will affect the device performance. For t =0.976, 0.972 and 0.981, there is a corresponding gap distance of 295 nm, 275 nm, 315 nm. If the 295nm is assumed to be the optimum gap for the critically coupled condition, a small variation (e.g ± 20nm) can result in a change of the coupling condition and consequently a reduction in the notch depth. Similarly, other design parameters such as those for the p-n junction and the silicon ridge waveguide can also vary to the extent that the fabricated device deviates in performance from nominal simulations. To counteract the fabrication uncertainty, the current approach is to offset the design parameters of the device around an optimal combination by assigning them to a 2-D matrix (for example, junction offset versus gap). Therefore, devices with the expected optimum performance can be obtained from a wafer even in the presence of the fabrication uncertainty. These types of deliberate device design variation to account for inevitable fabrication variation will remain an important part of commercialization of silicon photonics (at least until fabrication variance can be substantially reduced). The maximization of device yield under such conditions is a complex problem often approached using Monte-Carlo simulation. It is not discussed further in this thesis.

The total bandwidth f_{3dB} of the Si-MRR modulator can be estimated using the relation:

$$\frac{1}{f_{3dB}^2} = \frac{1}{f_{pn}^2} + \frac{1}{f_{cav}^2} \tag{2.41}$$

by using the RC limited bandwidth f_{pn} and the cavity-limited bandwidth f_{cav} defined by equations (2.25) and (2.38). Recent studies have shown that Eq. (2.41) is not able to accurately reflect the bandwidth due to the so-called optical peaking effect [29], which results from the asymmetrical small-signal response at different detunings between the laser wavelength and Si-MRR resonance. Nevertheless, Eq. (2.41) can still provide a useful estimate (usually an underestimate) of the device bandwidth, which is tolerable in the design phase.

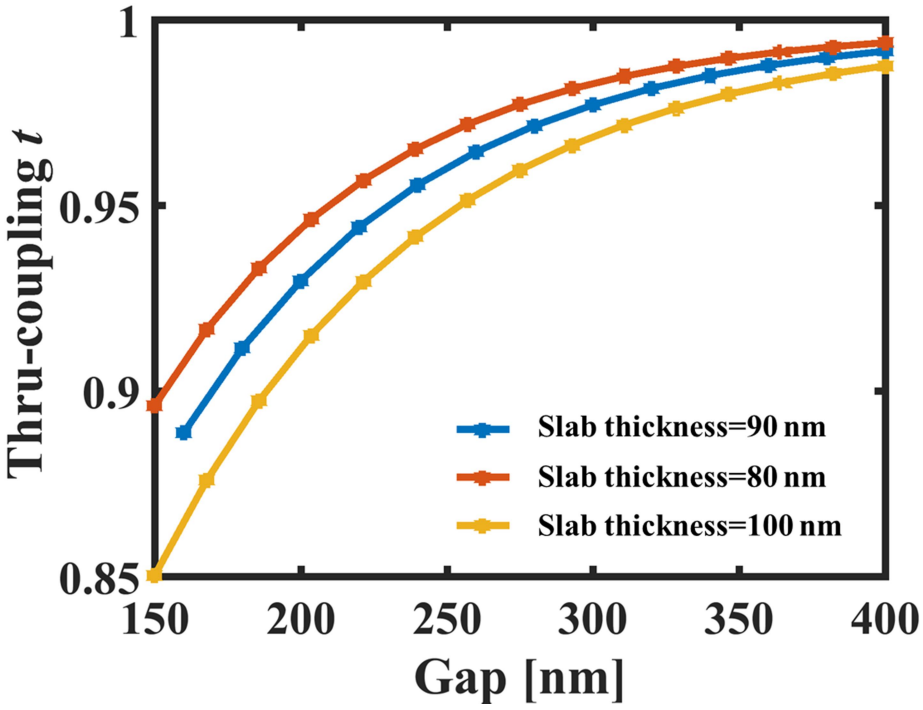

Figure 2.17 Thru-coupling coefficient *t* with respect to gap for three different slab thicknesses (80 nm, 90 nm and 100 nm)

2.3.3 Dynamic response of Si-MRR modulator

The static model introduced in section 2.3.2 can be used to extract many properties of the ring modulator such as resonance, FSR, Q-factor, notch depth etc. However, it provides no information on the dynamic response under an RF-drive signal, which in this case governs the chirp characteristics of the modulator. The dynamic model of the ring resonator is described in this thesis by the *coupling mode theory* (CMT) in time domain [30], which states that the Si-MRR can be treated as an RLC-like system with a second-order response where the perturbation of the energy is caused by the RF-driving carrier-induced modulation on the refractive index. The damping, as explained previously for the introduction of the Q factor, is enabled by the energy that is either coupled out by the external through-port bus waveguide or dissipated by the internal loss in the ring. The CMT equations for the all-pass Si-MRR are given as [31]:

$$\frac{d}{dt}\left(\psi(t)e^{-j\omega t}\right)=\left(-j\omega_r(t)-\frac{1}{\tau_i(t)}-\frac{1}{\tau_e}\right)\left(\psi(t)e^{-j\omega t}\right)+j\sqrt{\frac{2}{\tau_e}}\left(E_i(t)e^{-j\omega t}\right) \tag{2.42}$$

$$E_t(t)e^{-j\omega t}=E_i(t)e^{-j\omega t}+j\sqrt{\frac{2}{\tau_e}}\psi(t)e^{-j\omega t} \tag{2.43}$$

where E_t and E_i are the amplitudes of optical waves at the input port and through port respectively, while ψ is the amplitude of the optical wave circulating in the ring; ω is the angular frequency of the optical carrier and ω_r is the angular resonance frequency; τ_i is the amplitude decay time constant due to the internal loss in the ring; and τ_e is the amplitude decay time constant caused by the external loss. The two decay time constants are related to the propagation coefficient a and through-coupling coefficient t through the equations:

$$\tau_i = \frac{2Ln_g}{c\left(1-a^2\right)} \tag{2.44}$$

$$\tau_i = \frac{2Ln_g}{c\left(1-t^2\right)} \tag{2.45}$$

In (2.42) and (2.43), the time-dependent parameters $\omega_r(t)$ and $\tau_i(t)$ are the two perturbing terms associated with the effective index and the absorption change of the phase shifter in the cavity. Eq. (2.42) is a first-order differential equation that can be solved by the forward Euler method or other numerical techniques. The algorithm in the forward Euler method requires iterations of equations (2.42) and (2.43) at a time step much smaller than the period of the modulated signal in order to obtain a converged output.

The CMT model can also generate the static transfer, using the derivative theorem of Fourier transform $\left(\mathcal{F}\left\{dx(t)/dt\right\} = -j\omega tX(\omega)\right)$, which provides:

$$\frac{E_t}{E_i} = \frac{-j\left(\omega-\omega_r\right)+\frac{1}{\tau_l}-\frac{1}{\tau_e}}{-j\left(\omega-\omega_r\right)+\frac{1}{\tau_l}+\frac{1}{\tau_e}} \tag{2.46}$$

Since the CMT mode only describes a specific resonance, the actual value of ω_r needs to be provided by the intensity transfer generated by the formula in the space domain such as the one shown in Figure 2.14. A useful practice prior to the time-domain simulation is to compare the static transfers obtained by equations (2.29) and (2.46), which can ensure the modulated parameters like ω_r and τ_i are accurately assigned.

2.4 System modeling

2.4.1 Overview

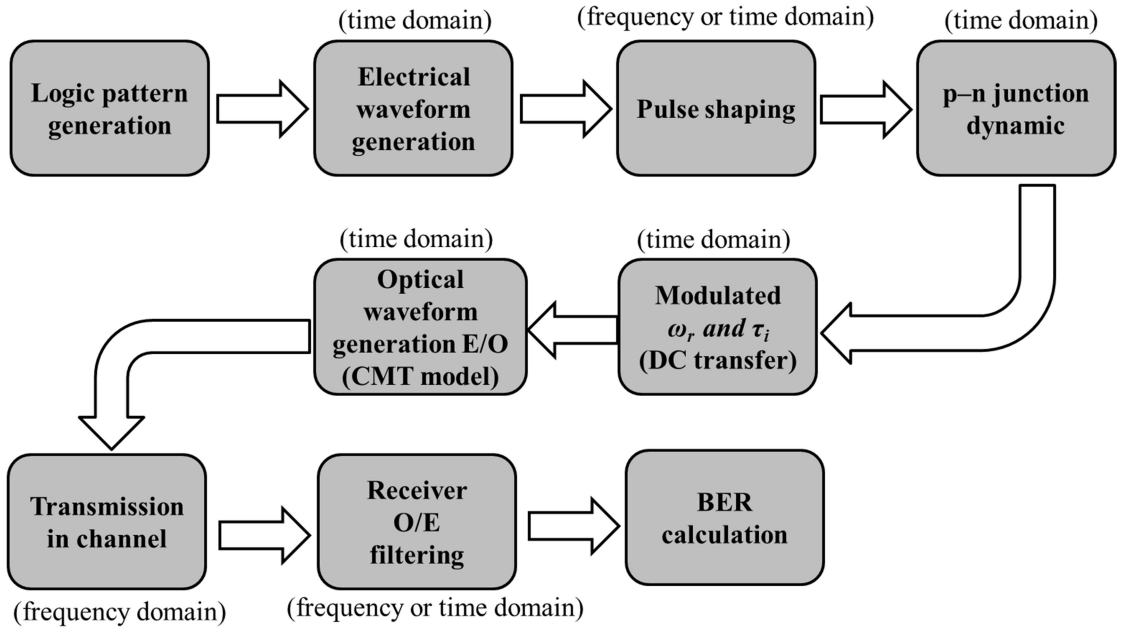

Figure 2.18 Flowchart for the system end-to-end modeling

A preliminary system-level model is built using MATLAB® with the aim to provide a fast but insightful estimation for the modulator performance in a transmission link. The simulation results can not only be used to validate the device modeling discussed in this thesis but also identify those predominant limiting factors in the performance such as modulation chirp, bandwidth and large-signal extinction ratio in order to generate feedback information for a further optimization. The flowchart of the system end-to-end simulation is given in Figure 2.18 showing the main functional blocks that are currently implemented in the model. In order to simplify the simulation, it is necessary to break down the whole simulation into several smaller blocks (where the simulation may be performed either in the time domain or in the frequency domain) so

that the specific problem can be singled out and solved. The applications of these simulations will be laid out in the following sections by using an example of calculating the chirp-induced power penalty from the intensity-modulated over-coupled Si-MRR modulators (the one shown in Figure 2.14) in a presence of different aggregated dispersions.

2.4.2 Electrical waveform generation

For electrical signal generation, a pseudo-random logic pattern consisting of '0' and '1' bits should be first created, followed by the electrical waveform generation. A raised cosine pulse is used for generating the '1' bit in order to create a more realistic device-generated electrical pulse. The raised cosine function in the time domain is expressed as

$$p(t)=\begin{cases}1, & |t|\le\dfrac{1-\beta}{2}T_b\\ \dfrac{1}{2}\left\{1+\cos\left[\dfrac{\pi}{\beta T_b}\left(t-\dfrac{1-\beta}{2}T_b\right)\right]\right\}, & \dfrac{1-\beta}{2}T_b\le|t|\le\dfrac{1+\beta}{2}T_b\\ 0, & \text{otherwise}\end{cases} \tag{2.47}$$

where T_b is the time interval for one bit and the pulse is assumed to have 100% duty cycle or in other words, non-return-to-zero (NRZ). β is the roll-off factor with a range between 0 and 1, which accounts for the roll-off speed of the pulse edge. $\beta=0$ corresponds to an ideal rectangular pulse whereas $\beta=1$ corresponds to an ideal cosine pulse that has a maximum rising/falling time of T_b. Figure 2.19 gives the simulated pulses according to Eq. (2.47) as an example for a 10 Gb/s signal with an arbitrary bit pattern for three different conditions: $\beta=0$, $\beta=0.5$ and $\beta=1$.

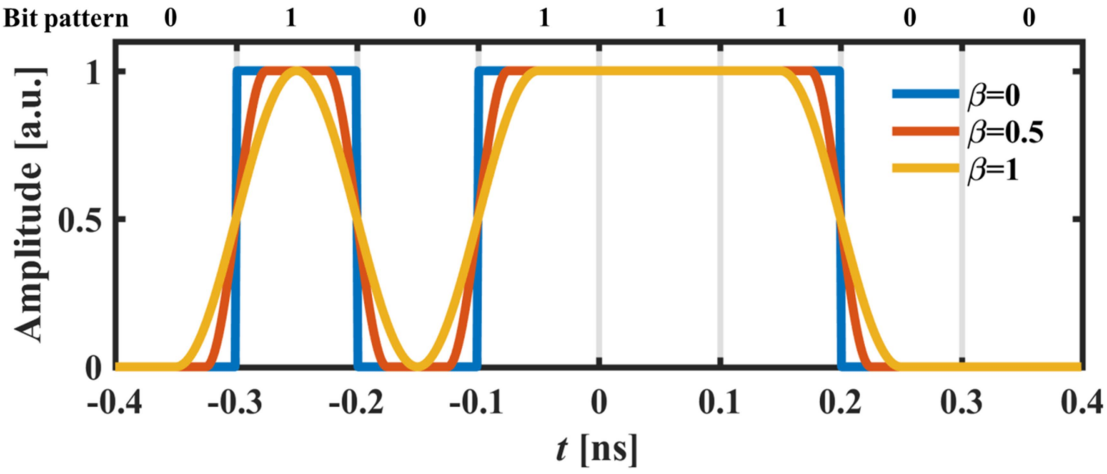

Figure 2.19 Simulated raised cosine pulse for a 10 Gb/s signal

Pulse shaping [32] has become increasingly important in digital communication owing to its capability to deal with the bandwidth limitation of the transmitter and the channel distortion, especially for high modulation rates. Nyquist filtering is frequently used to achieve a band-limited signal so that the inter-symbol interference can be minimized. The raised cosine filter is a type of Nyquist filter incorporated in the model, though their theoretical description is not discussed in this thesis and only the mathematical forms are given. To begin with, the frequency response of the raised cosine filter which has the similar expression as Eq. (2.47) is given as

$$H_{RC}(f)=\begin{cases}1, & |f|\le\dfrac{1-\beta}{2T_b}\\[2ex] \dfrac{1}{2}\left\{1+\cos\left[\dfrac{\pi T_b}{\beta}\left(f-\dfrac{1-\beta}{2T_b}\right)\right]\right\}, & \dfrac{1-\beta}{2T_b}\le|f|\le\dfrac{1+\beta}{2T_b}\\[2ex] 0, & \text{otherwise}\end{cases} \tag{2.48}$$

where it can be seen that the bandwidth of the baseband signal is determined to be $(1+\beta)/2T_b$. The time-domain impulse response of Eq. (2.48) is given as

$$h_{RC}(t)=\frac{\cos\left(\pi\beta\frac{t}{T_b}\right)}{1-\left(2\beta\frac{t}{T_b}\right)^2}\times\frac{\sin\left(\pi\frac{t}{T_b}\right)}{\pi\frac{t}{T_b}} \tag{2.49}$$

where L'Hospital's rule needs to be applied to solve the equations for three points $h(0)=1$ and $h(\pm T_b/2\beta)=\beta/2\sin(\pi/2\beta)$. To apply the filtering in the simulation, a convolution is performed between the electrical signal and the filter impulse response in the time domain to obtain a filtered signal output. Figure 2.20 gives an example of simulated impulse responses based on Eq. (2.49) with $T_b=0.1$ ns for three conditions: $\beta=0,\ 0.5$ and 1 along with their Fourier transforms which give the frequency responses. Note that the impulse response given by Eq. (2.49) is divided by its integration over the total time span so that the calculated frequency response will be normalized to 1 at DC operation. Other filters such as root raised cosine filter, Gaussian filter, Bessel filter, etc. are also frequently used for a variety of applications such as pulse shaping, noise rejection etc. In principle, they are treated in the same way as the raised cosine filter described here. The use of them depends on the focus of the work. For the sake of simplicity, these filters will not be further discussed in the thesis.

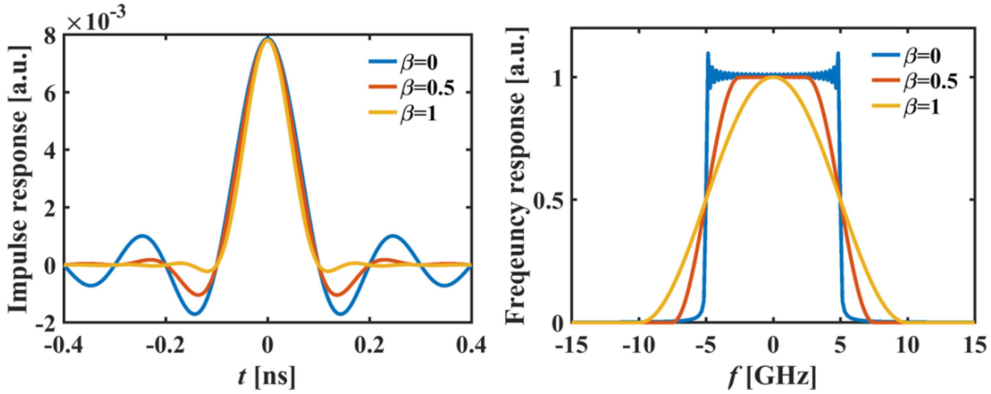

Figure 2.20 Simulated impulse responses (left) and the frequency responses (right) of the raised cosine filter for three roll-off factors. T_b is 0.1 ns and the time span is $8T_b$

2.4.3 Optical waveform generation in the CMT model

With a known electrical waveform of the source signal, the effective voltage drop on the depletion region can be determined based on the dynamic of the serial *RC* circuit as shown in section 2.2.3. The effective voltage V_{pn} on the capacitor and the source voltage V_s are related by the following expression:

$$\frac{dV_{pn}(t)}{dt} + \frac{1}{RC}V_{pn}(t) = V_s(t) \tag{2.50}$$

which is also a first-order differential equation that can be numerically solved by the forward Euler method. Using equations (2.26) and (2.28), the capacitance *C* at zero bias and the total resistance *R* including the 50 ohms source resistance are calculated to be 28 fF and 104.6 Ω, resulting in the *RC* constant of 3 ps and the corresponding electrical 3-dB bandwidth of 54 GHz. Although the *RC* constant should be a dynamic term due to the modulation on the depletion width, the variation is so fractional that it is neglected in the simulation. Next steps are to determine the modulated terms $\omega_r(t)$ and $\tau_i(t)$ appearing in the CMT equations, using the analytical method described for the DC simulation. Figure 2.21 gives an example of the simulated $V_{pn}(t)$, $\omega_r(t)$ and $\tau_i(t)$ generated by the electrical waveform in Figure 2.19 with a peak-to-peak voltage equal to 2 V and β=0.5.

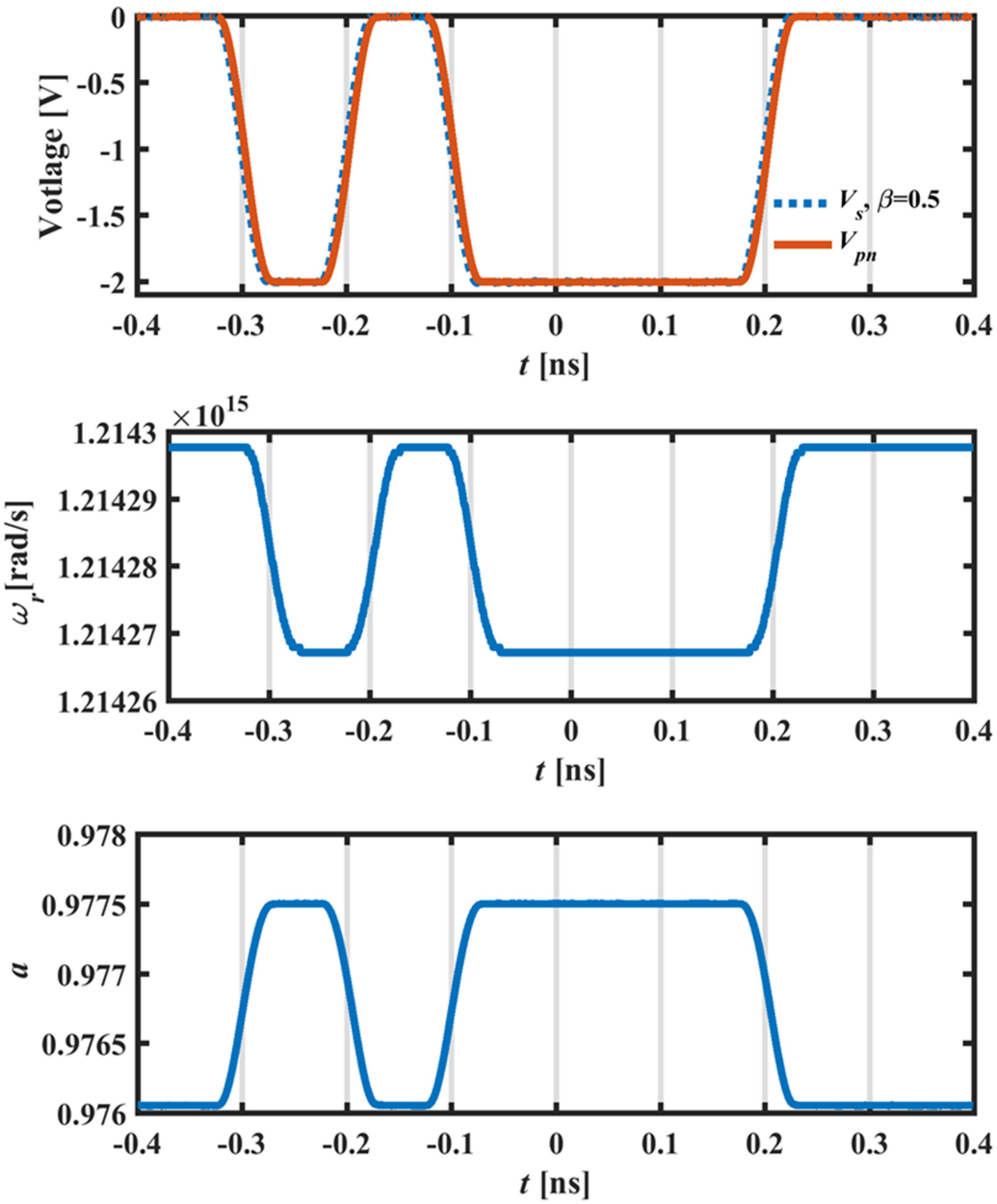

Figure 2.21 Simulated V_{pn} , ω_r and a .

The optical carrier frequency ω in the CMT equations determines which side of the intensity transfer is used for modulation. The blue-side modulation is obtained when the detuning relative to ω_r at 0 V is positive (towards the shorter wavelength) whereas the red-side modulation is achieved when the detuning relative to ω_r at the maximum reverse

bias (-2 V in this case) is negative (towards the longer wavelength). Setting ω between the resonances at 0 V and -2 V will cause a secondary peak at zero level of the modulation and thus it should be avoided. The simulated optical waveforms at two wavelengths of 1552.29 nm and 1552.35 nm (corresponding to a 10 pm detune towards the blue side and the red side, respectively) are compared to show the difference between the blue-side and the red-side modulations. By inserting $\omega_r(t), \tau_i(t)$, ω and t (0.972 for the over-coupled Si-MRR as given by Figure 2.14) into CMT equations (2.42) and (2.43), the simulated results for 128 iterations per 1-bit interval are shown in Figure 2.22, including both the intensity waveform $\left|E_t(t)\right|^2$ and the chirp waveform $\Delta f(t)$. The modulation chirp is referred to as the frequency deviation from the central carrier frequency and mathematically defined as [33]:

$$\Delta f = -2\pi \frac{d\phi}{dt} \tag{2.51}$$

where ϕ is the phase change of the signal obtained by the argument of the complex amplitude. It can be seen that a major difference is the opposite sign for the chirp appearing at the signal rising/falling edge. This unique chirp characteristic that can be only found in the over-coupled Si-MRR leads to a phenomenon, so-called negative-chirp modulation, where a negative frequency change occurs at the signal rising edge whereas a positive frequency change occurs at the signal falling edge [34]. The negative-chirp modulation is more desirable in an intensity-modulated system because it naturally counteracts the positive dispersion possessed by the single-mode fiber for the C-band communication window. This feature will be discussed more in the following chapter that experimentally demonstrates a negative-chirp modulation using an over-coupled Si-MRR modulator.

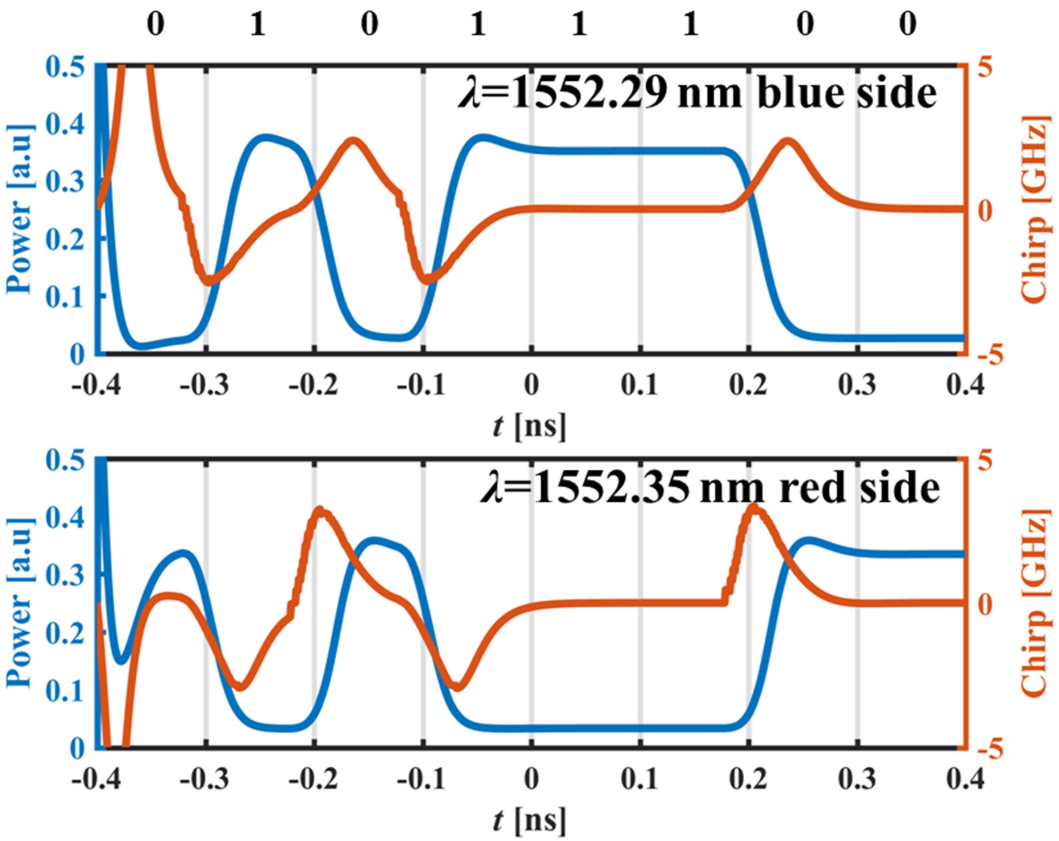

Figure 2.22 Simulated optical waveforms (intensity and chirp) for two wavelengths: 1552.29 nm (blue-side modulation) and 1552.35 nm (red-side modulation).

2.4.4 Performance analysis

The evolution of the slow varying envelope of the modulated signal propagating in fiber is governed by the nonlinear Schrödinger equation in which the fiber dispersion and nonlinearity are mutually interactive. The nonlinear Schrödinger equation is commonly solved in the frequency domain, using the *split-step Fourier method* (SSFM) [35]. In SSFM, the total propagation distance z is divided into many small steps Δz, leading to de-coupled fiber dispersion and nonlinearity that are then treated separately in the frequency domain. Since SSFM is a well-established theory, the detail will not be discussed further in this thesis. To study the chirp-induced power penalty, it is a common

practice to assume that the propagation loss in the fiber is zero since the modulation chirp solely interacts with the dispersion. It is similar to the experimental condition of using a lossless dispersion emulator only to emulate a total dispersion from the fiber link without introducing loss [36]. As a result, the need for the optical amplifier in the modeling is negated. In addition, the nonlinearity of the fiber can be also ignored in the simulation if the power launched is assumed small, which is also true for the real-word application.

At the receiver end, the optical signal is down-converted by a PIN photodiode with a responsivity of 1 A/W. It is necessary to have a low-pass filter to limit the excessive signal noise. There are two dominant types of receiver noise, namely the shot noise and thermal noise, both accounted for in the simulation. The mean current fluctuation (or the variance) caused by the shot noise is defined as:

$$\sigma_{\text{shot}}^2 = 2qI\Delta f \tag{2.52}$$

where I is the mean current of the signal and Δf is the bandwidth of the filter. Thus, the shot noise is significantly larger for the '1' level than for the '0' level. The thermal noise variance is defined as:

$$\sigma_{\text{thermal}}^2 = \frac{4k_B T\Delta f}{R_L} \tag{2.53}$$

where R_L is the load resistance , T is the temperature and k_B is the Boltzmann constant. The received signal quality is analyzed by the signal Q-factor defined as:

$$Q = \frac{I_1 - I_o}{\sigma_{1\text{total}} + \sigma_{0\text{total}}} \tag{2.54}$$

where I_1 and I_0 are the mean currents of the modulation '1' level and '0' level, respectively; and σ_{total} is the standard deviation for the modulation level which is defined as

$$\sigma_{\text{total}} = \sqrt{\sigma_{\text{signal}}^2 + \sigma_{\text{thermal}}^2 + \sigma_{\text{total}}^2} \tag{2.55}$$

The analytical bit error ratio (BER) is linked to the signal Q factor via:

$$\text{BER} = 0.5 erfc(Q/\sqrt{2}) \tag{2.56}$$

To extract the chirp-induced power penalty, a group of BER curves is obtained for a fiber span from 0 km to 120 km with a step of 10 km. The dispersion in the C-band window in a single-mode fiber is 15 ps/nm·km giving a total emulated dispersion up to 1800 ps/nm, while the propagation loss and nonlinearity in the fiber are disabled in the simulation. The bit sequence length of the 10 Gb/s signal is increased to 2048 with 128 samples per bit and two training bits attached ahead in order to allow enough time for the CMT simulation to stabilize (notice that in Figure 2.22, the CMT simulation appear to be unsteady at the beginning of pulse train). Pulse shaping at the transmitter is disabled and instead, a 4^{th}-order Bessel filter is added at the receiver with a bandwidth of 6 GHz (1.25 times the Nyquist frequency). The threshold of the decision level is set to be the average current of the received signal. An auto-search algorithm is also implemented to search for the optimum delay time for the sampling that provides the maximum signal Q-factor. The two groups of BER cures are shown in Figure 2.23 (a) and (b) for the blue-side modulation and the red-side modulation, respectively. The chirp-induced power penalties for the two BER results, as shown in Figure 2.23(c) are extracted by normalizing the received optical power relative to the one for the back-to-back BER curve at BER of 10^{-3}. Although both back-to-back performances are almost identical, the red-side modulation

severely degrades with increasing link distance compared to the blue-modulation owing to the influence of modulation chirp. The negative chirp in the blue-side modulation counteracts the positive dispersion in the fiber, leading to a low power penalty after 120km propagation. As a result, the blue-side modulation of the over-coupled Si-MRR is preferable for the inter-data centre communication with its potential of not requiring dedicated chirp compensation.

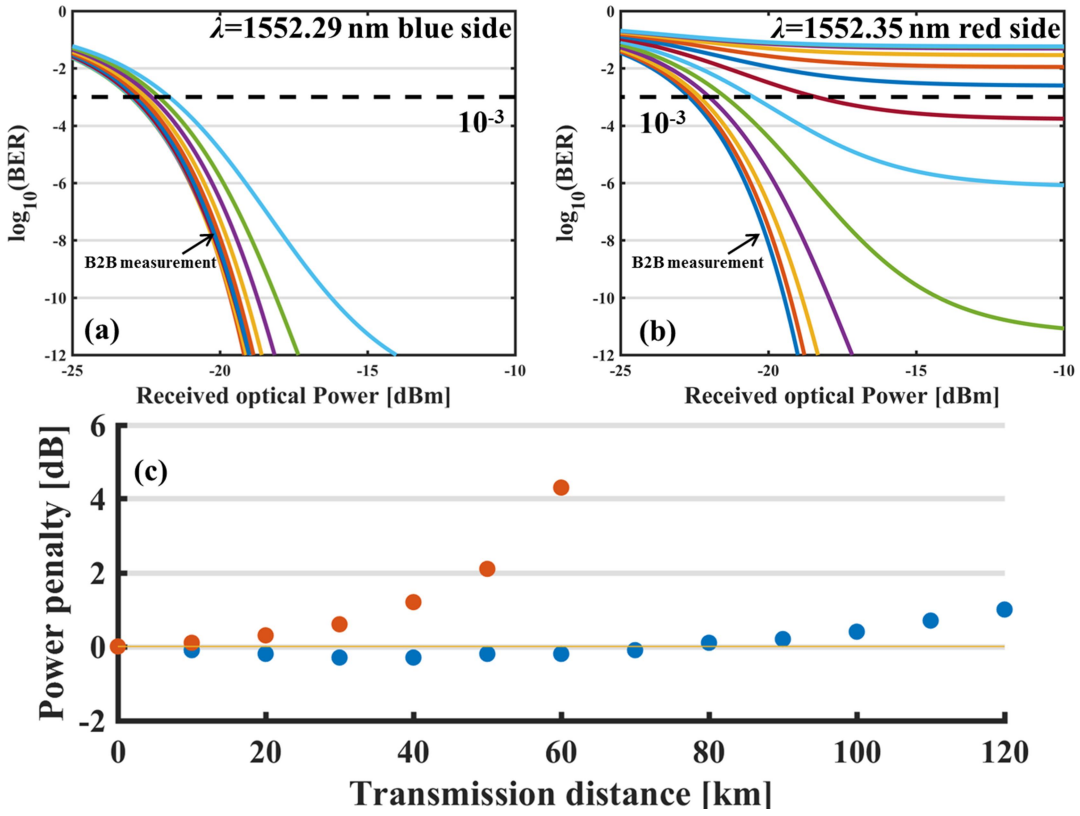

Figure 2.23 Simulated BER curves obtained for the fiber link from 0 km to 120 km at a step of 10 km: (a) for the blue-side modulation; (b) for the red-side modulation. (c) Power penalty curves calculated at BER of 10^{-3} for the two BER results.

Reference

[1] W. Bogaerts, M. Fiers, and P. Dumon, "Design challenges in silicon photonics," *IEEE J. Sel. Top. Quantum Electron.*, vol. 20, no. 4, pp. 1–8, 2014.

[2] A. Yariv and P. Yeh, *Photonics : Optical electronics in modern communications*, 6th ed. New York: Oxford University Press, 2007.

[3] G. Reed and A. Knights, *Silicon Photonics an introduction*. Chichester, West Sussex, UK ; Etobicoke, Ontario: John Wiley & Sons, c2004.

[4] E. Hecht, *Optics*, 3rd ed. Reading, Mass.: Addison-Wesley, c1998.

[5] G. B. Hocker and W. K. Burns, "Mode dispersion in diffused channel waveguides by the effective index method," *Appl. Opt.*, vol. 16, no. 1, pp. 113–118, Jan. 1977.

[6] K. S. Chiang, "Performance of the effective-index method for the analysis of dielectric waveguides," *Opt. Lett.*, vol. 16, no. 10, pp. 714–716, May 1991.

[7] B. Tatian, "Fitting refractive-index data with the Sellmeier dispersion formula," *Appl. Opt.*, vol. 23, no. 24, pp. 4477–85, 1984.

[8] R. G. Walker, "High-speed III-V semiconductor intensity modulators," *IEEE J. Quantum Electron.*, vol. 27, no. 3, pp. 654–667, 1991.

[9] B. Chmielak, M. Waldow, C. Matheisen, C. Ripperda, J. Bolten, T. Wahlbrink, M. Nagel, F. Merget, and H. Kurz, "Pockels effect based fully integrated, strained silicon electro-optic modulator," *Opt. Express*, vol. 19, no. 18, pp. 17212–19, 2011.

[10] S. Ren, Y. Rong, S. A. Claussen, R. K. Schaevitz, T. I. Kamins, J. S. Harris, and D. A. B. Miller, "Ge/SiGe quantum well waveguide modulator monolithically integrated With SOI Waveguides," *IEEE Photonics Technol. Lett.*, vol. 24, no. 6, pp. 461–463, Mar. 2012.

[11] D. A. B. Miller, D. S. Chemla, and S. Schmitt-Rink, "Electroabsorption of highly confined systems: Theory of the quantum-confined Franz-Keldysh effect in semiconductor quantum wires and dots," *Appl. Phys. Lett.*, vol. 52, no. 25, pp. 2154–2156, 1988.

[12] R. Soref and B. Bennett, "Electrooptical effects in silicon," *IEEE J. Quantum Electron.*, vol. 23, no. 1, pp. 123–129, Jan. 1987.

[13] L. Chrostowski and M. Hochberg, *Silicon photonics design*. Cambridge, UK: Cambridge University Press, 2015.

[14] G. T. Reed, G. Mashanovich, F. Y. Gardes, and D. J. Thomson, "Silicon optical modulators," *Nat. Photonics*, vol. 4, no. 8, pp. 518–526, Jul. 2010.

[15] S. Akiyama, T. Baba, M. Imai, T. Akagawa, M. Takahashi, N. Hirayama, H. Takahashi, Y. Noguchi, H. Okayama, T. Horikawa, and T. Usuki, "125-Gb/s operation with 029-V·cm V_πL using silicon Mach-Zehnder modulator based-on forward-biased pin diode," *Opt. Express*, vol. 20, no. 3, pp. 2911–23, Jan. 2012.

[16] Liao, Ling, A. Liu, R. D, B. J, C. Y, N. H, C. R, I. N, and Paniccia M, "40 Gbit/s silicon optical modulator for high-speed applications," *Electron Lett*, vol. 37, no. 24, pp. 1437–1439, 2001.

[17] A. Liu, R. Jones, L. Liao, D. Samara-Rubio, D. Rubin, O. Cohen, R. Nicolaescu, and M. Paniccia, "A high-speed silicon optical modulator based on a metal–oxide–semiconductor capacitor," *Nature*, vol. 427, no. 6975, pp. 615–618, 2004.

[18] L. Liao, D. Samara-Rubio, M. Morse, A. Liu, D. Hodge, D. Rubin, U. Keil, and T. Franck, "High speed silicon Mach-Zehnder modulator.," *Opt. Express*, vol. 13, no. 8, pp. 3129–35, Apr. 2005.

[19] R. Dube-Demers, J. St-Yves, A. Bois, Q. Zhong, M. Caverley, Y. Wang, L. Chrostowski, S. Larochelle, D. V. Plant, and W. Shi, "Analytical modeling of silicon microring and microdisk modulators with electrical and optical dynamics," *J. Light. Technol.*, vol. 33, no. 20, pp. 4240–4252, 2015.

[20] G. T. Reed, G. Z. Mashanovich, F. Y. Gardes, M. Nedeljkovic, Y. Hu, D. J. Thomson, K. Li, P. R. Wilson, S.-W. Chen, and S. S. Hsu, "Recent breakthroughs in carrier depletion based silicon optical modulators," *Nanophotonics*, vol. 3, no. 4–5, pp. 229–245, Jan. 2013.

[21] M. Shin, Y. Ban, B.-M. Yu, M.-H. Kim, J. Rhim, L. Zimmermann, and W.-Y. Choi, "A linear equivalent circuit model for depletion-type silicon microring modulators," *IEEE Trans. Electron Devices*, vol. 64, no. 3, pp. 1140–1145, Mar. 2017.

[22] H. Yu, D. Ying, M. Pantouvaki, J. Van Campenhout, Y. Hao, J. Yang, and X. Jiang, "Trade-off between optical modulation amplitude and modulation bandwidth of silicon micro-ring modulators," *Opt. Express*, vol. 22, no. 12, pp. 15178–15189, 2014.

[23] A. Agarwal and J. Lang, *Foundations of Analog and Digital Electronic Circuits*. Amsterdam ; Boston: Elsevier : Morgan Kaufman Publishers, c2005.

[24] H. Jayatilleka, W. D. Sacher, and J. K. S. Poon, "Analytical model and fringing-field parasitics of carrier-depletion silicon-on-insulator optical modulation diodes," *IEEE Photonics J.*, vol. 5, no. 1, p. 2200211, 2013.

[25] K. Vahala, *Optical Microcavities*. Singapore ; Hackensack, N.J: World Scientific, c2004.

[26] D. G. Rabus, *Integrated ring resonators the compendium*. Berlin, Heidelberg: Springer Berlin Heidelberg, 2007.

[27] W. Bogaerts, P. De Heyn, T. Van Vaerenbergh, K. De Vos, S. Kumar Selvaraja, T. Claes, P. Dumon, P. Bienstman, D. Van Thourhout, and R. Baets, "Silicon microring resonators," *Laser Photon. Rev.*, vol. 6, no. 1, pp. 47–73, Jan. 2012.

[28] W.-P. Huang, "Coupled-mode theory for optical waveguides: an overview," *J. Opt. Soc. Am. A*, vol. 11, no. 3, pp. 963–983, 1994.

[29] J. Müller, F. Merget, S. S. Azadeh, J. Hauck, S. R. García, B. Shen, and J. Witzens, "Optical peaking enhancement in high-speed ring modulators," *Sci. Rep.*, vol. 4, p. 6310, 2014.

[30] B. E. Little, S. T. Chu, H. A. Haus, J. Foresi, and J.-P. Laine, "Microring resonator channel dropping filters," *J. Light. Technol.*, vol. 15, no. 6, pp. 998–1005, Jun. 1997.

[31] L. Zhang, Y. Li, and J. Yang, "Silicon-based microring resonator modulators for intensity modulation," *Quantum Electron.*, vol. 16, no. 1, pp. 149–158, 2010.

[32] J. D. Gibson, *Principles of digital and analog communications*. New York: Macmillan, c1989.

[33] F. Koyama and K. Iga, "Frequency Chirping in External Modulators," *J. Light.*, vol. 6, no. 1, pp. 87–93, 1988.

[34] G. P. Agrawal, *Fiber-optic communication systems*, 2nd ed. New York: Wiley, c1997.

[35] Le Nguyen Binh, *Optical fiber communications systems:theory and practice with MATLAB and simulink models*. Boca Raton, FL: CRC Press/Taylor & Francis, 2010.

[36] L. Chen, P. Dong, and Y. K. Chen, "Chirp and dispersion tolerance of a single-drive push-pull silicon modulator at 28 Gb/s," *IEEE Photonics Technol. Lett.*, vol. 24, no. 11, pp. 936–938, Jun. 2012.

Chapter 3 Negative-chirp modulation using silicon micro-ring resonator modulator in a metro link

Si-MRR is considered as a key component enabling high-capacity interconnection in short-reach systems especially for some WDM applications within the data centre that demand compact footprint and low energy consumption [1–4]. Admittedly, long-haul applications where coherent communication is the preferable architecture are still, and will continue to be, dominated by the high-performance modulators built on those expensive materials such as Lithium Niobate or III-V compounds [5–7]. However, short and medium-reach applications like those for inter-data centre or metro links are more likely to adopt a low-cost, intensity-modulated and chirp-uncompensated system with consequent less stringent requirements on the modulator. In recent years, tremendous efforts have been made to improve the performance of silicon modulators in general, which leads to an increased attraction for medium-reach systems [8].

Traditionally, studies of Si-MRR modulators focus on maximizing the bandwidth and efficiency that are the critical figures of merit for shorter links, whereas the modulation chirp, an important property that limits application for longer distances, has received much less attention [9–11]. A modulated signal with chirp that has the same sign as the dispersion of the medium in which the signal propagates will aggravate pulse broadening more quickly and eventually lead to an increased inter-symbol interference [12]. The effect of different chirp signs for the intensity-modulated system performance has been discussed in section 2.4 through a simple demonstration of chirp-induced power

penalty for an over-coupled Si-MRR modulator. In a chirp-uncompensated system, it is known that zero- or small negative-chirp modulation needs to be maintained in order to invoke tolerance against the positive dispersion exhibited in the standard single-mode fiber at a 1.55 μm wavelength [13]. As a result, the Si-MRR is required to be over-coupled and modulated on the blue side of resonance where the slope of the phase response does not change chirp sign (as clearly shown in Figure 2.15). This is in contrast to an under-coupled Si-MRR whose phase response changes sign, independent of side of the resonance slope.

In this chapter, I will demonstrate an optimally designed over-coupled Si-MRR modulator on SOI with a deep notch to provide a large extinction ratio for an intensity-modulated system. The modulation chirp, especially for the blue-side modulation, is theoretically studied. The negative-chirp modulation is verified via 10 Gb/s BER measurements at a 1.55 μm wavelength for different link distances up to 100 kilometers. The results show that a zero and below zero power penalty up to 50 km link distance is achieved and the power penalty at 100 km link distance is as low as 2.5 dB. At the time of publication, this was the lowest power penalty demonstrated for a Si-MRR operating at a link distance of 100 km [14].

3.1 Device fabrication and characterization

3.1.1 Modulator design

The Si-MRR devices were fabricated at *A**Star lab, Institute of Microelectronics (IME) in Singapore. A 12 μm Si-MRR modulator with an all-pass configuration was monolithically built on a 220 nm thick SOI, using 248-nm lithography. The channel

waveguide had a width of 500 nm and a height of 220nm that guarantees single-mode operation while the slab waveguide has a thickness of 90 nm to provide an access for the heavy doping region and electrical contacts. The 2D cross-section geometry of the ridge waveguide as well as the FDTD-simulated model profile for the fundamental mode has been shown in Figure 2.4. An asymmetrical p-n junction operating in the depletion mode was embedded in the waveguide that is formed in approximately 88% of the ring whereas the remaining intrinsic segment, along with the bus waveguide, forms a 2 × 2 coupler. The nominal carrier concentrations of the n-type dopant (phosphorous) and p-type dopant (boron) are 3×10^{18} cm^{-3} and 0.5×10^{18} cm^{-3}, respectively. Two heavy doing regions with carrier concentrations of 1×10^{20} cm^{-3} were placed 800 nm away from the edge of core waveguide to avoid an excessive carrier absorption, while maintaining a tolerable device resistance.

To maximize the overlap between the depletion region in the p-doped side of the junction and the optical mode (as to increase the efficiency of the plasma dispersion effect) the junction was offset from the central position by 70 nm, which was determined to be optimal by the modeling results demonstrated in section 2.2.2. The carrier absorption in an unbiased condition was estimated to be approximately 30 dB/cm, requiring a coupling gap distance of 295 nm to achieve the critically coupled condition (3 dB/ cm intrinsic loss is assumed). The actual gap was chosen to be slightly narrower than 295nm as the design aim was to obtain an over-coupled Si-MRR with a deep notch.

A top-view microscopic image for one of the fabricated devices is shown in Figure 3.1. High-speed modulation was achieved by driving the GSG (ground-signal-ground) port (bottom three pads are the signal ports) via an RF probe. Resonance control using the thermo-optic effect was provided through an intermediate-level resistive heater

(top two pads are the signal ports) placed near the ring. The bus waveguide was 3 mm long and light was coupled into the device using a pair of surface gratings.

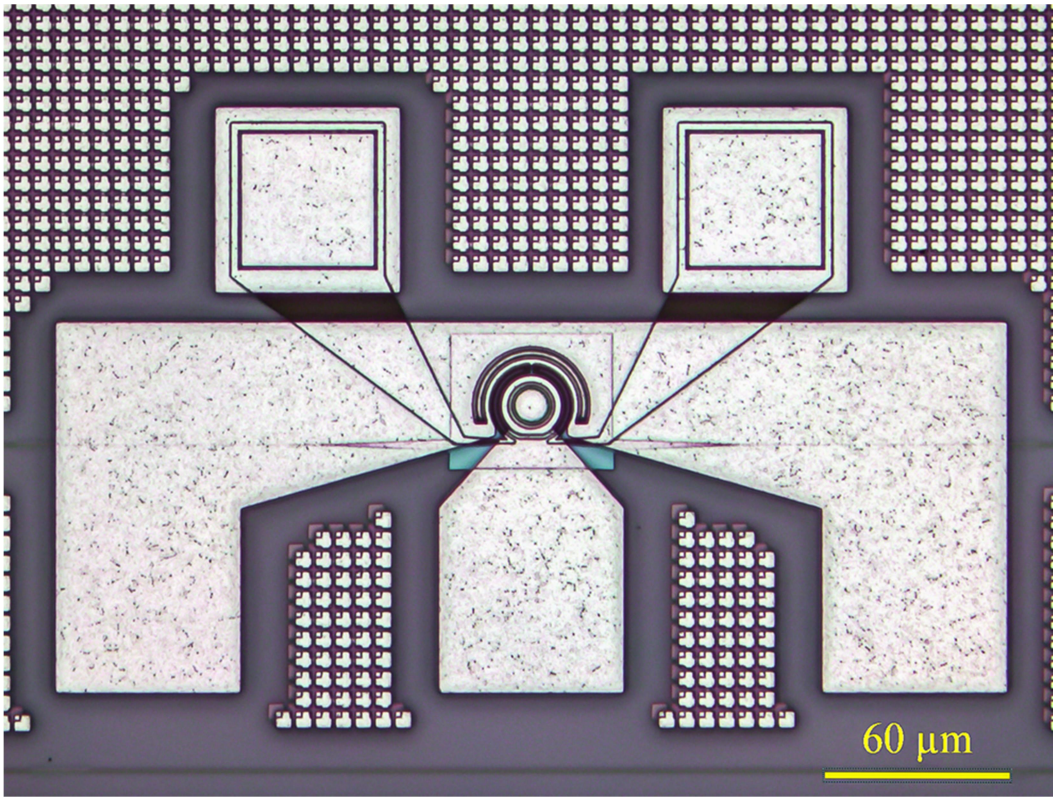

Figure 3.1 Top view microscopic image of the fabricated Si-MRR

3.1.2 Modulator characterization

The DC spectral characterization was performed using a tunable laser source with a minimum step of 2 pm and a low-noise photo-detector. The measurement setup is shown in Figure 3.2 (a) where a polarization controller aligned the input light to match the TE-mode supported by the device. A temperature controller was used to maintain the sub-mount temperature at 25 ^{o}C for thermal stability. Figure 3.2 (b) shows the measured spectra from a small forward bias of 0.5 V up to a reverse bias of -6 V. The input power was fixed at 0 dBm. Using the measured off-resonance power, the total optical loss was

thus calculated to be 17 dB, including the coupling loss at the surface gratings as well as the propagation loss in the bus waveguide. In addition, it can be easily seen that a large extinction ratio (~ 25 dB at 0 V) as well as the over-coupled condition (the notch depths reduces as the reverse bias increases) was achieved. The resonance spacing between 0 V and -6 V was determined to be 98 pm, leading to an average modulation efficiency of 16.3 pm/V if a sublinear shift is assumed for the specified bias range. The measured modulation efficiency is consistent, to a large extent, with the modelling results shown in Figure 2.16 for a similar Si-MRR design.

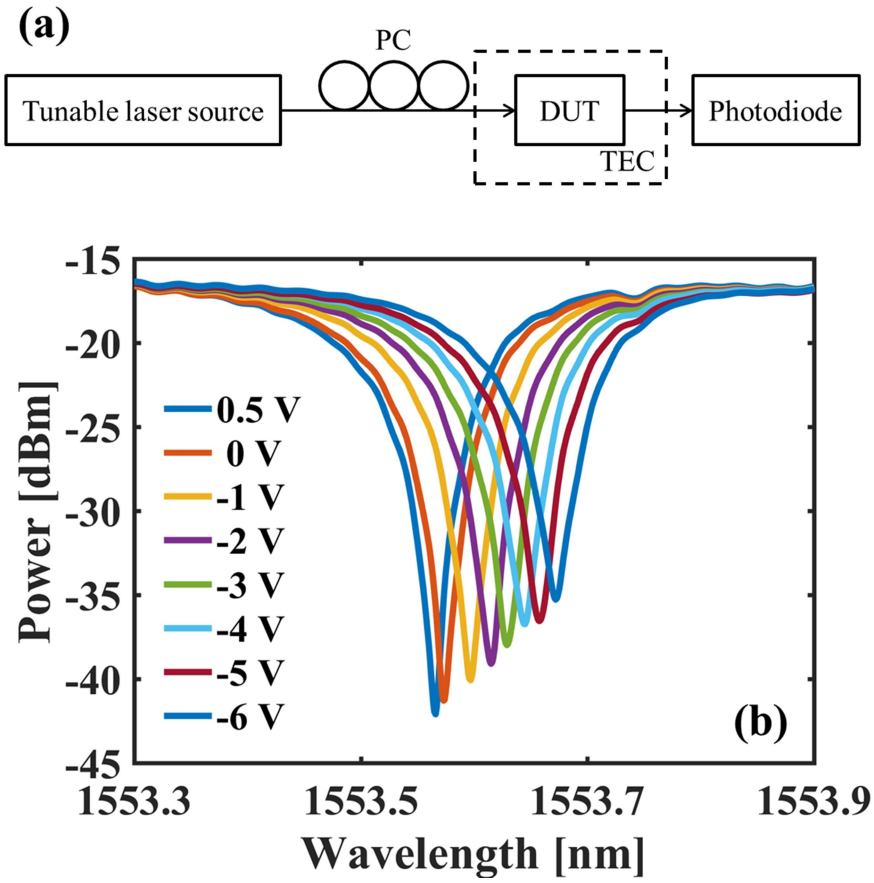

Figure 3.2 (a) Setup for DC intensity transfer measurement. PC: polarization controller. TEC: temperature control unit. DUT: device under test. (b) Measured DC spectra.

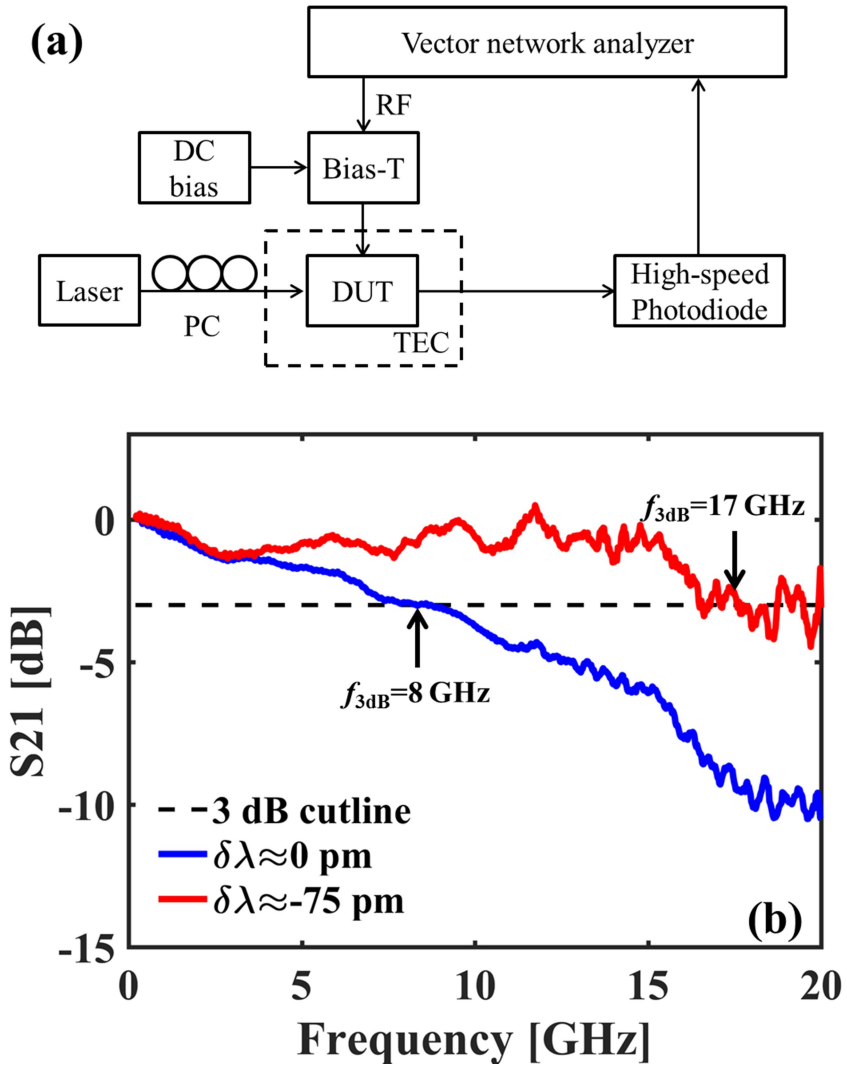

Figure 3.3 (a) Setup for S_{21} curve measurement to extract the device bandwidth. (b) Measured S_{21} curves at two detunings: $\delta\lambda = 0$ pm and $\delta\lambda = -75$ pm

The FWHM measured at – 2 V bias is 150 pm indicating a Q-factor calculated to be ~10,000, corresponding to a photon cavity-limited optical bandwidth of 19 GHz. To determine whether the total bandwidth f_{3dB} after reduction by the *RC*-limited electrical bandwidth is suitable for a 10 Gb/s BER test, a lightwave component analyzer that includes a vector network analyzer and a calibrated high-speed photodiode was used to obtain the small-signal S_{21} response, the experimental setup of which is shown by Figure

3.3 (a). A bias-T combined the RF signal and the DC bias that was set to be -2 V. As described in section 2.3.2, the laser wavelength detuning also plays a vital role in determining the effective bandwidth owing to the optical peaking effect. The S_{21} curves for two blue-side detunings namely $\delta\lambda = 0$ pm and $\delta\lambda = -75$ pm relative to the resonance at -2 V were obtained and plotted in Figure 3.3 (b) to reflect the complete bandwidth property of the device under large-signal modulation. The extracted bandwidths from the two curves are 8 GHz ($\delta\lambda = 0$ pm) and 17 GHz ($\delta\lambda = -75$ pm) which, as expected, are smaller than the optical bandwidth owing to the junction RC constant as well as other parasitic elements in the high-speed test apparatus. However, the experimentally determined bandwidth is considered sufficient for 10 Gb/s operation.

The fabricated devices were not intentionally terminated by a 50-ohm impedance, thus the device impedance under high-speed operation needs to be characterized in order to determine the effective RF signal, that is a sum of the input RF signal and the reflected signal, a direct result of impedance mismatch. Larger driving signals can generally improve the extinction ratio and reduce the insertion loss of the modulated signal but at the same time increase the modulation chirp. For a depletion-type Si-MRR modulator that has relatively low modulation efficiency, a large driving voltage is often considered beneficial for medium-reach systems due to the resulting high-quality signal. The impedance can be accurately estimated if the equivalent small-signal circuit model of the device is known. A common technique to derive the small-signal circuit is through fitting the theoretical frequency response of the reflective signal onto the measured S_{11} amplitude curve measured by the vector network analyzer [15]. However, this method is time-consuming and indirect, despite measurement precision. Instead, a simple and faithful method based on direct observations of eye diagrams has been developed to evaluate the peak-to-peak voltage (V_{pp}) of the effective signal.

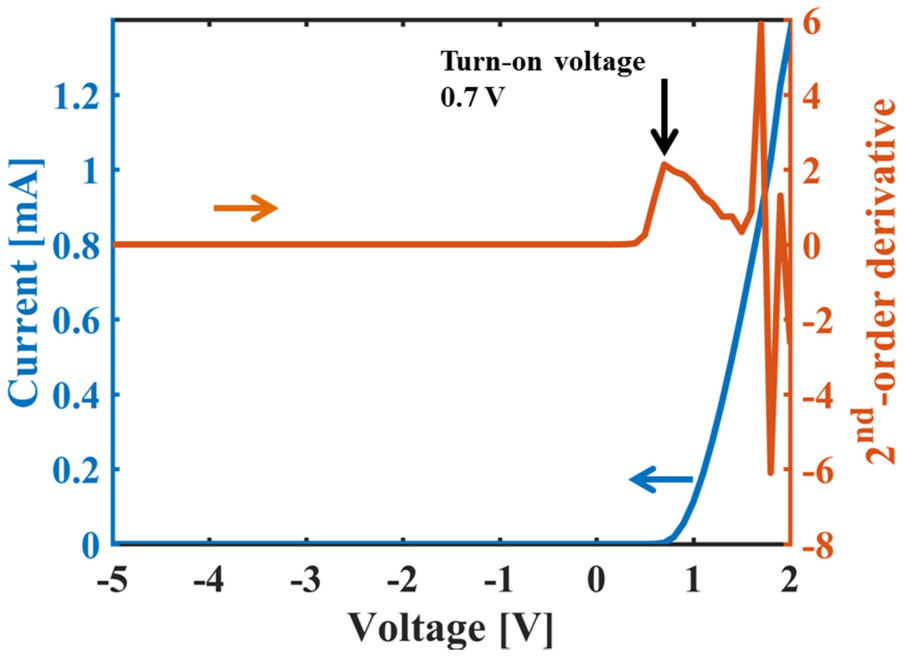

Figure 3.4 I-V curve (blue) and its 2nd-order derivative (red) to show the turn-on voltage.

Prior to the eye-diagram measurement, the turn-on voltage of the p-n junction is required. Figure 3.4 shows the measured current-voltage curve (IV curve) for the DUT studied here and its 2nd-order derivative. The turn-on voltage can be related to the voltage at which the first peak appears for the 2nd-order derivative and found to be 0.7 V. The signal generator produced a 10 Gb/s 2^{31}-1 non-return-to-zero pseudorandom binary sequence (NRZ PRBS) signal with a 2.5 V V_{pp}. Figure 3.5 (a) ~ (d) are the four captured eye-diagrams with the reverse bias gradually changing from -2 V to -1.7 V. The laser wavelength was detuned by around -10 pm on the blue side of resonance so that the one level corresponds to a condition of higher reverse bias. Figure 3.5 (a) and (b) both show undistorted modulation with clean one and zero levels, indicating that the p-n junction is maintained in the depletion mode. On the contrary, the zero level in Figure 3.5 (c) begins to become distorted while the zero level in Figure 3.5 (d) becomes very noisy, meaning

that the p-n junction was turned on during the voltage swing, and has switched from the depletion mode to the injection mode. Since the turn-on voltage is 0.7 V and the reverse bias is -1.7 V in Figure 3.5 (d), the effective V_{pp} can be accordingly determined to be 4.8 V (2 × (1.7 V + 0.7 V)).

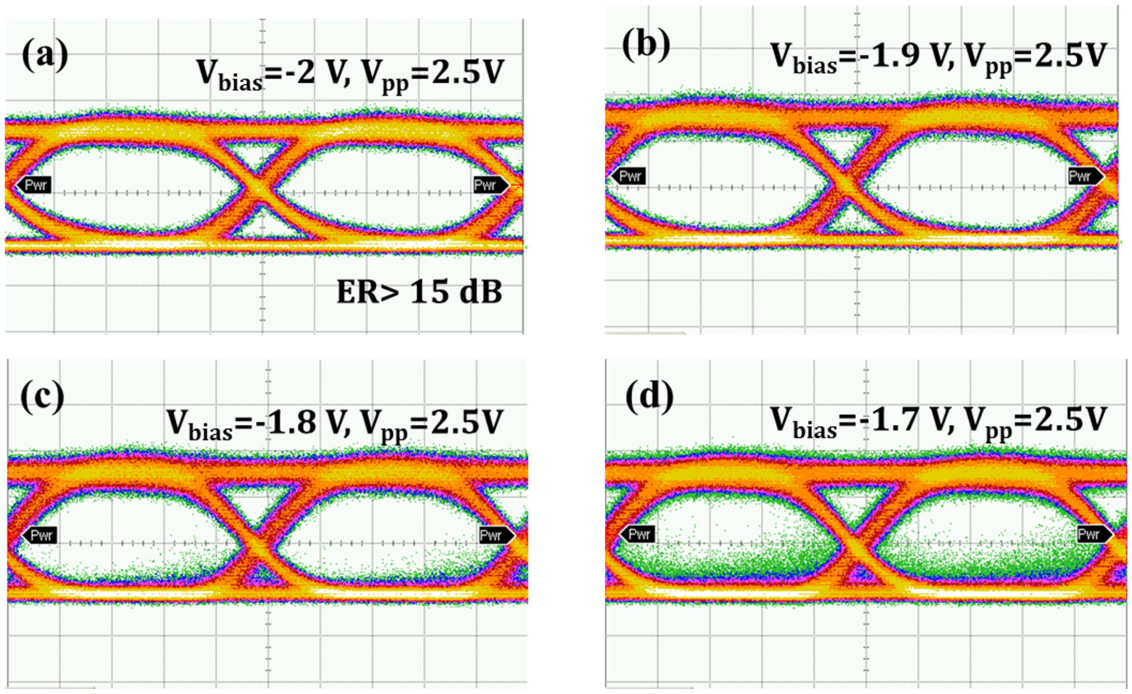

Figure 3.5 Eye diagrams at different voltages (a) -2 V; (b) -1.9 V; (c) -1.8 V; (d) -1.7 V. The V_{pp} is 2.5 V and the signal is 10 Gbps NRZ PRBS pulse train.

3.2 Chirp analysis

The voltage-dependent, small-signal α-parameter [16] is used to investigate the steady-state chirp of the device and its mathematical expression is given as:

$$\alpha(V) = -I(V)\frac{d\phi(V)}{dI(V)} \tag{3.1}$$

where $I(V)$ and $I(V)$ are the steady-state, voltage-dependent intensity and phase at a given detuning respectively. The negative sign is added in Eq. (3.1) to maintain consistency with the time-dependent phase factor $e^{-j\omega t}$ previously used in equations (2.29) and (2.46). The α-parameter can be calculated once the intensity and phase response are both known. The steady-state intensity has been readily given by the DC spectrum as shown in Figure 3.2. The phase response can be numerically reconstructed by the curve-fit method [17]. To ensure the stability and accuracy of the fitting, multiple intensity responses measured at different reverse biases are simultaneously fitted onto the corresponding theoretical equation that is defined as the absolute square of Eq. (2.29), resulting in an extraction of three parameters a , t , and n_{eff} . Therefore, the phase response can be calculated by computing the argument of Eq. (2.29). Three boundary conditions are imposed for the fitting: 1) the through-coupling coefficient t remains unchanged regardless of the bias voltage; 2) the propagation coefficient a can only increase with an increased reverse bias that causes less carrier-induced absorption; 3) $t < a$ must always hold for the over-coupled condition confirmed by the experimental result. The results of the curve fitting on the multiple intensity responses and the numerically reconstructed phase responses are shown in Figure 3.6 (a) and (b), respectively.

The α-parameter for various detunings on both blue (denoted as $\delta\lambda$) and red side (denoted as $\delta\lambda'$) of resonance are calculated and shown in Figure 3.7, using $I(V)$ and $\phi(V)$ extracted from the intensity and phase responses. Some important information can be obtained from Figure 3.7. Firstly, it is possible to have opposite chirps in an over-coupled Si-MRR modulator, depending on the side of the slope used for modulation. This has been discussed briefly in the previous chapter and here it is explicitly demonstrated that the sign of the chirp is ultimately determined by the intensity-phase relation.

Secondly, the magnitude of the chirp, in general, is lower under a smaller bias voltage. A smaller negative chirp can tolerate a larger positive dispersion because it "slows down" the pulse compression during which the signal falling edge is travelling faster than the signal rising edge. Thus, the modulated pulse can propagate in a longer link without significant distortion caused by pulse broadening. However, as discussed previously, the device performance depends on not only the modulation chirp but also other properties such as the insertion loss and extinction ratio that can usually benefit from a larger driving voltage particularly for depletion-type Si-MRRs. Thirdly, a larger detuning generally yields a larger chirp with only one exception, i.e. when the chirp tends to increase dramatically at the off state when the detuning is small. This is similar to the condition that the α-parameter of a single-drive Mach-Zehnder modulator tends to become infinite at the off state. However, it should be noted that the near-resonance state corresponds to the off state of the modulation so that the effective chirp weighted by the transmitted optical power is negligible, provided that a deep-notch intensity response is attained.

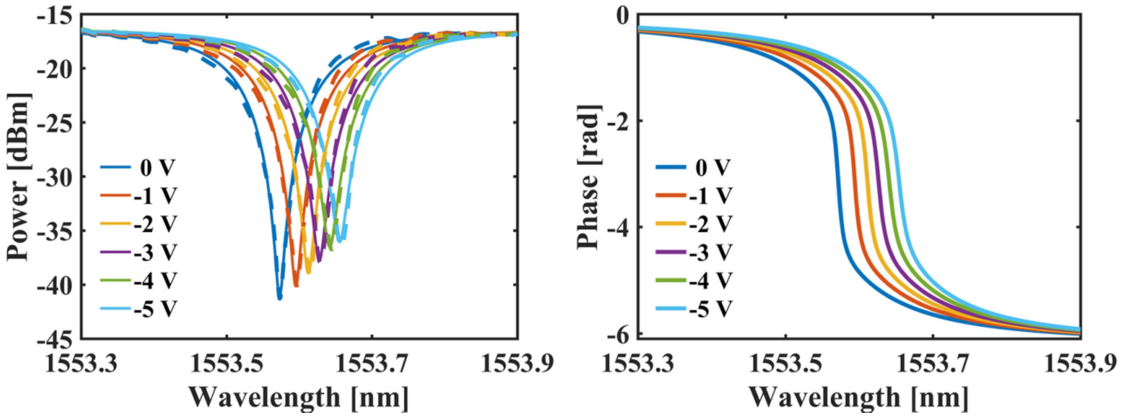

Figure 3.6 (a) Curve fitting on multiple intensity responses at reverse bias from 0 V to -5 V. Solid line and dashed line represent the fitted curve and measured curve, respectively. (b) Reconstructed phase responses.

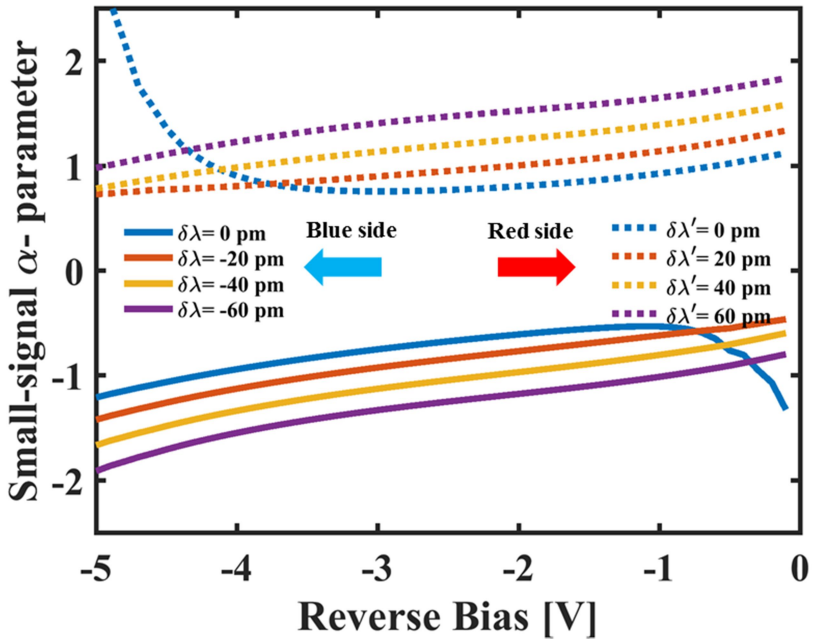

Figure 3.7 Calculated voltage-dependent, small signal α-parameters for various detunings on the blue side ($\delta\lambda$) and red side ($\delta\lambda'$) of resonance

The α-parameter based on the steady-state response can only be considered as semi-quantitatively since the chirp itself is a dynamic term. The dynamic response of the Si-MRR under the large-signal modulation, such as overshoot, should also have an impact on the total chirp generated. Therefore, the on/off α-parameter is used to quantify the large-signal chirp and is defined as [18]:

$$\alpha_{\text{on/off}} = -2\frac{\phi(\text{on})-\phi(\text{off})}{\ln\left(I(\text{on})\right)-\ln\left(I(\text{off})\right)} \tag{3.2}$$

where the instantaneous intensity and phase output at the on and off states needs to be obtained from the temporal response of the modulated signal. Thus, the CMT simulation can be conveniently used to find the solution for the temporal response, the detail of which has been given in section 2.3.3. V_{pp} is set to be 5 V while the DC bias is -2.5 V.

The raised cosine pulse has a roll-off factor of 0.5 and the electrical *RC*-constant is estimated to be 5 ps for the simulation. The simulated temporal response for a bit pattern 010 as an example is shown in Figure 3.9 (a) where the positions which are used to account for the on (maximum intensity at overshoot) and off states are marked by the two black dots. The calculated $\alpha_{on/off}$ with respect to the V_{pp} between -5 V and -1 V for several detunings on the blue side are then plotted in Figure 3.9 (b). The result shows that $\alpha_{on/off}$ reduces as the detuning becomes smaller except when the detuning is close to resonance, which is consistent with the analysis made for the small-signal α-parameter.

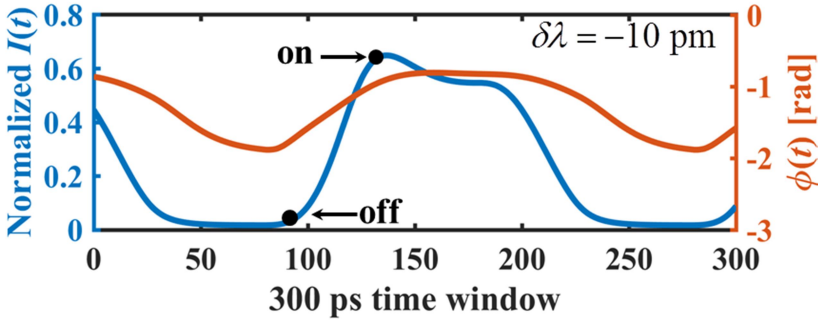

Figure 3.8 Temporal response for bit pattern 101, using the CMT simulation. The detuning is -10 pm at blue side.

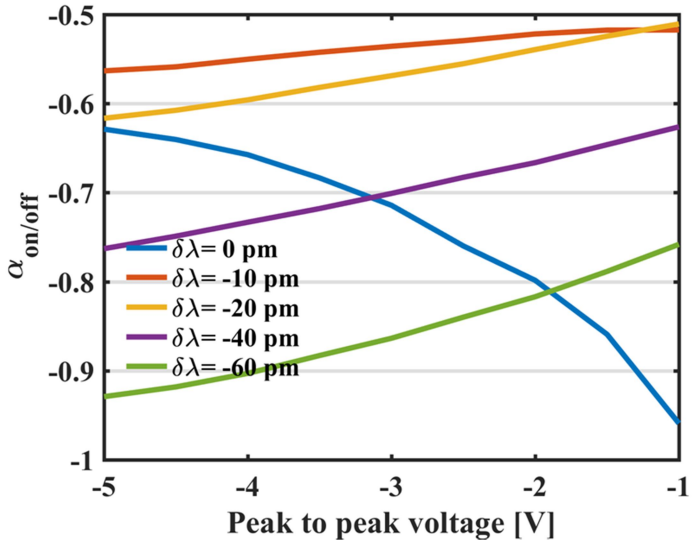

Figure 3.9 Calculated $\alpha_{on/off}$ for various detunings at blue side.

3.3 Transmission measurement

The BER measurement was preformed to validate the dispersion tolerance of the over-coupled Si-MRR described here. The schematic of the setup is shown in Figure 3.10. A signal generator provided a 10 Gb/s 2^{31}-1 NRZ PRBS signal with V_{pp} of 2.5 V. The effective V_{pp} is approximately double this value (determined to be 4.8 V) owing to the RF reflection under impedance mismatch. The optimal DC bias was -2 V, producing a maximized extinction ratio, meaning that the device was operating under the small forward bias but still below the turn-on voltage for the entire duty cycle. The detuning for the device was set to be approximately -10 pm on the blue side of the resonance, corresponding to relatively low chirp. As a result, a 14.7 dB extinction ratio was achieved by assessing the eye diagram obtained from the back-to-back measurement using an oscilloscope. It should be mentioned that an extinction ratio in excess of 13 dB is usually required for the commercialized Lithium-Niobate Mach-Zehnder modulators in typical 10 Gb/s fiber communication systems. In addition to the large extinction ratio, the insertion loss for the Si-MRR was as low as 2.5 dB (estimated by the optical power at the on state). Thermal stability was provided by an external TEC that maintained the sub-mount temperature. An erbium doped fiber amplifier (EDFA) with a 25 dB constant gain was added at the device output to compensate the coupling loss introduced by the surface gratings. A narrow-band optical filter was used to suppress the amplified spontaneous emission (ASE) noise. The optical power was limited to be 5 dBm in order to avoid excessive non-linear effects in the fiber link that ranged up to a maximum of 100 km. A pre-amplified detection scheme was implemented at the receiver end that included a second EDFA and a high-speed PIN photodiode. The second EDFA fixed the optical input power for the PIN at 0.5 mW so that the electrical noise (the shot noise is only related to the input power as shown in Eq. (2.52)) remained the same for all BER

measurements. Thus, the dominant noise source in the BER measurement was the ASE noise proportional to the gain of the second EDFA. The quality of the received signal was examined using the eye diagram measured by an oscilloscope. The BER test set included an automatically clock recovery unit as well as the automatic voltage decision level search that can be also manually adjusted for finer optimization. Finally, the BER at different received power was recorded by using a variable optical attenuator (VOA) that varies the optical power before the pre-amplified receiver.

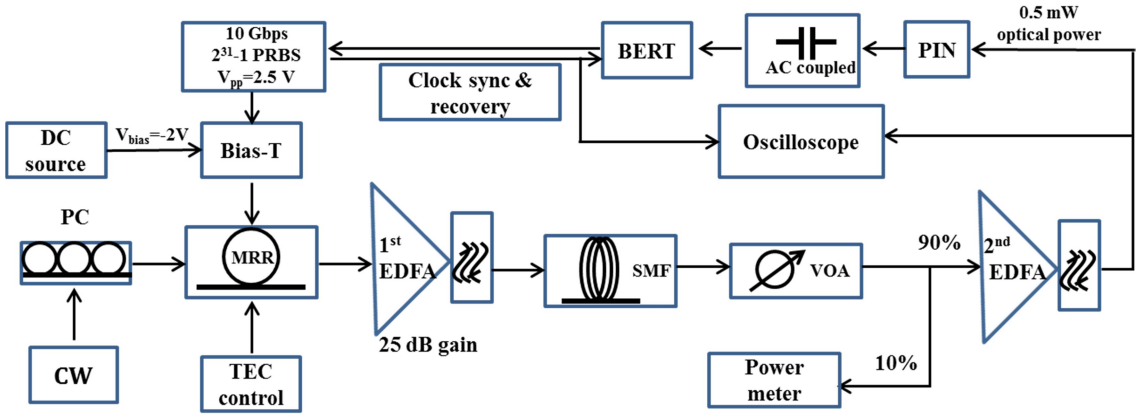

Figure 3.10 Experimental setup for the BER measurement. SMF: single mode fiber. EDFA: erbium-doped fiber amplifier. VOA: variable optical attenuator. BERT: bit error rate tester.

The measured BER curves for the fiber links ranging from 0 km to 100 km are plotted in Figure 3.11, along with the eye-diagrams associated to the corresponding links. It is clearly observed from the eye diagrams below 60 km that the extinction ratios are increased compared to the back-to-back eye diagram, leading to an improved signal quality. The reason is due to the pulse compression that occurs in the negative-chirp modulation. As the link distance extends above 60 km, the eye diagrams are more distorted owing to the increase in the total fiber dispersion as well as the increasing noise introduced by the second EDFA that provides a higher gain to compensate the higher

propagation loss in the pre-amplified detection scheme, leading to a reduced signal-to-noise ratio. The amplifier noise predominantly contributes the signal-spontaneous beat noise in the receiver, causing a noisier '1' level which is observed in the eye diagrams.

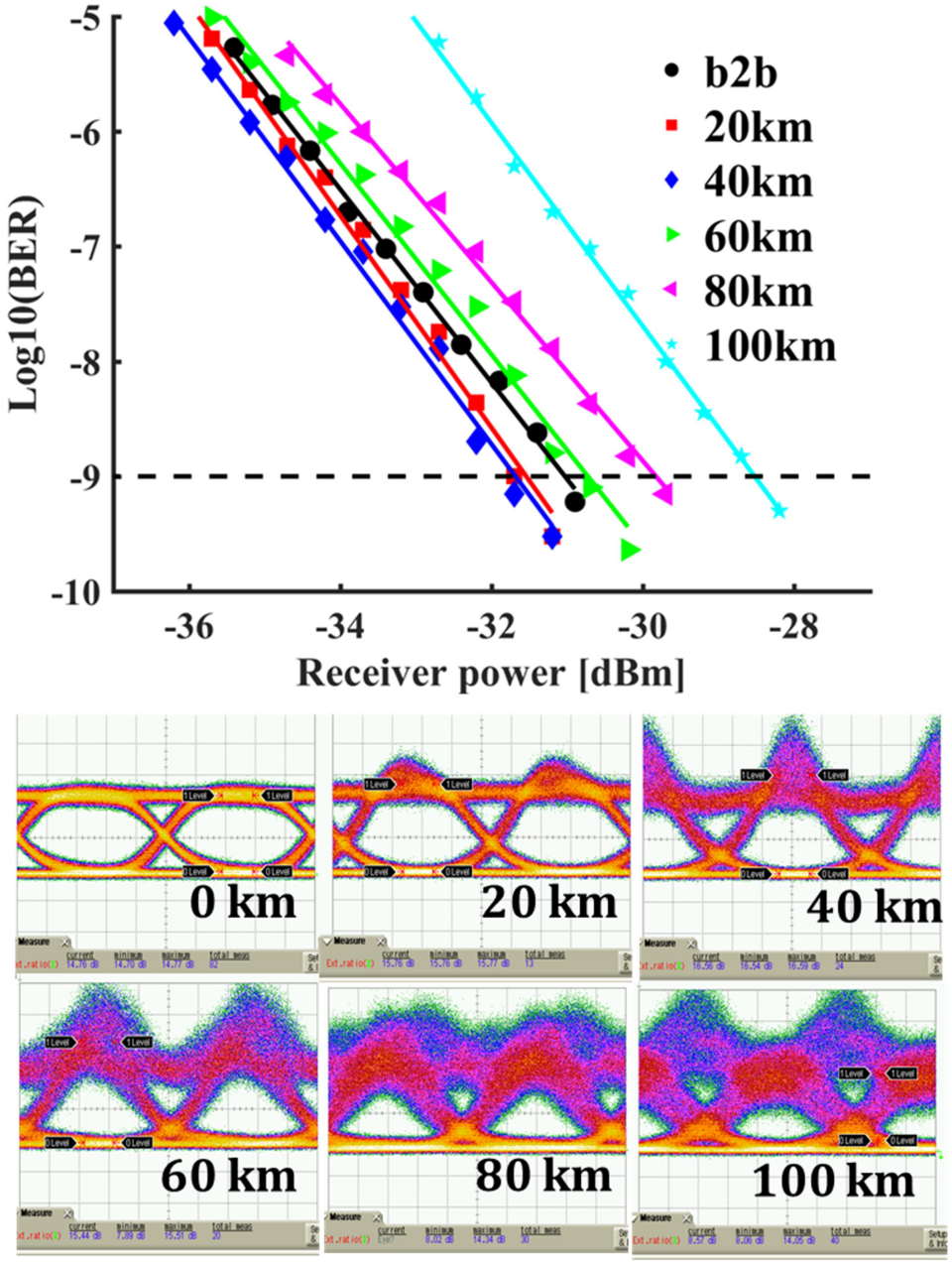

Figure 3.11 Plot of BER measurement results and the recorded eye diagrams.

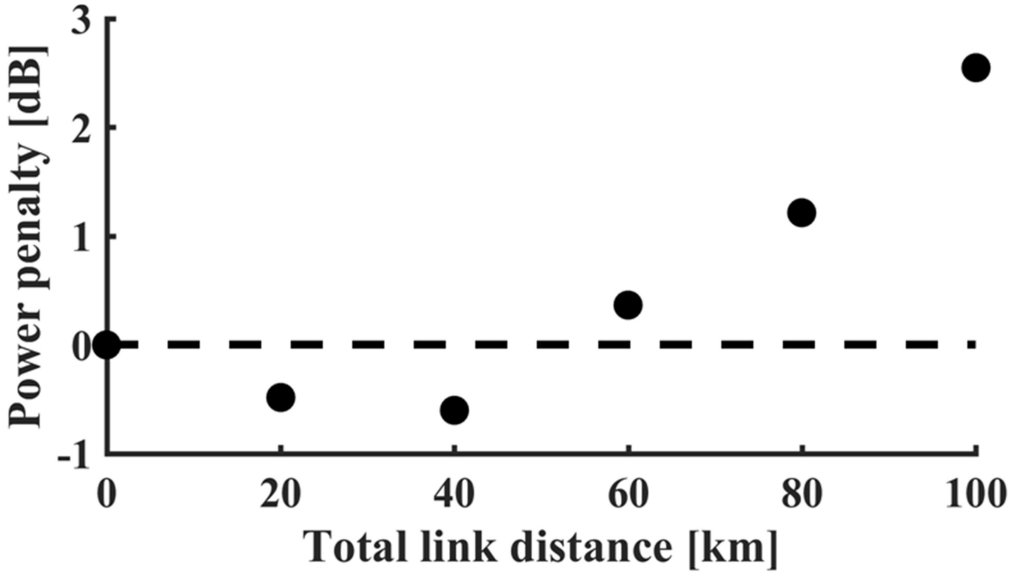

Figure 3.12 Chirp-induced power penalty for 0 km to 100 km link distance.

The chirp-induced power penalty previously described in section 2.4.4 is plotted in Figure 3.12 by normalizing the received powers at BER=10^{-9} for all the curves with respect to the one for the back-to-back measurement. A negative power penalty remains until approximately 50 km, which results in an improved receiver sensitivity. The power penalty for the 100 km was measured to be only 2.5 dB, which to the best of my knowledge is the lowest value achieved for similar kinds of links using the Si-MRR modulator in extended reach.

Reference

[1] M. Asghari and A. V. Krishnamoorthy, "Silicon photonics: Energy-efficient communication," *Nat. Photonics*, vol. 5, no. 5, pp. 268–270, 2011.

[2] G. Li, A. V Krishnamoorthy, I. Shubin, J. Yao, Y. Luo, H. Thacker, X. Zheng, K. Raj, and J. E. Cunningham, "Ring resonator modulators in silicon for interchip photonic links," *IEEE J. Sel. Top. Quantum Electron.*, vol. 19, no. 6, pp. 95–113, 2013.

[3] B. G. Lee, A. Biberman, J. Chan, and K. Bergman, "High-performance modulators and switches for silicon photonic networks-on-Chip," *IEEE J. Sel. Top. Quantum Electron.*, vol. 16, no. 1, pp. 6–22, 2010.

[4] S. Manipatruni, L. Chen, and M. Lipson, "Ultra high bandwidth WDM using silicon microring modulators.," *Opt. Express*, vol. 18, no. 16, pp. 16858–67, Aug. 2010.

[5] R. Nagarajan, M. Kato, J. Pleumeekers, P. Evans, S. Corzine, S. Hurtt, A. Dentai, S. Murthy, M. Missey, R. Muthiah, R. A. Salvatore, C. Joyner, R. Schneider, M. Ziari, F. Kish, and D. Welch, "InP photonic integrated circuits," *IEEE J. Sel. Top. Quantum Electron.*, vol. 16, no. 5, pp. 1113–1125, Sep. 2010.

[6] E. L. Wooten, K. M. Kissa, A. Yi-Yan, E. J. Murphy, D. a. Lafaw, P. F. Hallemeier, D. Maack, D. V. Attanasio, D. J. Fritz, G. J. McBrien, and D. E. Bossi, "A review of lithium niobate modulators for fiber-optic communications systems," *IEEE J. Sel. Top. Quantum Electron.*, vol. 6, no. 1, pp. 69–82, 2000.

[7] Y. Yamamoto and T. Kimura, "Coherent optical fiber transmission systems," *IEEE J. Quantum Electron.*, vol. 17, no. 6, pp. 919–935, Jun. 1981.

[8] D. Thomson, F. Gardes, S. Liu, H. Porte, L. Zimmermann, J. Fedeli, Y. Hu, M. Nedeljkovic, X. Yang, P. Petropoulos, and G. Mashanovich, "High performance Mach-Zehnder based silicon optical modulators," *IEEE J. Sel. Top. Quantum Electron.*, vol. 19, no. 6, pp. 85-94, 2013.

[9] L. Zhang, Y. Li, and J. Yang, "Silicon-based microring resonator modulators for intensity modulation," *Quantum Electron.*, vol. 16, no. 1, pp. 149–158, 2010.

[10] A. Biberman, S. Manipatruni, N. Ophir, L. Chen, M. Lipson, and K. Bergman, "First demonstration of long-haul transmission using silicon microring modulators.," *Opt. Express*, vol. 18, no. 15, pp. 15544–52, 2010.

[11] K. Padmaraju, N. Ophir, Q. Xu, B. Schmidt, J. Shakya, S. Manipatruni, M. Lipson, and K. Bergman, "Error-free transmission of microring-modulated BPSK," *Opt. Express*, vol. 20, no. 8, pp. 8681–8688, 2012.

[12] G. L. Li and P. K. L. Yu, "Optical intensity modulators for digital and analog applications," *J. Light. Technol.*, vol. 21, no. 9, pp. 2010–2030, 2003.

[13] A. H. Gnauck, S. K. Korotky, J. J. Veselka, J. Nagel, C. T. Kemmerer, W. J. Minford, and D. T. Moser, "Dispersion penalty reduction using an optical modulator with adjustable chirp," *IEEE Photonics Technol. Lett.*, vol. 3, no. 10, pp. 916–918, Oct. 1991.

[14] Z. Wang, Y. Gao, A. S. Kashi, J. Cartledge, and A. Knights, "Silicon micro-ring modulator for dispersion uncompensated transmission applications," *J. Light. Technol.*, vol. 34, no. 16, pp. 3675–3681, 2016.

[15] H. Yu, D. Ying, M. Pantouvaki, J. Van Campenhout, Y. Hao, J. Yang, and X. Jiang, "Trade-off between optical modulation amplitude and modulation bandwidth of silicon micro-ring modulators," vol. 22, no. 12, pp. 15178–15189, 2014.

[16] D. Petousi, L. Zimmermann, K. Voigt, and K. Petermann, "Performance limits of depletion-type silicon Mach–Zehnder modulators for telecom applications," *J. Light. Technol.*, vol. 31, no. 22, pp. 3556–3562, Nov. 2013.

[17] Z. Wang, E. Huante-Ceron, A. P. Knights, A. S. Karar, and J. C. Cartledge, "High-speed low-voltage BPSK modulation using a silicon micro-ring resonator," in *11th International Conference on Group IV Photonics (GFP), Paris*, 2014, pp. 51–52.

[18] J. C. Cartledge, "Comparison of effective -parameters for semiconductor Mach – Zehnder optical modulators," *J. Light. Technol.*, vol. 16, no. 3, pp. 372–379, 1998.

Chapter 4 Advanced modulation using silicon micro-ring resonator modulators

Driven by the exponential growth of IT services, such as high-definition video streaming and cloud computing, there is an increasing demand for communication systems in the data centre to have larger capacity and higher bandwidth. In a WDM system with a simple implementation of on-off modulation, the maximum achievable capacity per single channel is limited by the channel spacing. Continuously increasing the number of WDM channel to gain the total capacity has met with a number of challenges, including a raised complexity of transceiver design as well as a prohibitive power consumption that results from the need for more optical sources. Therefore, spectrally efficient modulation enabled by Digital Signal Processing (DSP) has attracted much attention for silicon photonics systems in short and medium range links. DSP-based, multi-level, multi-dimensional (amplitude, phase and polarization) signaling allows for the highest data-rate in a single channel, thereby increasing the total system capacity. This chapter focuses on the realization of some advance modulations using Si-MRR modulators. Section 4.1 demonstrates experimental work on an efficient high-speed binary-phase-shift-keying (BPSK) modulation using an over-coupled Si-MRR modulator, which serves as the cornerstone for building higher-order coherent systems. Section 4.2 will focus on advanced modulation through an intensity-modulation, direct-detection approach (IM-DD) that is favorable for inter/intra datacentre link owing to its low implementation complexity and cost effectiveness. The experimental result for a 104 Gb/s half-cycle 16-QAM Nyquist subcarrier modulation is demonstrated using a single Si-

MRR modulator. This is the highest bit-rate demonstrated to date for a single channel, Si-MRR modulator.

4.1 BPSK modulation using silicon micro-ring resonator modulator

For coherent systems, the fundamental modulation format is *binary-phase-shift-keying* (BPSK) for which two transition states have the same amplitude but a π-phase shift. BPSK modulation can be used to build higher-order modulation formats such as the *quadrature-phase-shift-keying* (QPSK) and *quadrature-amplitude-modulation* (QAM) to ultimately provide high spectral efficiency. It is known that a single over-coupled Si-MRR modulator can be used to obtain BPSK modulation [1, 2]. Since a 2π phase shift occurs across the resonance such as that shown in Figure 2.15, there can be always found two operating points on either side of the resonance that have identical amplitudes but π phase difference due to the symmetry of the intensity response (thus providing a means for BPSK modulation). One of the highlighted problems with this scheme is the large driving voltage that is incompatible with CMOS electronics [3]. In this thesis, a 10 Gb/s BPSK modulation with only 2 V peak-to-peak driving voltage is experimentally demonstrated with a depletion-type Si-MRR modulator [4].

The design of a modulator suitable for BPSK modulation is similar to that described in section 3.1.1 since over-coupled Si-MRRs are required in both work. The phase response of the Si-MRR was characterized using a combination of a curve-fit method and direct phase response measurement. In section 3.2, the curve-fit method was explained as a numerical reconstruction of phase responses with imposed boundary conditions on multiple intensity responses measured at different reverse biases.

Additionally, direct phase response measurement was performed by an LUNA optical vector analyzer™ (OVA). The OVA measures the amplitude and phase response of the Jones matrix elements of the optical passive device under test, yielding a full optical *S*-parameter characterization [5]. In order to remove the phase noise generated by other passive components present in the measurement path (such as the straight waveguide, surface grating, etc.), a reference measurement with only a straight bus waveguide was made and the resulting phase response was then subtracted from the subsequent phase responses that had Si-MRRs in the measurement path.

Figure 4.1 shows the measured intensity and phase responses (dotted lines) of the selected over-coupled Si-MRR under bias voltages of 0 V and -2 V as well as data fits (solid lines) for a comparison. A good agreement can be seen between the results obtained from the two methods, particularly for the phase response, indicating a good accuracy and robustness for the curve fitting. A π-phase shift required for the BPSK modulation was achieved at the intersecting wavelength of the two intensity curves. Correspondingly, the required driving voltage is as low as 2 V, which results from a near critically coupled condition for which there is a sharp phase change around the resonance. However, for the same reason, the insertion loss can be seen to be approximately 10 dB. This insertion loss can be reduced by designing for operation further away from the critically coupled condition, which will accordingly increase the driving voltage. To obtain both small insertion loss and driving voltage, the injection-type Si-MRR modulator can be considered for its large modulation efficiency [6], albeit with a more complicated driver design.

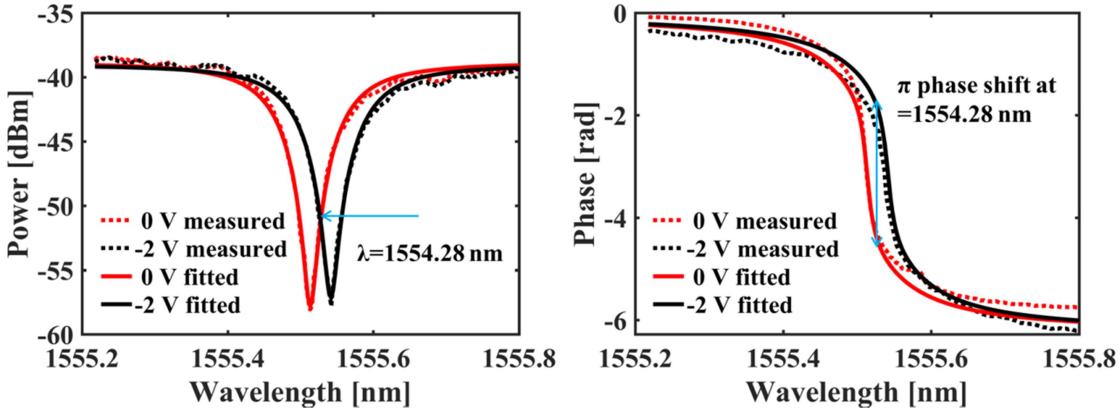

Figure 4.1 Measured and fitted intensity responses (left) and phase responses (right) at 0 V and -2 V. The π phase shift occurs at 1554.28 nm, pointed by the blue arrow.

The Q-factor of the device was estimated to be 11000, corresponding to an optical bandwidth of 17 GHz. The laser wavelength was initially set to be 1554.28 nm and a sub-mounted TEC then provided precise alignment of the operating wavelength for the BPSK modulation. The 10 Gb/s high-speed performance was investigated by eye-diagram measurements as shown in Figure 4.2. The signal generator produced a 10 Gb/s BPSK signal with a V_{pp} of 1 V, which gave an effective V_{pp} of 2 V on the p-n junction owing to RF reflection resulting from the impedance load mismatch. DC bias was set to be -1 V, ensuring operation in the depletion mode of the p-n junction. The optical eye diagram before demodulation shows a BPSK-like modulation of which two transitional states have the same intensity with an intensity dip due to the resonance crossover when one state transits into another state. The noise on the top floor, that should be absent, was caused by the pattern dependency of the MMR modulator. A commercial BPSK demodulator with balanced detection was employed to investigate the eye-diagram of the demodulated signal. The fully opened eye (extinction ratio > 10 dB) confirmed that the BPSK modulation was indeed achieved.

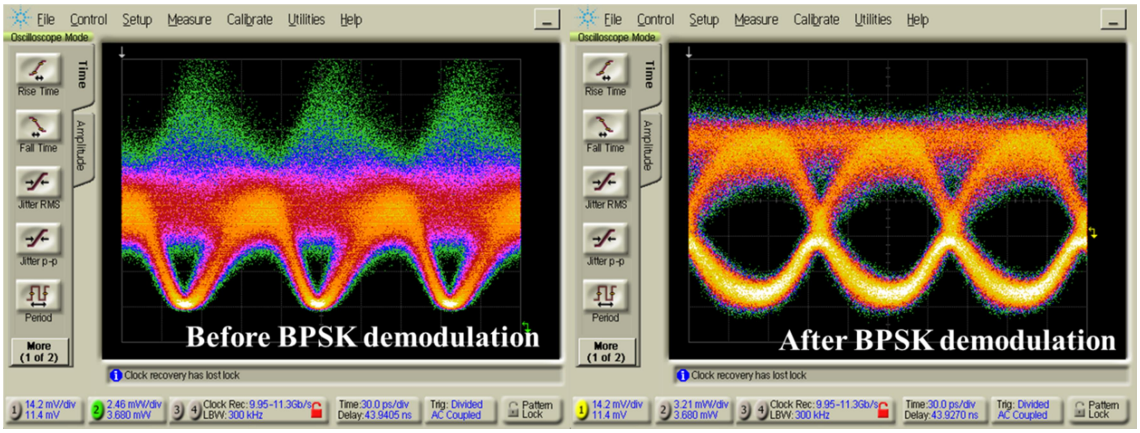

Figure 4.2 10 Gb/s BPSK measurements: optical eye diagram recorded before demodulation (left) and electrical eye diagram recorded after demodulation (right).

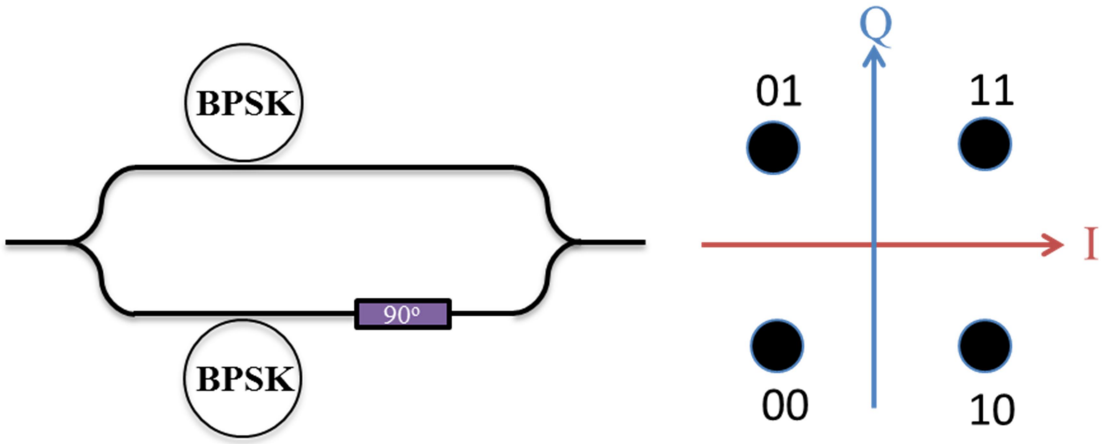

Figure 4.3 Schematic of QPSK modulator based on two Si-MRR BPSK modulators and the corresponding constellation diagram

Higher-order phase modulation can be built from the foundational measurement of this Si-MRR [7, 8]. For example, a QPSK modulator can be constructed by embedding two Si-MRR BPSK modulators onto a Mach-Zehnder interferometer (MZI) as shown in Figure 4.3. A 90-degree phase delay is implemented between two MZI arms so that one Si-MRR modulator operates in the in-phase plane whereas the other one operates in the quadrature plane. After the coherent recombination at MZI output, the modulated signal

will lead to four possible transition states as indicated by the constellation diagram (Figure 4.3 right), which doubles the spectral efficiency by encoding two bits into one symbol.

There are two significant problems in using an Si-MRR modulator in its simplest form (a single ring resonator with intra-cavity modulation) to achieve higher-order coherent modulation. The first one is the inherent modulation chirp associated with the non-zero phase response of the Si-MRR. The second is related to lack of fabrication tolerance. For the higher-order coherent device, each Si-MRR modulator is required to have a uniform performance in terms of field transfer, that unfortunately is not case due to fabrication variance (e.g. in an extreme scenario, an over-coupled condition can be switched to an under-coupled condition thus not supporting BPSK). Mitigation of some of the fabrication variance is achieved via thermal stabilization of each Si-MRR using a designated control circuit. The increased implementation complexity as well as the aggregated power consumption that results from thermal control on multiple MMR modulators may become prohibitive for cost-sensitive applications.

4.2 Nyquist single subcarrier modulation using silicon micro-ring resonator modulator

Cost effectiveness is essential for silicon photonic systems for short/medium reach applications [9]. Compared to coherent modulation where a balanced detector is needed, *Intensity-modulation-direct-detect* (IM-DD) is the most practical approach due to its relatively simple implementation consisting of a single modulator and a single photo-detector per optical carrier [10, 11]. Of the modulator designs available for intensity modulation, the Si-MRR modulator has been shown to combine a small footprint with

power efficiency and can be conveniently cascaded on a single bus to form an ultra-compact IM-DD WDM system [12]. Current 100 Gb/s systems (e.g. 100GE-SR4 [13]) features an on-off modulation, four-channel IM-DD approach that supports a data rate of 25 Gb/s per channel whereas four-channel IM-DD systems that support a data rate of 100 Gb/s per channel have become a major contender for the next-generation 400 Gb/s system. Scaling the bandwidth of the Si-MRR modulator to accommodate 100 Gb/s per channel presents many technical challenges such as an inherent bandwidth-efficiency tradeoff and nonlinear modulation dynamic [14], apart from the spacing limit for WDM channel, which makes *digital signal processing* (DSP)-enabled spectrally efficient modulation formats particularly attractive [15]. M-level *pulse amplitude modulation* (M-PAM) and subcarrier modulation are the most common advanced modulations for an IM-DD system [16]. Although M-PAM is straightforward, it only provides one-dimensional modulation (amplitude) and exhibits poor receiver sensitivity especially for extended reach. Subcarrier modulation, on the other hand, is a 2-dimensional modulation scheme (amplitude and phase) allowing QAM signal encoding on an RF subcarrier, thereby increasing the receiver sensitivity. Furthermore, it also provides more flexibility for scaling the data rate as the QAM signal can be increased to higher modes. Among the different subcarrier modulation techniques *orthogonal frequency division multiplexing* (OFDM), *discrete-multi tone* (DMT) modulation, and *Nyquist subcarrier modulation* (N-SCM) can provide comparable spectral efficiencies [17]. However, N-SCM provides a low-complexity and low-cost DSP design that utilizes a single RF subcarrier (in contrast to other techniques that require multiple RF subcarriers) [18]. As a result, N-SCM does not need fast Fourier transform processing at both ends of the transceiver as well as the adaptive power and bit loading that requires a feedback from receiver to the transmitter, thereby improving the power efficiency [19]. All three techniques described have been

studied extensively for long-reach system as well as short reach. 100 Gb/s and above data rates per single optical carrier based on subcarrier modulations have been demonstrated using Si-MRR [20, 21] or other types of silicon modulators [22, 23]. In this thesis, I will demonstrate a 104 Gb/s 16-QAM N-SCM for back-to-back transmission. This is the first experimental result of its kind demonstrating the highest reported bit rate for a single Si-MRR modulator operated in an IM-DD system.

4.2.1 Concept of Nyquist pulse shaped subcarrier modulation (N-SCM)

The concept of N-SCM is explained by Figure 4.4 where a baseband NRZ signal with a symbol rate of B_s is chosen arbitrarily as an example. The bandwidth of a digital signal is normally very large, which causes *inter-symbol interference* (ISI) in a typically band-limited transmission channel. Therefore, this baseband signal bandwidth is usually limited by the pulse shaping using a Nyquist filter such as the raised cosine filter introduced in section 2.4.2, that fulfills the zero-ISI criterion. The bandwidth of the raised cosine filter is determined by the roll-off factor β. The Nyquist criterion requires that the minimum bandwidth to be transmitted without signal degradation needs to be $B_s/2$ that corresponds to a maximum spectral efficiency for a given baseband signal, which can be achieved by an ideal filter with $\beta = 0$. The filtered, band-limited signal is up-converted by a RF subcarrier that provides a direct intensity modulation to the optical modulator. The smallest frequency f_{sc} of the RF subcarrier without inducing aliasing is equal to the bandwidth of the Nyquist filter (measured in the baseband). The spectral efficiency can be further scaled by applying a QAM signal onto the RF subcarrier. Half-cycle N-SCM is defined when $\beta = 0$, leading to the most spectrally-efficient modulation with a null-to-null electrical bandwidth of B_s. Single-cycle N-SCM is defined when $\beta = 1$, leading to a null-to-null electrical bandwidth of $2B_s$ that is the least spectrally efficient. The

characteristic of sub-cycle N-SCM falls in the middle. Choosing different roll-off factors results in a tradeoff between the filter design complexity and the spectral efficiency. As the filter is implemented in the time domain by DSP, also known as the *finite impulse response* (FIR) filter, a smaller β can yield a larger spectral efficiency but in the meantime requires more taps for the FIR, leading to increased complexity and power consumption. It should be noted that the added advantage of a higher spectral efficiency is the reduced requirement for the modulator bandwidth, which is sometimes critical for the Si-MRR modulator that suffers from the bandwidth-efficiency tradeoff.

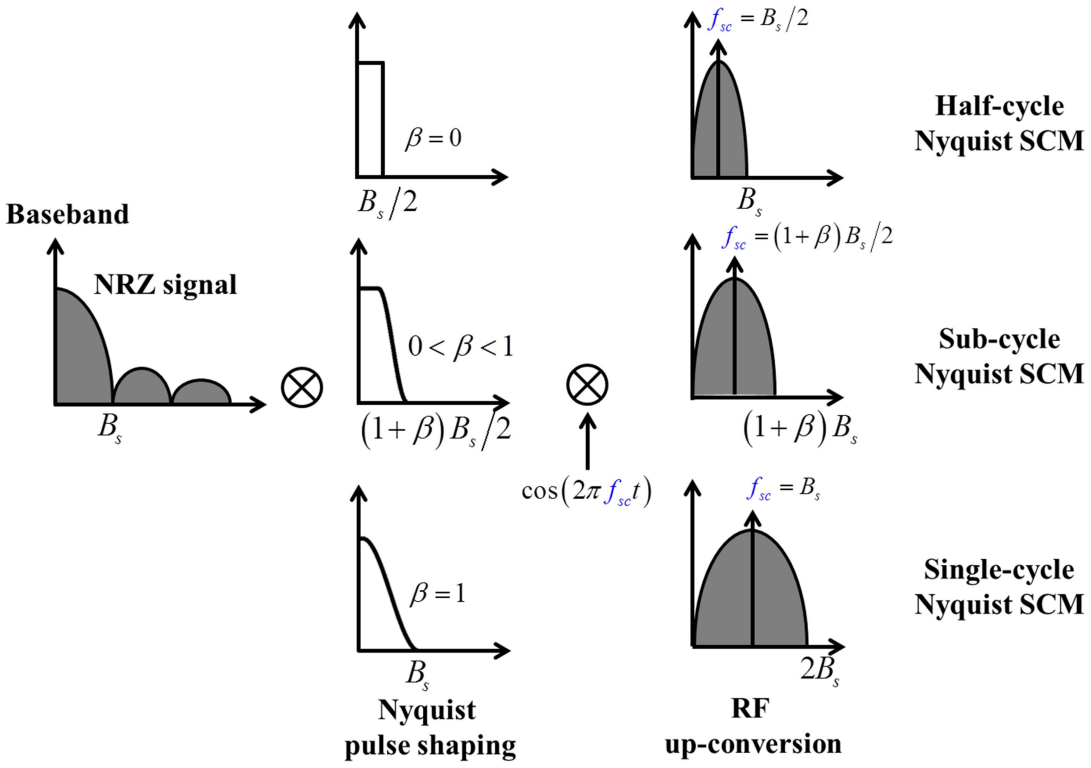

Figure 4.4 Principle of Nyquist pulse shaped subcarrier modulation.

4.2.2 N-SCM Transceiver DSP architecture

The transceiver DSP design for the N-SCM experiment is shown in Figure 4.5. The transmitter DSP was performed by a programmable arbitrary waveform generator (AWG) in which a 2^{15} de Bruijn bit sequence was first mapped onto 16-QAM symbols. Then, the baseband signals for I- and Q- components were band-limited by a root raised cosine (RRC) filter. The frequency response of the RRC filter is defined as the square root of Eq. (2.47) so that a matched filter (RRC filter itself) was added in the receiver DSP in order to have an overall identical filtering response as that provided by a single raised cosine filter at the transmitter. The reason for using a pair of RRC filters is to maximize the signal-to-noise ratio at the receiver while still maintaining the zero-ISI condition. The roll-off factor β was chosen to be zero in order to have a minimum demand for the modulator bandwidth that was later found to be the main limiting factor for the system performance. An important optimization in the transmitter DSP is electrical pre-compensation achieved by a frequency-domain equalization [24], which is mathematically described as

$$s'(t) = IFFT\left(\frac{S(f)}{H(f)}\right) \tag{4.1}$$

where $s'(t)$ is the time-domain signal after the pre-compensation, $S(f)$ is the complex frequency response of the signal before the pre-compensation and $H(f)$ is the complex small-signal frequency response for the end-to-end channel. By inversely multiplying $H(f)$, the signal at the transmitter is pre-distorted so that the distortion caused by transmission in the channel will be eliminated at the receiver. $H(f)$ was measured by transmitting 320 frequency tones, equally distributed over 32 GHz (the bandwidth of the AWG), and determining the changes in the amplitudes and phases of the stimulus

frequencies at the receiver. To reduce the impact of additive noise, eight independent measurements were averaged. The downside of the pre-compensation is, however, the reduced signal-to-noise ratio due to the boosted high-frequency components. Finally, the filtered, pre-compensated I- and Q- components were up-converted, combined, and the generated digital RF signal was then converted into analog using an 8-bit *digital-to-analog converter* (DAC) operating at a sampling rate of 92 GSa/s before directly driving the Si-MRR modulator.

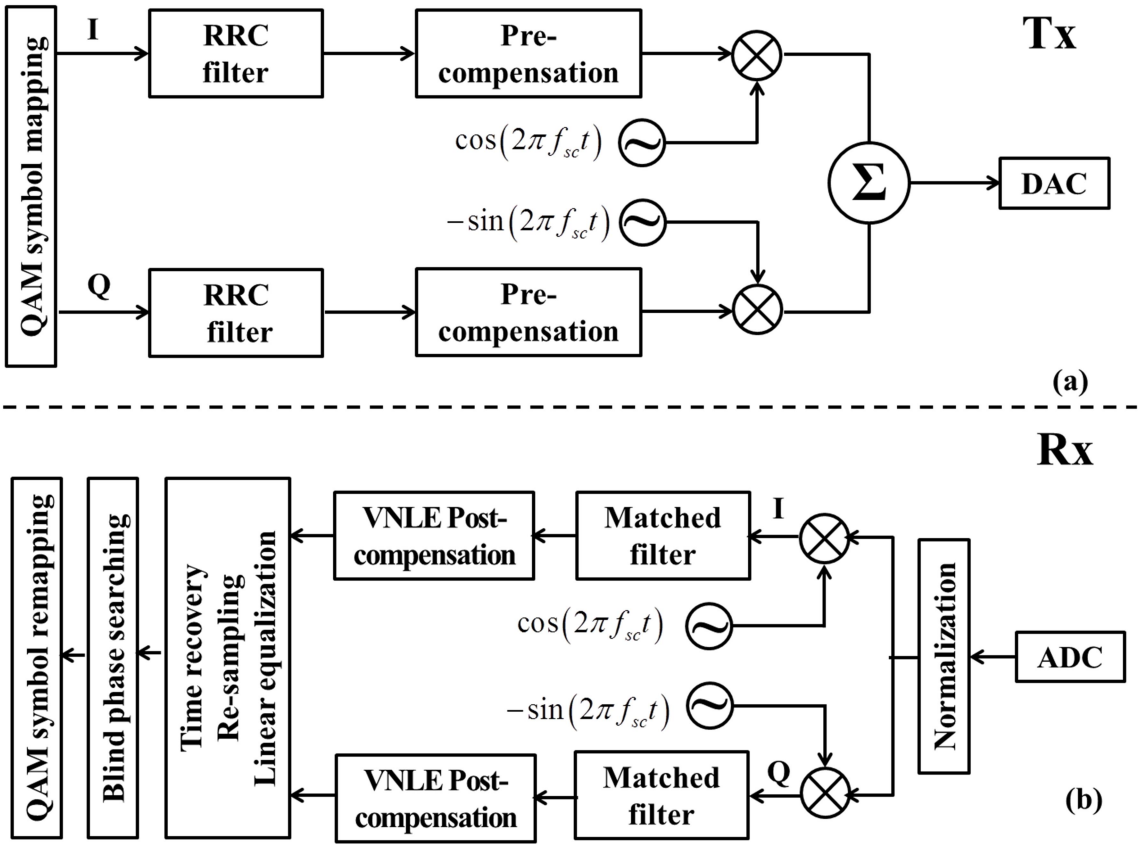

Figure 4.5 DSP architectures for Transmitter (Tx) and receiver (Rx). RRC: root raised cosine. DAC: digital-to-analog convertor. ADC: analog-to-digital convertor. VNLE: Volterra non-linear equalizer.

At the receiver, an 80 GSa/s *analog-to-digital converter* (ADC) provided by a real-time sampling scope was used to digitize the received optical signal into 5.6×10^5 symbols. For the offline receiver DSP, the signal was first normalized, down-converted and then match-filtered by the same RRC filter used in the transmitter DSP. A low-complexity second-order 7-tap *Volterra nonlinear equalizer* (VNLE) was applied to post-compensate the nonlinear modulation dynamics exhibited by the Si-MRR modulator, (e.g., from overshooting, plasma dispersion effects or the Lorentzian transfer function). This follows from previous work showing that the VNLE is efficient for post-compensating the nonlinearity resulting from a directly modulated laser in an IM-DD system [25], which exhibits some similarities with the Si-MRR modulator. The discrete-time Volterra series describing a nonlinear system with a finite memory length is given by

$$x^{'}(n) = \sum_{p=1}^{M} \sum_{k_1=0}^{N-1} \cdots \sum_{k_p=0}^{N-1} h_p\left(k_1, \cdots, k_p\right) \cdot \prod_{j=1}^{p} x\left(n - k_j\right) \tag{4.2}$$

where $x^{'}(n)$ and $x(n)$ are the output and input signals at a discrete time n, M is the order of Volterra series and N is the tap number representing the memory length. Further, $h_p\left(k_1, \cdots, k_p\right)$ is known as Volterra kernel coefficients that are obtained in a training phase using the recursive least square algorithm based on 16,000 training symbols. The coefficients were then fixed, as the nonlinear distortion introduced by the Si-MRR modulator is deterministic. The total number of kernel coefficients can be calculated by $\sum_{i=1}^{M} N^{i}$, which requires 56 multiplications to obtain a single sampled value for a second-order 7-tap VNLE. The order and tap number of the VNLE offer a trade-off between the accuracy and the implementation complexity. For an inexpensive IM-DD system, the VNLE ought to be as simple as possible. The VNLE design for the work described in this thesis resulted from the comparison of BER results in which higher-order VNLE did not

offer significant improvement. The N-SCM signal was recovered using a digital square and filter-retiming algorithm (re-sampled to 2 samples per symbol), followed by a 21-tap half-symbol-spaced linear equalizer that compensates the residual channel distortion. The filter taps were pre-converged using the constant modulus algorithm and then updated by the radius directed algorithm. Finally, using the blind phase searching algorithm, the 16-QAM N-SCM signal was re-mapped to bits for the bit error counting and BER calculation.

4.2.3 System characterization

The N-SCM measurement setup is shown in Figure 4.6. The analog RF signal at the output of the DAC was amplified to a peak-to-peak voltage of approximately 1.8 V before being applied to the Si-MRR modulator via a high-speed GSG probe. The DC bias was set to -2 V to ensure a depletion-mode operation on the p-n junction of the Si-MRR at all times. The laser with 5 dBm output power was maintained in the TE-mode by a polarization controller. Light was coupled into the chip through grating couplers that exhibited approximately 8 dB insertion loss for each. The modulated optical signal was amplified and then filtered before being launched into the single mode fiber. A variable tunable attenuator was used to adjust the power level at the receiver consisting of a PIN photodiode and transimpedance amplifier with a bandwidth of 40 GHz. Finally, the signal was captured and digitized by the real-time sampling scope for the offline receiver DSP.

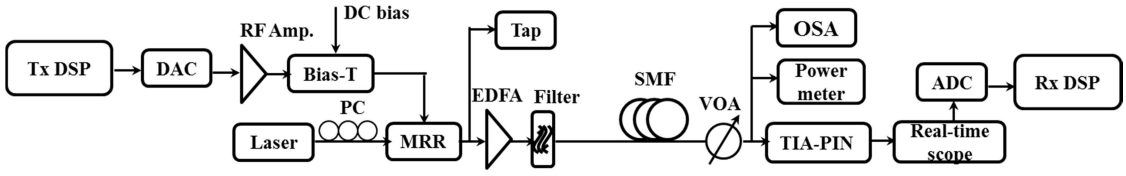

Figure 4.6 System build for N-SCM measurement. PC: polarization controller. SMF: single mode fiber. VOA: viable optical attenuator. OSA: optical spectrum analyzer. TIA: transimpedance amplifier.

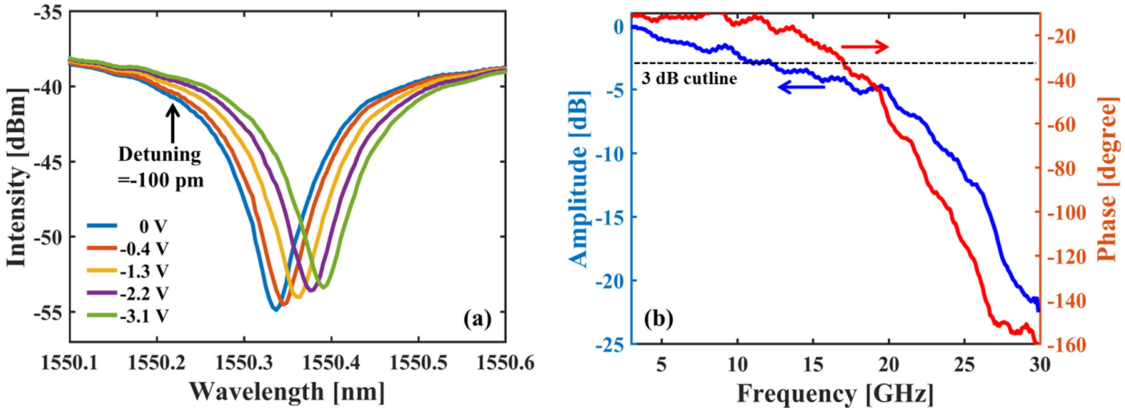

Figure 4.7 (a) Measured DC spectra at various reverse biases. (b) Measured system end-to-end small-signal response: amplitude (blue) and phase (red).

The Si-MRR modulator used for the N-SCM measurement was fabricated on 220 nm SOI with an add-drop configuration that allows for resonance control via a feedback from the drop-port power tap. The design of the p-n junction was similar to those previously demonstrated but with different doping concentrations. The carrier-induced absorption in the ring was estimated to be 50 dB/cm, while the ratio between the two field coupling coefficients at the through port and drop port, as given by Eq. (2.34), was optimized for large extinction ratio. DC spectra at different reverse biases are shown in Figure 4.7 (a), indicating a large modulation efficiency of 18.7 pm/V and a large notch depth (around 20 dB at zero bias). The Q-factor estimated by the 3-dB linewidth at zero bias is approximately 7000, corresponding to an optical bandwidth of 27.5 GHz. The detuning plays an important role in determining the system performance as it has been shown that a larger detuning generally can produce a better linearity and a larger bandwidth but come at the expense of a reduced extinction ratio [26]. The optimum detuning (pointed out in Figure 4.7 (a)) in the N-SCM experiment was obtained by comparing the BER with respect to incremental detuning steps and was found at -100 pm at which the system end-to-end response used for the electrical pre-compensation was

measured. The results are shown in Figure 4.7 (b), including the magnitude and phase response curves. The measured 3-dB bandwidth is about 14 GHz, significantly lower than the optical bandwidth determined by the Q-factor. The dominant sources of this bandwidth limit include the parasitic resistance and capacitance associated with the DUT as well as the impairment of other RF components in the system (in particular the RF probe).

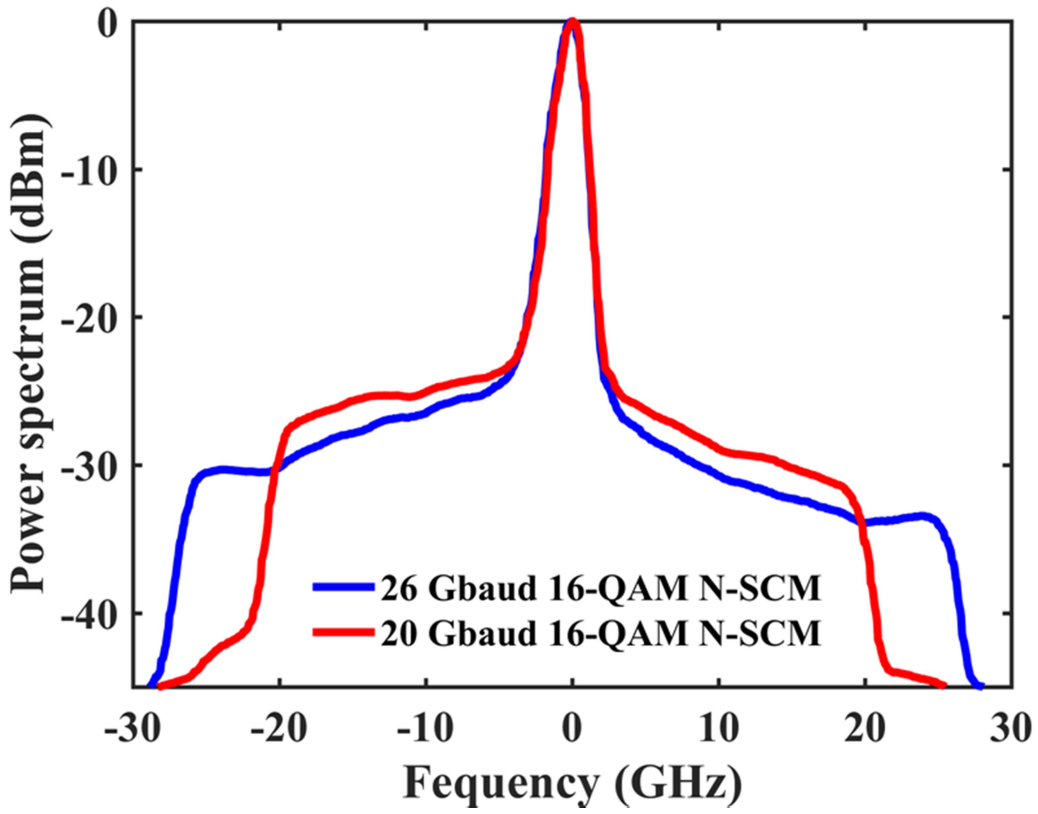

Figure 4.8 Measured optical spectra of 20 Gbaud and 26 Gbaud 16-QAM N-SCM signals

Figure 4.8 gives the optical spectra of modulated 16-QAM N-SCM signals at 20 Gbaud and 26 Gbaud (corresponding to 80 Gb/s and 104 Gb/s gross bit rate). The strong asymmetry between the magnitudes of the lower and upper sidebands is due to the optical

peaking effect [27] that enhances the side band closer to the resonance. Since the modulation occurred on the blue side, the sideband towards the lower frequency (towards resonance) was enhanced. The bandwidth at a -35 dB power level is 41 GHz and 52.3 GHz, are slightly larger than the doubled symbol rates demonstrating a good spectral efficiency owing to a nearly ideal filtering with $\beta = 0$.

4.2.4 16-QAM N-SCM BER measurement

Figure 4.9 (a) shows the BER results in the back-to-back measurement for the 16-QAM N-SCM signal at 20 Gbaud and 26 Gbaud under two conditions: with and without the VNLE in the receiver DSP in order to observe the effectiveness of the VNLE. The recovered constellation diagrams as shown in Figure 4.9 (b) ~ (e) are also used to qualitatively illustrate the signal degradation induced by the Si-MRR nonlinearity and the resulting improvement when the VNLE is used. The inhomogeneous divergence for the 16-QAM symbols, especially for the symbols at the outer corners, is caused by the increased nonlinear distortion at a larger detune. It can be also seen that the symbols with the VNLE are more converged compared to those without the VNLE. The lowest BERs achieved for the 20 Gbaud and 26 Gbaud signals were 7.8×10^{-4}.and 3.6×10^{-3} with the VNLE to compensate the nonlinear distortion of the Si-MRR modulator, which exhibits an order of magnitude of improvement over the BER results obtained without the VNLE. The maximum capacity that can be achieved for the 16-QAM NSCM, as discussed earlier, is limited by the bandwidth of the Si-MRR modulator as well as the electrical interface to the modulator. The reason can be explained by Figure 4.7(b), i.e. the magnitude of the roll-off of the system response at 20 GHz is 8 dB but dramatically increases to 20 dB at 27.5 GHz. The consequence for excessively amplifying the high-frequency components of the input signal is a reduced signal dynamic range and consequently a reduced signal-

to-noise ratio that adversely affects the system performance. However, it can be anticipated that with improvements in the electrical interface to the modulator and reducing RC constant of the junction, then a bit rate of 112 Gbit/s can be achieved with a BER below the hard-decision *forward error correction* (FEC) coding limit of 3.8×10^{-3} [28]. The combination of pre-/post-compensation and Nyquist pulse shaping enabled by inexpensive DSP presents an intriguing and practical approach for next-generation 100 Gbit/s per wavelength IM-DD systems based on the Si-MRR modulator.

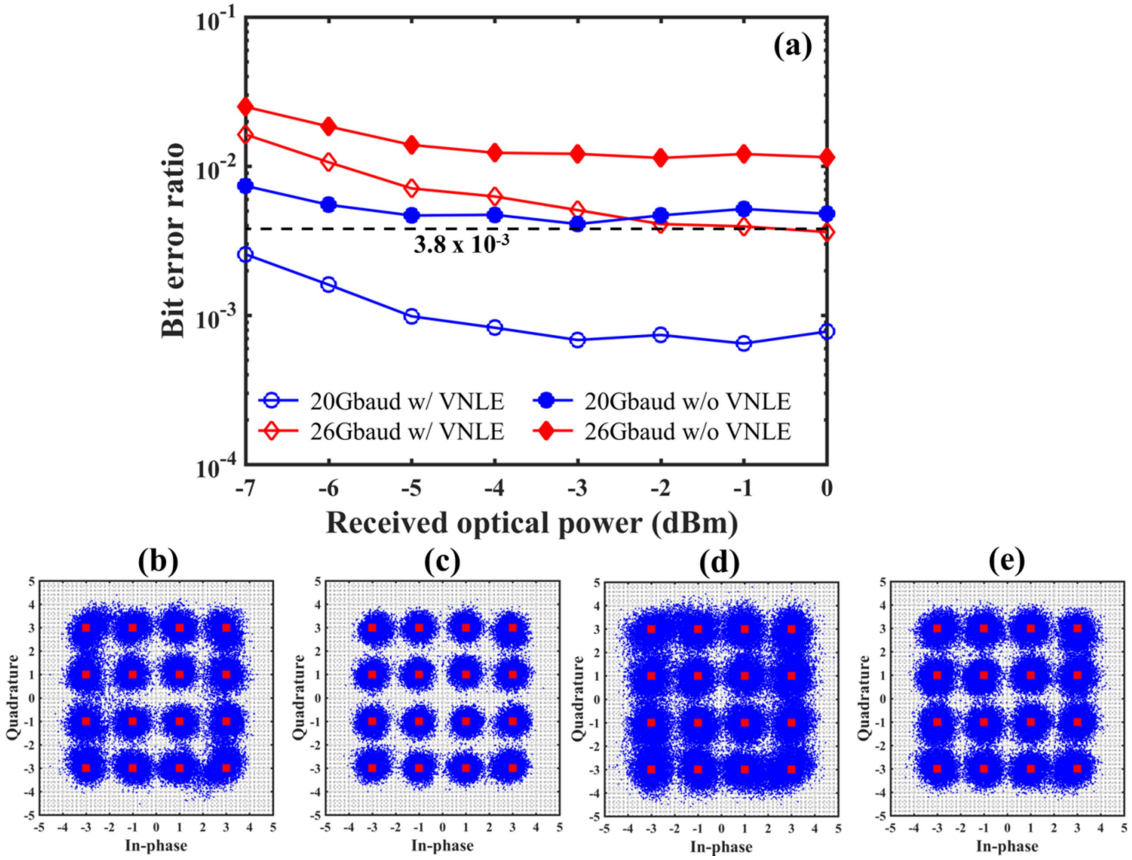

Figure 4.9 (a) Measured BER curves for 20 Gbaud and 26 Gbaud 16-QAM N-SCM signals in the back-to-back link. Recovered 16-QAM constellations diagram when the received optical power was 0 dBm: (b) 20 Gbaud without VNLE; (c) 20 Gbaud with VNLE; (d) 26 Gbaud without VNLE and (e) 26 Gbaud with VNLE.

Reference

[1] L. Zhang, J.-Y. Yang, M. Song, Y. Li, B. Zhang, R. G. Beausoleil, and A. E. Willner, "Microring-based modulation and demodulation of DPSK signal.," *Opt. Express*, vol. 15, no. 18, pp. 11564–9, Sep. 2007.

[2] K. Padmaraju, N. Ophir, Q. Xu, B. Schmidt, J. Shakya, S. Manipatruni, M. Lipson, and K. Bergman, "Error-free transmission of microring-modulated BPSK.," *Opt. Express*, vol. 20, no. 8, pp. 8681–8, Apr. 2012.

[3] T. Li, J. Zhang, H. Yi, W. Tan, Q. Long, Z. Zhou, X. Wang, and H. Wu, "Low-voltage, high speed, compact silicon modulator for BPSK modulation," *Opt. Express*, vol. 21, no. 20, pp. 23410–5, Oct. 2013.

[4] Z. Wang, E. Huante-Ceron, A. P. Knights, A. S. Karar, and J. C. Cartledge, "High-speed low-voltage BPSK modulation using a silicon micro-ring resonator," in *11th International Conference on Group IV Photonics (GFP),* Paris, 2014, pp. 51–52.

[5] D. K. Gifford, B. J. Soller, M. S. Wolfe, and M. E. Froggatt, "Optical vector network analyzer for single-scan measurements of loss, group delay, and polarization mode dispersion," *Appl. Opt.*, vol. 44, no. 34, pp. 7282–6, Dec. 2005.

[6] T. Baba, S. Akiyama, M. Imai, N. Hirayama, H. Takahashi, Y. Noguchi, T. Horikawa, and T. Usuki, "50-Gb / s ring-resonator-based silicon modulator," *Opt. Express*, vol. 21, no. 10, pp. 11869–76, 2013.

[7] L. Zhang, J. Yang, Y. Li, and M. Song, "Monolithic modulator and demodulator of differential quadrature phase-shift keying signals based on silicon microrings," *Opt. Lett.*, vol. 33, no. 13, pp. 1428–1430, 2008.

[8] P. Dong, C. Xie, L. Chen, N. K. Fontaine, and Y. Chen, "Experimental demonstration of microring quadrature phase-shift keying modulators.," *Opt. Lett.*, vol. 37, no. 7, pp. 1178–80, Apr. 2012.

[9] H. Liu, C. F. Lam, and C. Johnson, "Scaling optical interconnects in datacenter networks opportunities and challenges for WDM," in *2010 18th IEEE Symposium on High Performance Interconnects*, 2010, pp. 113–116.

[10] S. Randel, F. Breyer, S. C. J. Lee, and J. W. Walewski, "Advanced modulation schemes for short-range optical communications," *IEEE J. Sel. Top. Quantum Electron.*, vol. 16, no. 5, pp. 1280–1289, Sep. 2010.

[11] P. J. Winzer and R.-J. Essiambre, “Advanced modulation formats for high-capacity optical transport networks,” *J. Light. Technol.*, vol. 24, no. 12, pp. 4711–4728, Dec. 2006.

[12] C.-H. Chen, M. Ashkan Seyedi, M. Fiorentino, D. Livshits, A. Gubenko, S. Mikhrin, V. Mikhrin, and R. G. Beausoleil, “A comb laser-driven DWDM silicon photonic transmitter based on microring modulators,” *Opt. Express*, vol. 23, no. 16, pp. 21541–48, Aug. 2015.

[13] “Media Access Control Parameters, Physical Layers and Management Parameters for 40 Gb/s and 100 Gb/s Operation, IEEE Standard 802.3ba, 2010.”

[14] H. Yu, D. Ying, M. Pantouvaki, J. Van Campenhout, Y. Hao, J. Yang, and X. Jiang, “Trade-off between optical modulation amplitude and modulation bandwidth of silicon micro-ring modulators,” *Opt. Express*, vol. 22, no. 12, pp. 15178–15189, 2014.

[15] X. Liu, S. Chandrasekhar, and P. J. Winzer, “Digital signal processing techniques enabling multi-Tb\/s superchannel transmission: an overview of recent advances in DSP-enabled superchannels,” *IEEE Signal Process. Mag.*, vol. 31, no. 2, pp. 16–24, Mar. 2014.

[16] X. Xu, E. Zhou, G. N. Liu, T. Zuo, Q. Zhong, L. Zhang, Y. Bao, X. Zhang, J. Li, and Z. Li, “Advanced modulation formats for 400-Gbps short-reach optical inter-connection,” *Opt. Express*, vol. 23, no. 1, pp. 492–500, Jan. 2015.

[17] K. Zhong, X. Zhou, T. Gui, L. Tao, Y. Gao, W. Chen, J. Man, L. Zeng, A. P. T. Lau, and C. Lu, “Experimental study of PAM-4, CAP-16, and DMT for 100 Gb/s short reach optical transmission systems,” *Opt. Express*, vol. 23, no. 2, pp. 1176–89, Jan. 2015.

[18] A. S. Karar and J. C. Cartledge, “Generation and detection of a 56 Gb/s signal using a DML and half-cycle 16-QAM Nyquist-SCM,” *IEEE Photonics Technol. Lett.*, vol. 25, no. 8, pp. 757–760, Apr. 2013.

[19] M. S. Erkilinc, Z. Li, S. Pachnicke, H. Griesser, B. C. Thomsen, P. Bayvel, and R. I. Killey, “Spectrally efficient WDM Nyquist pulse-shaped 16-QAM subcarrier modulation transmission with direct detection,” *J. Light. Technol.*, vol. 33, no. 15, pp. 3147–55, Aug. 2015.

[20] X. Wu, C. Huang, K. Xu, C. Shu, and H. K. Tsang, “128-Gb/s line rate OFDM signal modulation using an integrated silicon microring nodulator,” *IEEE Photonics Technol. Lett.*, vol. 28, no. 19, pp. 2058–61, Oct. 2016.

[21] K. Xu, C. Y. Wong, L. Zhang, L. Liu, N. Liu, C. W. Chow, and H. K. Tsang, "56 Gbit/s DMT signal generated by an integrated silicon ring modulator," in *Conference on Lasers and Electro-Optics*, 2016, p. STu1G.7.

[22] P. Dong, J. Lee, Y.-K. Chen, L. L. Buhl, S. Chandrasekhar, J. H. Sinsky, and K. Kim, "Four-channel 100-Gb/s per channel discrete multitone modulation using silicon photonic integrated circuits," *J. Light. Technol.*, vol. 34, no. 1, pp. 79–84, Jan. 2016.

[23] Y. Kai, M. Nishihara, T. Tanaka, R. Okabe, T. Takahara, J. C. Rasmussen, H. Ishihara, K. Goi, and K. Ogawa, "130-Gbps DMT transmission using silicon Mach-Zehnder modulator with chirp control at 1.55-μm," in *Optical Fiber Communication Conference*, 2015, p. Th4A.1.

[24] F. Pancaldi, G. Vitetta, R. Kalbasi, N. Al-Dhahir, M. Uysal, and H. Mheidat, "Single-carrier frequency domain equalization," *IEEE Signal Process. Mag.*, vol. 25, no. 5, pp. 37–56, Sep. 2008.

[25] Y. Gao, J. C. Cartledge, A. S. Kashi, S. S.-H. Yam, and Y. Matsui, "Direct modulation of a Laser using 112-Gb/s 16-QAM Nyquist subcarrier modulation," *IEEE Photonics Technol. Lett.*, vol. 29, no. 1, pp. 35–38, Jan. 2017.

[26] Y. Gao, Z. Wang, J. C. Cartledge, S. Yam, and A. Knights, "56 Gb/s single-carrier 16-QAM and 32-QAM subcarrier modulation using a silicon micro-ring resonator," in *Optical Fiber Communication Conference*, 2017, p. Th1B.2.

[27] J. Müller, F. Merget, S. S. Azadeh, J. Hauck, S. R. García, B. Shen, and J. Witzens, "Optical peaking enhancement in high-speed ring modulators," *Sci. Rep.*, vol. 4, p. 6310, 2014.

[28] F. Chang, K. Onohara, and T. Mizuochi, "Forward error correction for 100 G transport networks," *IEEE Commun. Mag.*, vol. 48, no. 3, pp. S48–S55, Mar. 2010.

Chapter 5 Resonance control using intrinsically defect-mediated photocurrent

The Si-MRR modulator, benefiting from resonance enhancement, can provide fast and efficient modulation with small footprint and low power consumption, which is especially attractive to inter-/intra- data center communications. However, one practical issue associated with resonant-type modulators is the large sensitivity to temperature fluctuation in the host environment [1]. In some cases, this thermal sensitivity is desirable and even intentionally exploited. For instance, in a WDM system consisting of multiple Si-MRR modulators, the resonance of each Si-MRR is thermally aligned to the designated WDM channel via an integrated heater [2–4]. Once the initial alignment is successfully performed, an undisrupted high-speed operation of the Si-MRR modulator will depend on a precise and continuous locking of the resonance and the laser wavelength. Thermal fluctuations such as a transient thermal load in an adjacent channel or a slow ambient temperature drift can create an undesired resonance shift that can become unbearable for the maintenance of high-speed operation.

In this chapter, an efficient resonance control utilizing the intrinsic defect-mediated photo-detection in the depletion-type Si-MRR is demonstrated. The intrinsic photocurrent results from sub-bandgap photo-absorption enabled by the residual crystal defects in the p-n junction after standard fabrication and is directly measured by a source-meter that simultaneously provides the DC bias for the p-n junction during the high-speed modulation. The described control scheme does not need a dedicated photodetector to monitor the power associated with detuning, thereby reducing the fabrication complexity (in fact, no additional fabrication is required above that used to fabricate the Si-MRR).

The resonance control is achieved by compensating the power of an integrated heater via a computer-aided *proportional-integral-differential* (PID) loop. The thermal stability of the Si-MRR modulator under high-speed operation is validated by a 12.5 Gb/s back-to-back BER measurement.

5.1 Resonance control method review

Silicon exhibits a large positive thermo-optic index (dn/dT is 1.86×10^{-4} /K at room temperature near 1.55 μm [5]) so that a red shift in the Si-MRR can be associated with an increase of temperature. A genuine approach to resolve the thermal sensitivity in Si-MRR is through athermalization in which a passive mechanism is intentionally engineered to counter-balance the overall thermal response of the Si-MRR [6]. The advantage of this approach is clearly that no extra power consumption is required for thermal control. One kind of athermal Si-MRR is obtained by adopting an SOI-compatible cladding material that can exhibit a negative thermo-optic coefficient, thus effectively 'neutralizing' the thermal response of the Si-MRR [7–9]. However, the main drawback is the need for post-processing that is not compatible with standard CMOS fabrication techniques and consequently increases fabrication complexity and cost. Another type of athermal Si-MRR is based on the modified interferometric structure, namely the *ring-assisted Mach-Zehnder interferometer* (RAMZI) where the Si-MRR is side-coupled onto one of the MZI arms [10]. The waveguide dimension for each MZI arm is modified so that the thermal-optic coefficient is different for each arm. When the device is thermally perturbed, the different phase shift between the two MZI arms can result in an overall 'negative' thermo-optic effect that cancels the thermal response of the Si-MRR. A modified RAMZI with a low modulation speed of 2 GHz has been demonstrated over a temperature range of 35 ^{o}C [11]. However, the downside of this

method includes an added fabrication uncertainty due to the re-engineered waveguides as well as the large footprint associated with the MZI.

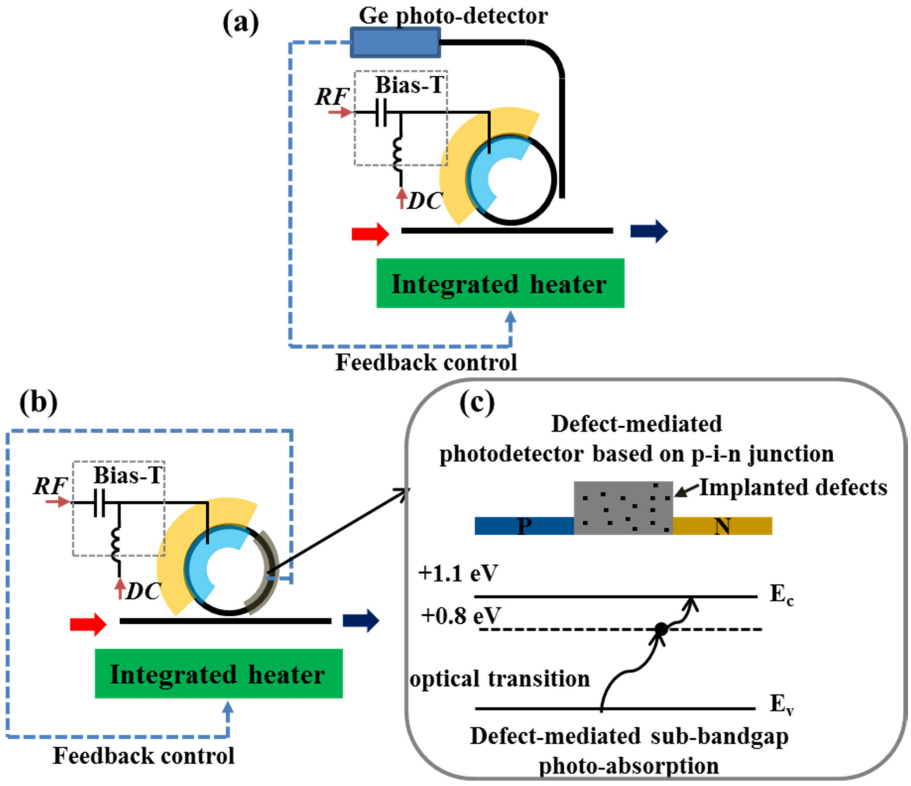

Figure 5.1 Conventional PID-based resonator control methods with (a) drop-port germanium photodetector (b) intra-cavity defect-mediated photodetector. (c) Cross-section view of the defect-implanted p-i-n diode and the simple bandgap model to explain the process of defected-mediated sub-bandgap photo-absorption.

In contrast to athermalizing the Si-MRR, active resonance control is a simpler and more viable approach to wavelength locking [12]. Although the drawback is the active power consumption associated with the control circuit, the overall power consumption for a single Si-MRR operation is likely to remain on the order of 100 fJ/bit (which will depend on the modulation rate). In particular, PID-based resonance control is a popular method that can be easily integrated into a CMOS circuit due to its simplicity. Figure 5.1 (a) shows the principle for the first proposed PID-based resonance control. A germanium

photodetector is used to provide a feedback signal by monitoring the drop-port power of the Si-MRR that corresponds to a detuning for a given laser wavelength [13]. When a deviation from the desired tuning (set-point value) occurs due to the thermal fluctuation, an error signal is generated and followed by the PID control that compensates the power on the heater until the resonance is stabilized. This method, however, is not a monolithic approach, as it requires heterogeneous integration of germanium, thereby increasing the fabrication complexity and cost.

Alternatively, defect-mediated sub-bandgap absorption can provide a monolithic solution for photo-detection in SOI [14]. A resonance control method utilizing an intra-cavity defect-mediated photodetector is shown in Figure 5.1 (b) where a defect-implanted lateral p-i-n junction is embedded into a portion of the ring waveguide to monitor the resonant power [15]. The resulting photocurrent due to the sub-bandgap absorption then provides the feedback signal for the PID control.

A simple model is given in Figure 5.1 (c) to explain the mechanism of the sub-bandgap absorption. Silicon is transparent to the communication wavelength (0.8 eV for photon energy at 1550 nm and the silicon bandgap is 1.1 eV). However, the presence of defects such as interstitials and vacancies in silicon can create deep levels (e.g. ~0.8 eV above the conduction band) that allow electrons to be elevated from the conduction band, by photon absorption, and subsequently excited to the conduction band through thermal excitation. These electrons are then swept across the junction by an electric field, leading to a photocurrent. It is known that this photocurrent depends on the density of the defects as well as the optical intensity of the overlapping mode [16, 17]. By placing the photodetector inside the cavity, the sub-bandgap absorption can be dramatically increased due to the large power build-up around resonance if the Si-MRR is assumed to be

critically coupled [18]. However, the drawback of this method is that in addition to the standard ion implantation to form the p-n junction for high-speed operation, a secondary ion implantation is needed to create the defect region. Moreover, for a small-radius Si-MRR modulator, a poor isolation between the defect-implanted region and the high-speed modulation region can potentially lead to an undesired electrical crosstalk that degrades the modulator performance.

5.2 Tapless resonance control using intrinsic defect-mediated photo-current

The method shown in Figure 5.1 (b) is an attractive approach to resonance control due to the monolithic photo-detection. The tapless resonance control method as shown in Figure 5.2 can be considered as a variant of the control method given in Figure 5.1 (b) but provides a much simpler design without the need for a separate photodetector. The depletion p-n junction under reverse bias can readily produce an intrinsic photocurrent that arises due to residual lattice defects following standard junction formation via ion implantation and *rapid thermal annealing* (RTA). The RTA is responsible for dopant activation as well as removal of the overwhelming majority of defects produced after ion implantation, but a small amount of defects still remain in the junction [19], resulting in sufficient photo-absorption because of the intra-cavity power build-up [20]. High-speed detection using residual defects has been demonstrated in the depletion-type Si-MRR photodetector that has the same configuration as the depletion-type Si-MRR modulator but with a reversed electrical signal flow (Bias-T decouples the DC and RF components of the signal instead of coupling them) [21]. In the present case, the DC photocurrent can be directly measured by a source-meter that simultaneously provides the reverse bias at

the DC port of the Bias-T during high-speed modulation. The advantage of this tapless method compared to the other two methods given by Figure 5.1 (a) and (b) can be easily shown. No tap is needed so that the p-n junction can be designed to maximally cover the ring resonator, thereby increasing the modulation efficiency as proved by Eq. (2.39). Furthermore, no excess optical loss is introduced to the modulator over the intrinsic loss associated with the fabricated device. The disadvantage, however, is that the device must operate in depletion mode so that the photocurrent can be measured. This limits the use of this tapless resonance control method for the depletion-type Si-MRR modulator only.

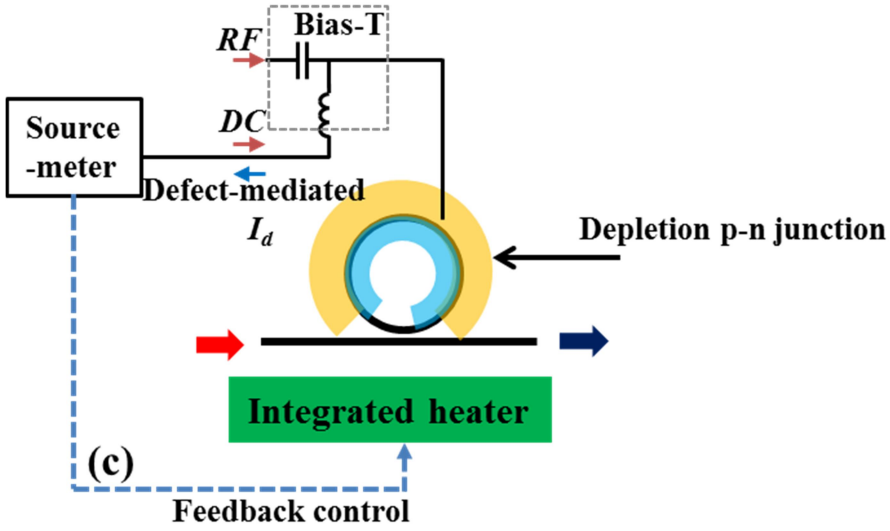

Figure 5.2 Tapless resonance control using intrinsic defect-mediated photocurrent as a measure to the resonant power.

The defect-mediated photodetector, in principle, has a linear responsivity [22], [23]. It is later shown to be advantageous in compensating the input power variation that is often responsible for the instability of the PID control. The linear dependence between the photocurrent and the input optical power allows the set-point current in the PID loop to be normalized to correspond to a specific detuning, thereby increasing the resilience to

the input optical power fluctuation. This normalization procedure will be further elaborated in section 5.4.

It should be mentioned that a similar device geometry was reported earlier in 2017 [24]. However, the mechanism for photocurrent generation in that case is based on *two-photon absorption* (TPA) [25]. In order to exploit the TPA with an appreciable efficiency, a relatively large optical input power together with a high-Q (>20,000) cavity are required to produce sufficient photo-carriers. The downside can be seen as a much higher sensitivity to the input optical power fluctuation that can result in the control instability. Besides, the maximum cavity bandwidth is limited approximately to 9.5 GHz owing to the high Q requirement and the device exhibits a much higher insertion loss due to the undesired TPA-induced optical absorption in the intrinsic region (e.g. bus waveguide). In contrast, the defect-mediated method shown here requires much lower optical input power, and is essentially independent of the Q-factor of the resonator. Thus, the proposed method is compatible with bandwidths of many tens of GHz.

5.3 Device characterization

The Si-MRR modulator used to demonstrate the resonance control in this chapter is obtained from the same fabrication as described in Chapter 3. The defect-mediated photocurrent can be consistently measured from Si-MRR devices at different locations across the wafer map as long as the laser wavelength is aligned near to the resonance. The results presented here are chosen from a particular Si-MRR device with a deep notch depth that is able to provide an adequate photocurrent even at a very low optical power input. To improve the measurement stability, the integrated heater of the Si-MRR modulator was wire-bonded to an external PCB as shown in Figure 5.3 (a). The high-

speed signal was delivered to the signal pads through a G-S-G probe as shown in Figure 3.1. To obtain the heater efficiency, optical spectra with zero bias on the p-n junction were obtained for a range of heater powers (chosen approximately between 0 mW and 60 mW), with the results plotted in Figure 5.3 (b). In Figure 5.3 (c), the heater efficiency (defined as resonance shift per mW) was determined to be 56.8 pm/mW through a linear fit between the extracted resonance shift and the corresponding heater power. This calculation has included the parasitic resistance associated with the wire bonding. The Q-factor of the Si-MRR was estimated to be 11,000 and the small-signal response is similar to the one shown in Figure 3.3 (b).

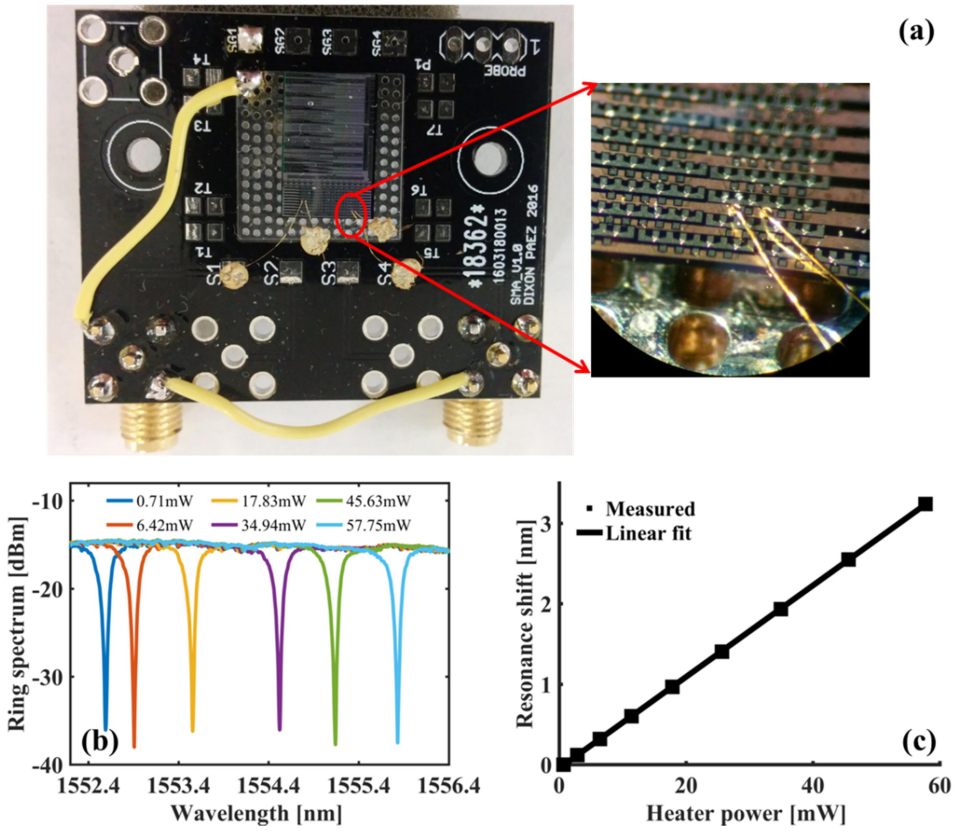

Figure 5.3 (a) Photo to show the wire-bonded Si-MRR device for thermal control. (b) Measured Si-MRR spectra for different heater powers. (c) Extracted resonance shift with respect to the applied heater power using a linear fit.

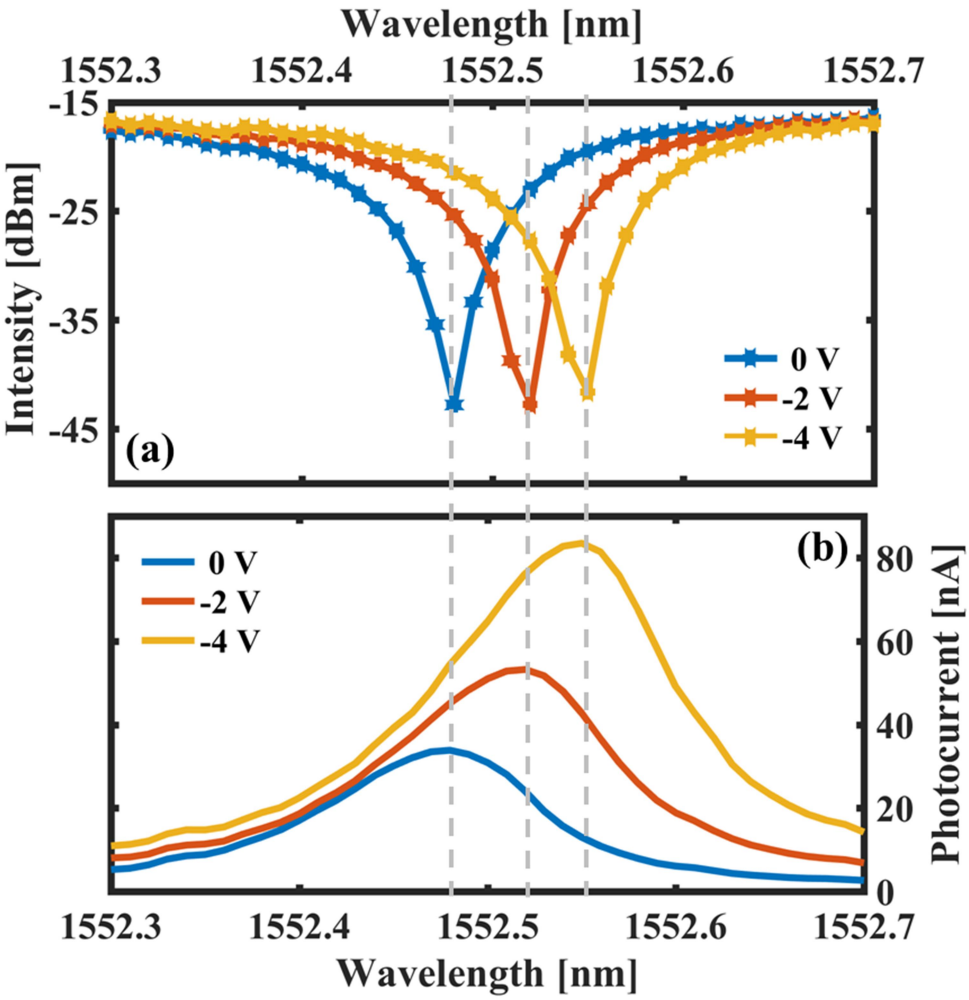

Figure 5.4 (a) Si-MRR spectra under different reverse biases from 0 V to -4 V. Intensity refers to light output from the chip. (b) Measured photocurrent versus wavelength.

The optical spectra as shown in Figure 5.4 (a) were measured under zero bias and two reverse biases (-2 V and -4 V), using the setup given by Figure 3.2 (a). As the laser wavelength was swept in steps of 100 pm, a source-meter maintained the reverse bias on the p-n junction through the DC port of the Bias-T and simultaneously measured the intrinsic defect-mediated photocurrent, the results of which are shown in Figure 5.4 (b). It is seen that the shape of the photocurrent curves tracks faithfully that of the intensity transfer with peak photocurrents and resonances occurring at the same wavelength

denoted by the dashed lines. The photo-detection also benefits from a large power build-up because of the nearly critically coupled condition indicated by the large notch depth (>25 dB). Thus for a relatively low optical input power (<-8 dBm deduced from Figure 5.4 (a)), photocurrent can be measured even in the absence of a reverse bias. The peak photocurrent also increases proportionally with increases in reverse bias due to the increased cross-junction field that improves carrier collection efficiency.

The intrinsic photocurrent measured during the high-speed operation should only correspond to the average DC-level intensity in the cavity due to the low-pass nature of the DC port of the Bias-T. An experiment to study the influence of the speed of RF modulation on the generated photocurrent was conducted by varying the data rates at the RF port of the Bias-T. The peak-to-peak voltage for the RF signal was set to 2 V and the reverse bias was maintained at -2 V to ensure the junction remained in reverse bias (the RF reflection was compensated for in this case). The maximum heater power was limited at 60 mW to prevent a potential burnout (the maximum load is known to be close to 100 mW from previous experience). The laser wavelength was chosen as 1554 nm so that increasing or decreasing the heater power could produce a red or blue shift respectively as indicated by Figure 5.3 (b). A sub-mounted temperature controller (TEC) maintained the temperature of the chip at 25 ^{o}C to guarantee that the thermal change is only from the integrated heater. The photocurrent was recorded by the source-meter when the heater power was scanned from 0 m W to 60 mW. The input power (defined as the optical power at the input of the Si-MRR modulator) was varied from 0.01 mW to 0.64 mW, with an incremental step of 0.09 mW (the laser power was calibrated and the fiber to grating coupling loss at the input coupler subtracted to arrive at these values). The measured photocurrents are shown in Figure 5.5. The three plots are shifted with respect to each other by 15 mW along the x-axis for a visual clarity (otherwise, the three plots

overlaps). The measured photocurrents are almost identical regardless of the data rate, indicating that the influence from the RF signal is negligible, as expected from a good electrical isolation between the DC and RF ports of the Bias-T.

The responsivity of the defect-mediated photo-detection can be calculated by a linear fit between the peak (on-resonance) photocurrent (averaged over the results for three data rates) and input power as given in Figure 5.6. The responsivity extracted from the linear fit was thus determined to be 1 mA/W. The responsivity is shown to be essentially linear, despite a noticeable measurement noise that likely results from the input power fluctuation.

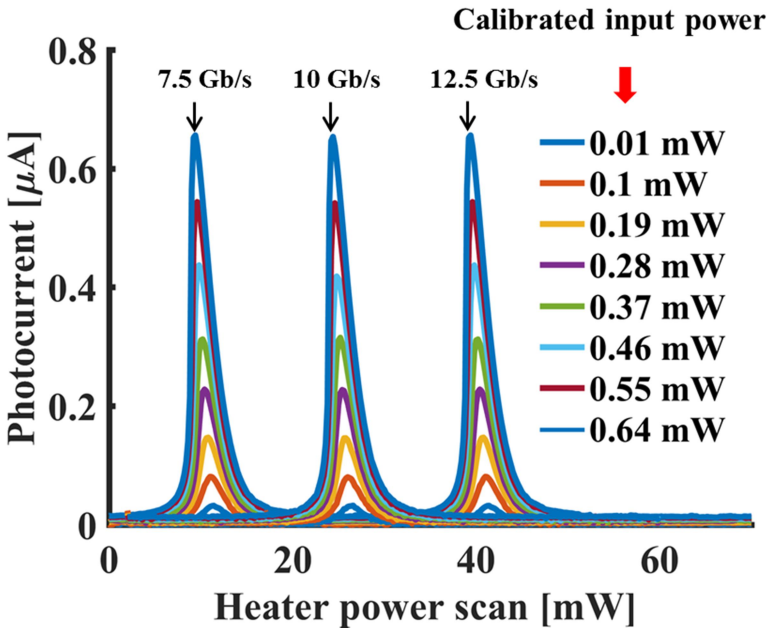

Figure 5.5 Recorded photocurrent curves versus the heater power scan for various on-chip optical powers. The results are shown for three data rates, 7.5 Gb/s, 10 Gb/s and 12.5 Gb/s with 2 V peak-to-peak voltage and -2 V Bias.

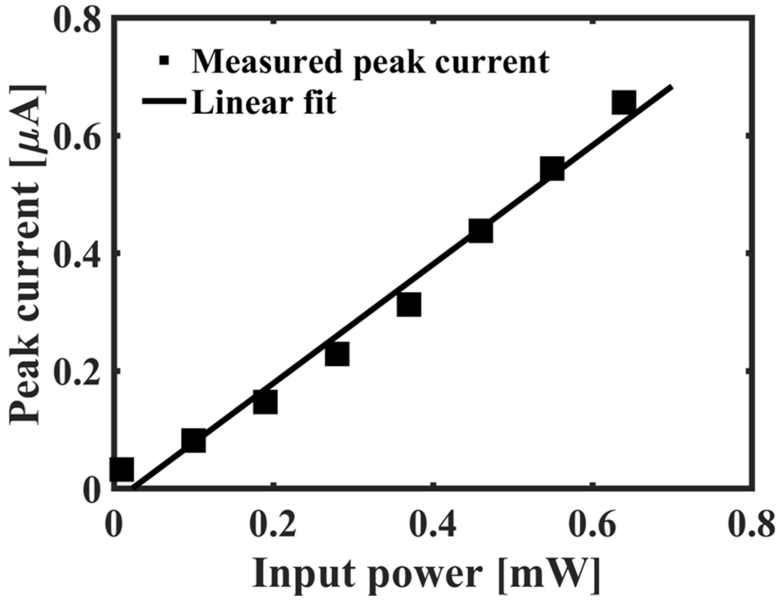

Figure 5.6 Measured peak photocurrent versus the input power along with a linear fit.

5.4 Resonance control algorithm implementation

A calibration is first performed to obtain the intrinsic photocurrent with respect to the heater power sweep in a pre-defined working range (e.g. from P_{min} =0 mW to P_{max} =60 mW) as shown in Figure 5.7. The calibrated profile is only valid for a given initial condition including reverse bias, input power, RF signal, etc., which should remain unchanged during the entire high-speed operation. Next, a set-point current I_{sp} is chosen for a desired modulation condition. The detuning and the slope type (blue or red) to be modulated will have a significant impact on the modulation characteristics such as extinction ratio, linearity, bandwidth, as well as modulation chirp, which has been elaborated upon throughout the thesis. In Figure 5.7, eye diagrams captured at different I_{sp} with an input power of 0.32 mW are shown as an example. It should be mentioned that the red-side modulation would suffer from self-heating effects that are associated with the

skew appearance in the photocurrent plot. This effect would become more severe as the intra-cavity power increases. The downside of an excessive self-heating effect is that the resonance is difficult to stabilize (partially also due to a sharper slope of the transfer), thereby leading to a certain amount of eye-closure as readily shown in Figure 5.7.

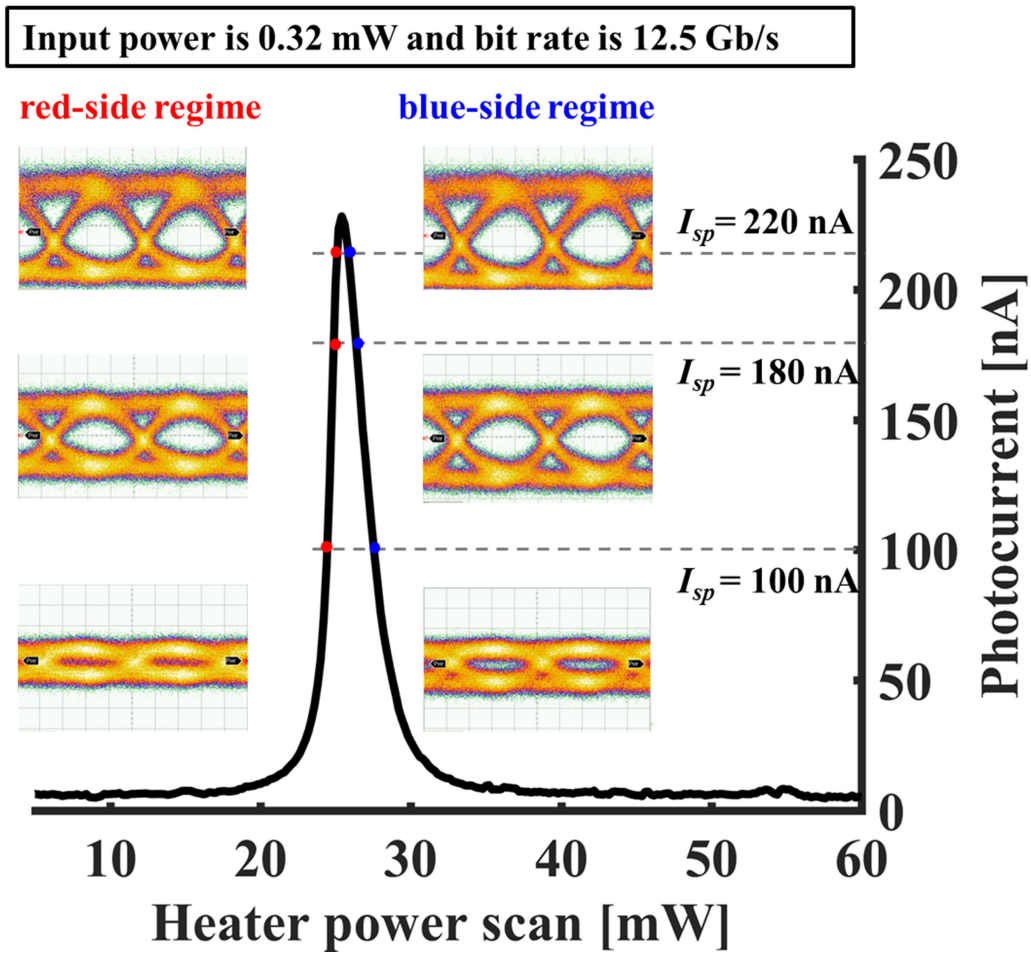

Figure 5.7 Modulation regimes for the Si-MRR and eye-diagrams at different set-point photocurrents (I_{sp}) in both regimes for a 12.5 Gb/s NRZ modulation.

Figure 5.8 shows the flowchart for the resonance control algorithm implemented in the computer controlling the source-meter and heater power supply via a closed-loop. Firstly, a desired I_{sp} is chosen from the calibration profile as shown in Figure 5.7 and the heater power is coarsely tuned either from P_{min} to P_{max} for the red-side modulation or

from P_{max} to P_{min} for the blue-side modulation. The PID control loop is triggered for fine tuning once the photocurrent approaches I_{sp} and eventually locks the photocurrent to I_{sp}. The cycle period for the control loop is estimated to be shorter than 1 ms, mainly limited by the communication delay between the computer and the control apparatus. Two additional functions (for the sake of a stability check) are also implemented in the PID loop to prevent the system from thermal runway, meaning that the heater power will be continuously increased by the PID loop until burnout. This unstable situation results from the error signal ($I\left(k\Delta t\right)-I_{sp}$) switching sign, which could happen when the modulation regime changes due to a burst of thermal fluctuation or a reduced input power lowers the peak photocurrent below I_{sp} (the latter will eventually force the modulation to switch to the other side of the slope). Confirmation of the slope type (red or blue) is realized by providing a very small power change to the heater and measuring the resulting current change (for example, if the modulation is on the blue side, increasing the heater power will reduce the photocurrent). Furthermore, the power check is provided by an off-chip power meter taping 10% of the output optical power. If the reduction is measured to be more than 2 dB (typically a thermal runaway is observed at this value for an original input power of 0.32 mW), the PID control loop is forced to halt to avoid the thermal runway. The main cause for a reduction of the input power is fiber drift from the optimum coupling location during many minutes of operation.

A normalization procedure is proposed to alleviate the instability of the PID control due to the input power fluctuation that for example, results from a laser power change or laser to chip coupling efficiency change. Since the instability originates from the fact that detuning does not correspond to a constant I_{sp} for different input power, a normalization factor $\beta = P\left(k\Delta t\right)/P\left(0\right)$ can be multiplied onto I_{sp} where $P\left(k\Delta t\right)$ is the input power measured at each discrete time step, $k\Delta t$, in each consecutive loop and $P\left(0\right)$

is the initial input power. As the input power is associated with the peak photocurrent via a linear dependency, the influence of the input power variation can be negated by the normalized I_{sp} that always corresponds to the same detuning. This method requires a means to measure the input power, likely prior to the modulator, via a tap-port terminated with an integrated defect-mediated photodetector in order to maintain a Ge-free process. This method only functions when the photo-detection at both the modulator and input tap-port has a linear responsivity that is the case for the photo-detection mechanism described here.

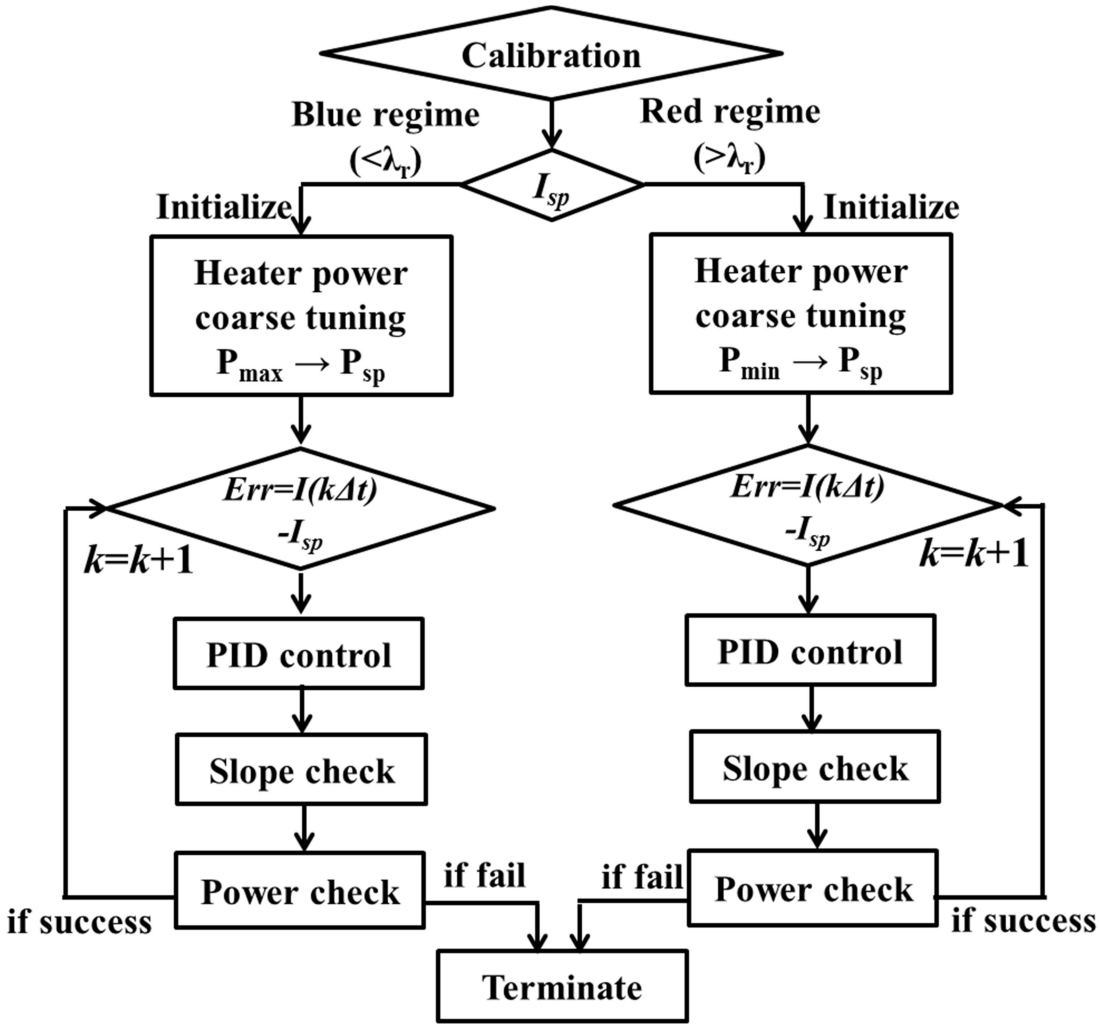

Figure 5.8 Computer-aided PID algorithm for resonance control measurement.

5.5 Validation of resonance control via BER measurement

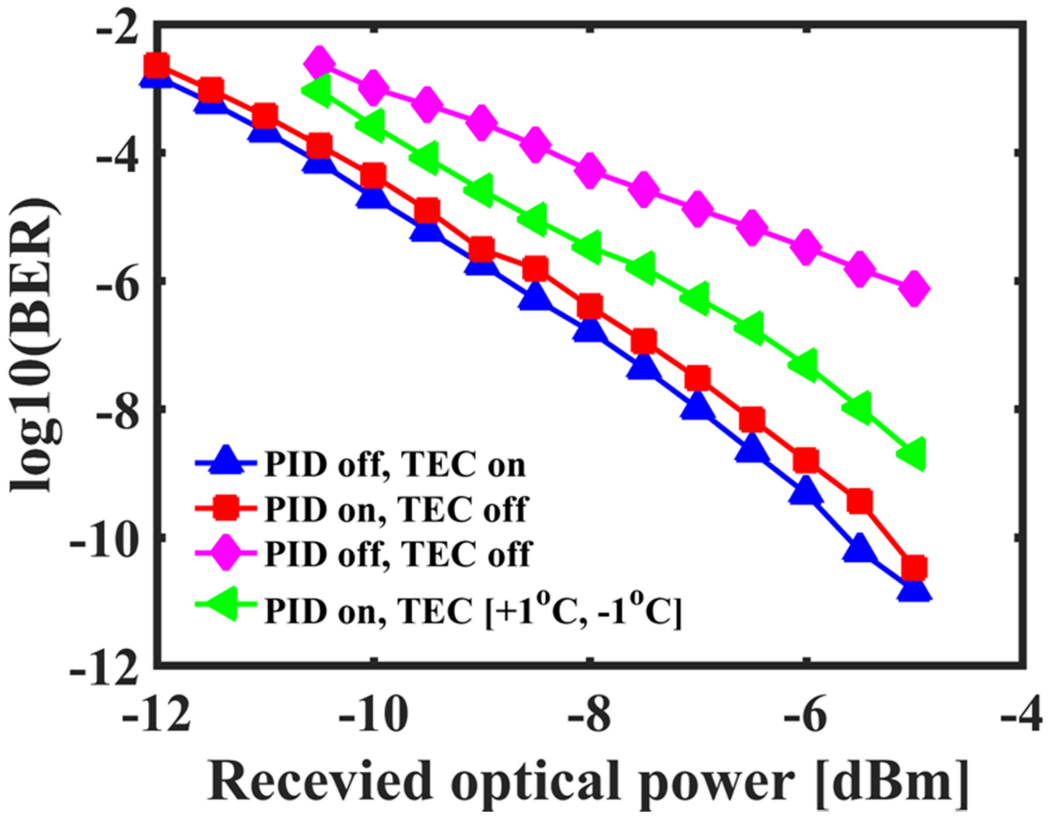

Figure 5.9 A set of measured BER curves of a 12.5 Gb/s rate fordifferent conditions

The resonance control algorithm was validated by a set of 12.5 Gb/s back-to-back BER measurement under different operating conditions. Four BER curves are plotted in Figure 5.9 in which I_{sp} was set to 180 nA on the blue-side of resonance while other driving conditions remained the same as used in Figure 5.7. The first and second BER curves (blue and red) were obtained when one of either the sub-mounted TEC control or the on-chip resonance control was enabled while the other was turned off. The difference between the two curves was negligibly small, indicating that the on-chip resonance control can provide a similar level of stability as the sub-mounted TEC. This is not

surprising because the sub-mounted TEC is also based on PID control. The third BER curve (purple) was obtained when both controls were disabled. A significant degradation can be observed, which results from an uncontrolled thermal environment. The last BER curve (green) was measured when the on-chip resonance control was turned on with an intentional temperature fluctuation of $\pm 1^{o}$C created by the sub-mounted TEC. The BER result exhibited a small power penalty of around 1 dB at 10^{-9} compared to the blue or red curve. The degradation was related to variation of the fiber-to-chip coupling (observed via our off-chip tap) when the sub-mount was heated and cooled.

The error currents recorded in each cycle of the PID loop are also given in Figure 5.10 in order to support the previous analysis. The four plots correspond to a 2-minute time window and are translated by 30 nA with respect to each other along the y-axis for visual clarity. It can be seen that as long as the on-chip control is enabled (red and green lines), the error current is centered at the respective zero level (shown as the black line) over time due to a functional resonance control that locked the photocurrent at $I_{sp.}$ On the contrary, when the device was not thermally controlled (purple line), the error current slowly walked off the zero level, indicating a permanent resonance change that was not compensated. When the temperature variation was induced and the on-chip resonance control is off (black line), the error current reflected the magnitude of the deviation and the resulting BER became unmeasurable without the on-chip resonance control. Eye-diagrams were also captured at random times during the BER measurement with each eye-diagram based on 50 sweeps. With the on-chip resonance control disabled, the eye-diagrams were completely distorted owing to the temperature fluctuation. However, when the on-chip control was implemented, the eye-diagrams maintained the shape at the set point relatively faithfully (compared to the eye diagram in Figure 5.7) due to successful locking.

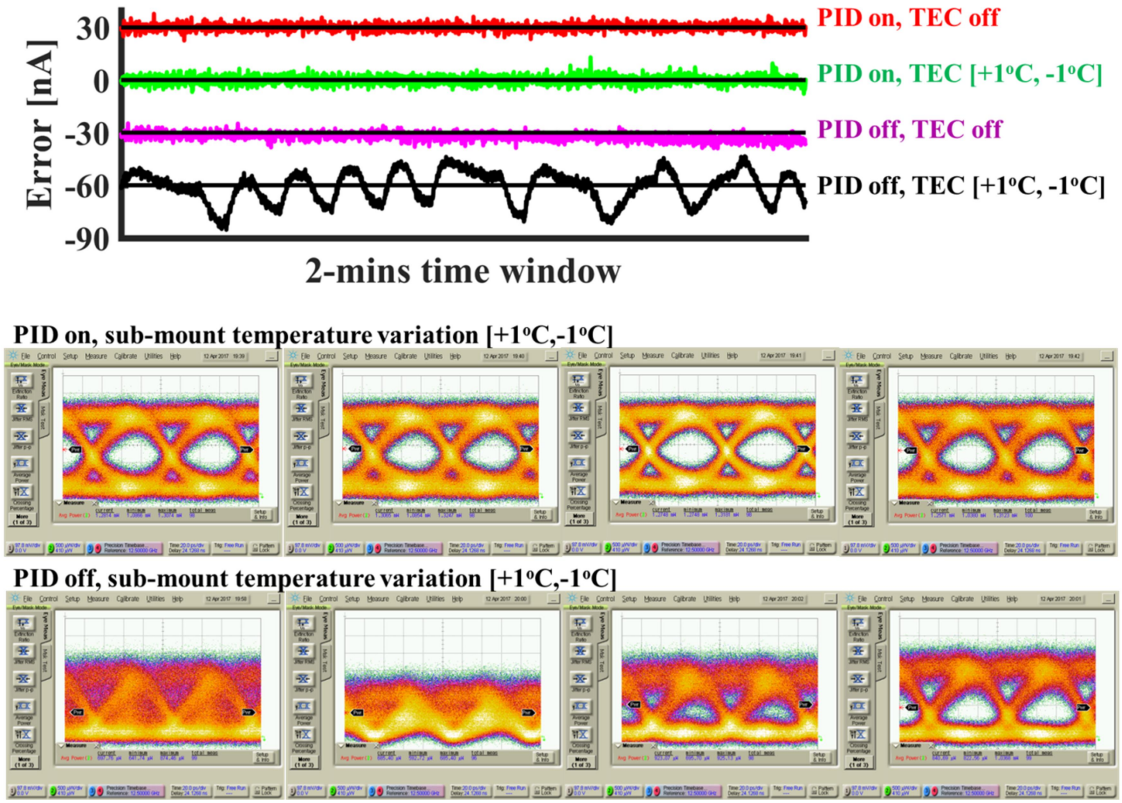

Figure 5.10 Error current collected in a 2 minutes window and randomly selected eye diagrams when the control was either on or off during the BER measurement when a temperature variation was induced.

In this chapter, a generic resonance control method was introduced, utilizing the defect-mediated photocurrent that intrinsically arises from the residual defects in a depletion p-n junction. The simplicity of this method negates the need for a drop-port germanium photodetector as well as a dedicated intra-cavity defect-mediated photodetector, allowing the ring waveguide to be maximally covered by the p-n junction. A digital PID control algorithm was designed and the issues that can cause control instability were identified and addressed. A proposal was made to compensate the input power fluctuation, utilizing a normalization factor due to the linear responsivity. The BER results were obtained as essentially error free when the on-chip feedback control was enabled, even under an intentionally induced temperature fluctuation. Furthermore, the

proposed control scheme can be easily integrated into a CMOS circuit to achieve a tapless resonance control.

Reference

[1] K. Padmaraju and K. Bergman, "Resolving the thermal challenges for silicon microring resonator devices," *Nanophotonics*, vol. 3, no. 4–5, pp. 269–281, Jan. 2013.

[2] X. Zheng, E. Chang, P. Amberg, I. Shubin, J. Lexau, F. Liu, H. Thacker, S. S. Djordjevic, S. Lin, Y. Luo, J. Yao, J.-H. Lee, K. Raj, R. Ho, J. E. Cunningham, and A. V. Krishnamoorthy, "A high-speed, tunable silicon photonic ring modulator integrated with ultra-efficient active wavelength control," *Opt. Express*, vol. 22, no. 10, p. 12628-33, 2014.

[3] P. Dong, R. Shafiiha, S. Liao, H. Liang, N.-N. Feng, D. Feng, G. Li, X. Zheng, A. V Krishnamoorthy, and M. Asghari, "Wavelength-tunable silicon microring modulator.," *Opt. Express*, vol. 18, no. 11, pp. 10941–6, May 2010.

[4] P. Dong, W. Qian, H. Liang, R. Shafiiha, N.-N. Feng, D. Feng, X. Zheng, A. V. Krishnamoorthy, and M. Asghari, "Low power and compact reconfigurable multiplexing devices based on silicon microring resonators," *Opt. Express*, vol. 18, no. 10, pp. 9852-58, May 2010.

[5] G. E. Jellison and H. H. Burke, "The temperature dependence of the refractive index of silicon at elevated temperatures at several laser wavelengths," *J. Appl. Phys.*, vol. 60, no. 2, pp. 841–843, Jul. 1986.

[6] Y. Kokubun, N. Funato, and M. Takizawa, "Athermal waveguides for temperature-independent lightwave devices," *IEEE Photonics Technol. Lett.*, vol. 5, no. 11, pp. 1297–1300, Nov. 1993.

[7] J. Teng, P. Dumon, W. Bogaerts, H. Zhang, X. Jian, X. Han, M. Zhao, G. Morthier, and R. Baets, "Athermal silicon-on-insulator ring resonators by overlaying a polymer cladding on narrowed waveguides," *Opt. Express*, vol. 17, no. 17, pp. 14627-33, Aug. 2009.

[8] J. M. Lee, D. J. Kim, H. Ahn, S. H. Park, and G. Kim, "Temperature dependence of silicon nanophotonic ring resonator with a polymeric overlayer," *J. Light. Technol.*, vol. 25, no. 8, pp. 2236–2243, 2007.

[9] B. Guha, J. Cardenas, and M. Lipson, "Athermal silicon microring resonators with titanium oxide cladding," *Opt. Express*, vol. 21, no. 22, pp. 26557–63, 2013.

[10] B. Guha, B. B. C. Kyotoku, and M. Lipson, "CMOS-compatible athermal silicon microring resonators.," *Opt. Express*, vol. 18, no. 4, pp. 3487–3493, 2010.

[11] B. Guha, K. Preston, and M. Lipson, "Athermal silicon microring electro-optic modulator," *Opt. Lett.*, vol. 37, no. 12, pp. 2253-55, 2012.

[12] Y. Zhang, Y. Li, S. Feng, and A. W. Poon, "Towards adaptively tuned silicon microring resonators for optical networks-on-chip applications," *IEEE J. Sel. Top. Quantum Electron.*, vol. 20, no. 4, pp. 136-149, 2014.

[13] K. Padmaraju, D. F. Logan, X. Zhu, J. J. Ackert, A. P. Knights, and K. Bergman, "Integrated thermal stabilization of a microring modulator.," *Opt. Express*, vol. 21, no. 12, pp. 14342–50, Jun. 2013.

[14] J. J. Ackert, "High-speed silicon detector structures for photonic integrated circuits," *PhD dissertation*, McMaster University, 2015.

[15] Y. Li and A. W. Poon, "Active resonance wavelength stabilization for silicon microring resonators with an in-resonator defect-state-absorption-based photodetector," *Opt. Express*, vol. 23, no. 1, pp. 360-372, 2015.

[16] D. F. Logan, P. E. Jessop, A. P. Knights, R. M. Gwilliam, and M. P. Halsall, "The effect of doping type and concentration on optical absorption via implantation induced defects in silicon-on-insulator waveguides," *Conf. Optoelectron. Microelectron. Mater. Devices, Proceedings, COMMAD*, no. 1, pp. 152–155, 2008.

[17] D. F. Logan, K. J. Murray, J. J. Ackert, P. Velha, M. Sorel, R. M. De La Rue, P. E. Jessop, and a P. Knights, "Analysis of resonance enhancement in defect-mediated silicon micro-ring photodiodes operating at 1550 nm," *J. Opt.*, vol. 13, no. 12, p. 125503, 2011.

[18] J. K. Doylend, P. E. Jessop, and a P. Knights, "Silicon photonic resonator-enhanced defect-mediated photodiode for sub-bandgap detection.," *Opt. Express*, vol. 18, no. 1, pp. 14671–14678, 2010.

[19] C. Carter, W. Maszara, D. K. Sadana, G. A. Rozgonyi, J. Liu, and J. Wortman, "Residual defects following rapid thermal annealing of shallow boron and boron fluoride implants into preamorphized silicon," *Appl. Phys. Lett.*, vol. 44, no. 4, pp. 459–461, Feb. 1984.

[20] H. Yu, D. Korn, M. Pantouvaki, J. Van Campenhout, K. Komorowska, P. Verheyen, G. Lepage, P. Absil, D. Hillerkuss, L. Alloatti, J. Leuthold, R. Baets, and W. Bogaerts, "Using carrier-depletion silicon modulators for optical power monitoring.," *Opt. Lett.*, vol. 37, no. 22, pp. 4681–3, 2012.

[21] X. Li, Z. Li, X. Xiao, H. Xu, J. Yu, and Y. Yu, "40 Gb/s all-silicon photodetector based on microring resonators," *IEEE Photonics Technol. Lett.*, vol. 27, no. 7, pp. 729–732, 2015.

[22] Y. Li, S. Feng, Y. Zhang, and A. W. Poon, "Sub-bandgap linear-absorption-based photodetectors in avalanche mode in PN-diode-integrated silicon microring resonators.," *Opt. Lett.*, vol. 38, no. 23, pp. 5200–3, 2013.

[23] B. Desiatov, I. Goykhman, J. Shappir, and U. Levy, "Defect-assisted sub-bandgap avalanche photodetection in interleaved carrier-depletion silicon waveguide for telecom band," *Appl. Phys. Lett.*, vol. 104, no. 9, 2014.

[24] A. Melikyan, K. Kim, Y.-K. Chen, and P. Dong, "Tapless locking of silicon ring modulators for WDM applications," in *Optical Fiber Communication Conference*, 2017, p. Tu2H.6.

[25] M. Casalino, G. Coppola, M. Iodice, I. Rendina, and L. Sirleto, "Near-Infrared Sub-Bandgap All-Silicon Photodetectors: State of the Art and Perspectives," *Sensors*, vol. 10, no. 12, pp. 10571–10600, Nov. 2010.

Chapter 6 Conclusion and future work

This thesis document presents a study of high-speed Si-MRR modulator operation and specifically presents new insight into the following: device and system performance modeling; chirp characteristic in the extended reach; advanced modulation format; and resonance control. These subjects are highly interrelated and this work aims to promote Si-MRR modulators for data center applications from short to extended reach. In this chapter, a summary of the thesis work is first presented and suggested future work is then discussed.

A thorough theoretical basis was presented in Chapter 2, using a bottom-to-top modeling that aimed to support the device-to-system performance of a Si-MRR modulator. In this analytical approach to solving the plasma dispersion effect, the effective index and optical mode profile for a single-mode SOI waveguide were computed by the EIM, whereas the classical, well-established 1-D p-n junction theory under a full-depletion assumption was utilized to obtain the free carrier profile along with the junction RF characteristic. Subsequently, the static response of the Si-MRR modulator was calculated by incorporating the plasma dispersion effect into the static transfer function of a passive ring resonator. Further, the dynamic response of the Si-MRR modulator was obtained by the well-known CMT equations that contain two perturbing terms for the cavity loss and resonance frequency. The calculated slowly varying envelope due to the electrical modulation served as the link between the device simulation and the system simulation, thus enabling the performance of a transmission link to be examined. A simple system end-to-end simulation was demonstrated to show the chirp-induced power penalty of an over-coupled Si-MRR modulator in an intensity-modulated system.

Chapter 3 provided a theoretical analysis of the chirp characteristic of an over-coupled Si-MRR modulator, using the α-parameter. Then, the negative-chirp modulation for a 10 Gb/s NRZ modulation was experimentally demonstrated for the first time using a depletion-type Si-MRR modulator. The low chirp-induced power penalty after a 100 km link distance resulted from the optimally designed over-coupled Si-MRR modulator that generated a small negative chirp at the optical pulse transition period. As a result, the optical pulse first underwent a pulse compression before broadening as graphically illustrated by the eye diagrams captured for different link distances. This study is important if the Si-MRR modulator (commonly used for the short-reach interconnect) can be useful and competitive in the medium-reach application, such as inter-data center communication where the performance can be limited by the chirp-induced signal distortion.

Chapter 4 explored the potential of advanced modulation formats in the Si-MRR-based system in order to increase the spectral efficiency, which is driven by the need for a higher system capacity. In the first section, the capability of achieving coherent modulation was conveyed by an experimental demonstration of a low-voltage driven BPSK modulation using an over-coupled Si-MRR modulator. The second section described work with emphasis on a DSP-enabled spectrally efficient 16-QAM Nyquist subcarrier modulation. The rationale of this study is that the Si-MRR modulator has a superior performance for intensity modulation in terms of efficiency and footprint, while the subcarrier multiplexing is an excellent approach to increase the spectral efficiency in an intensity-modulated system with a limited number of optical carriers. For this section, a single-carrier, single-polarization with ultra-high data rate (104 Gb/s) 16-QAM N-SCM modulation was experimentally achieved in the back-to-back measurement, owing to a

combination of pulse-shaping and pre/post- compensation DSP techniques to mitigate the nonlinear distortion and bandwidth insufficiency problems in the Si-MRR modulator.

Chapter 5 described a generic PID-based resonance control method for a depletion-type Si-MRR modulator. The feedback signal was provided by the intrinsic photocurrent resulting from residual-defect-mitigated sub-bandgap absorption. The residual defect was believed to remain after the standard p-n junction formation and annealing process, thus negating the need for either a dedicated intra-cavity defect-implanted monitor or a drop-port Ge photodetector. Furthermore, this photocurrent was directly collected by a source-meter while the Si-MRR modulator was under RF modulation. This control configuration can allow the ring waveguide to be maximally covered by the p-n junction in order to increase the modulation efficiency that is critical for the performance of a depletion-type Si-MRR modulator. A digital PID control algorithm was developed and confirmed by successfully locking the resonance during a 12.5 Gb/s high-speed BER measurement in the back-to-back system. The responsivity of the photo-detection is linear, which can be utilized for removing the instability issue caused by the input optical power drift.

Some recommended future work that can extend the scope of this thesis is now discussed. Firstly, a more comprehensive study can be used in the future to compare the Si-MRR modulator to other modulators based on different technologies regarding the key figures of merit such as bandwidth, power consumption and thermal stability. In Chapter 2, Monte-Carlo simulation can be implemented to examine the probability of all outcomes (device performance) associated with the fabrication uncertainty. This requires substituting a group of design parameters (e.g. doping level, junction offset, waveguide dimension, etc.) that have inherent uncertainties. It is also beneficial to perform a full-

numerical simulation to investigate if there is any persistent deviation between the analytical approach and numerical approach. If a deviation occurs, it means that the analytical model will generally lead to a biased device performance so that some correction factors should be inserted as supplements for the analytical modeling. For the CMT simulation where rate equations are solved, more advanced numerical algorithms (e.g. backwards Euler method) can be used to improve the simulation stability and accuracy

More work can be done for the system model for it is still an on-going effort. For instance, advanced modulation formats (e.g. PAM-4, subcarrier modulation) in conjunction with proper detection and error counting simulations can be further incorporated in the model since it is particularly important to have a systematic study on performance limits for advanced modulation techniques such as the one shown in section 4.2. Moreover, some DSP functions such as filtering, equalization, etc., can be included for more realistic simulations.

In Chapter 3, the performance (specifically the modulation chirp) for the under-coupled Si-MRR modulator in extended reach can be further investigated. As the near critically coupled condition is the design target for extend-reach applications, the resulting device can be expected to be either over-coupled or under-coupled owing to the fabrication uncertainty. For an under-coupled condition, the sign of chirp may vary during modulation and consequently a negative chirp cannot be maintained. If this modulation chirp causes a performance limit, a chirp compensation mechanism such as electrical pre-compensation or dispersion compensating fiber must be employed to improve the overall transmission performance. In this case, the starting point would then be to quantify the

modulation chirp generated in the under-coupled Si-MRR, using the methods readily shown in Chapter 3.

For the N-SCM work presented in Chapter 4, a comprehensive study could be planned in order to determine the dominant limiting factor (e.g. bandwidth, linearity or detuning) in the system performance without relying on time-consuming and expensive exercises in the lab. Therefore, a system-level model as suggested previously must be provided first so that it can provide a comparison study by varying a particular condition (e.g. detuning or resonator Q-factor). Moreover, DSP is notoriously known for its large power consumption that is somewhat prohibited in the cost-sensitive applications. As a result, the total power consumption including the essential DSP for the N-SCM to be used in the communication link needs to be estimated. Can the power consumption be reduced by optimizing the DSP| algorithm (e.g. reducing the number of tap used in VNLE)?

Finally, the future work in Chapter 5 can be related to the estimation of the power consumption for the resonance control scheme described. To achieve this, an integrated device must be realized in the first place. For example, the Si-MRR device can be bonded to an external circuit that provides a similar function as the source-meter, while the heater power tuning in the PID loop can be realized by a programmable off-the-shelf FPGA chip together with a power supply that provides the resonance control. Another suggested future work is to investigate the long-term stability (e.g. responsivity) of the defect-mediated absorption through a high-temperature aging study. One interesting question still remains that if the defect-mediated absorption through residual defects is independent of fabrication process, which leads to theoretical study on residual defects (such as the originality, composition and thermal stability).